

## ABSTRACT

Title of dissertation:      **SEARCHING FOR ENTANGLED ELECTRON  
SPIN STATES WITH SHOT NOISE DETECTION**

Yuanzhen Chen, Doctor of Philosophy, 2005

Dissertation directed by:   Richard A. Webb  
Department of Physics

We report experimental research into the possibility of using shot noise measurements to detect the entangled states of electron spins. The study is part of the effort towards the demonstration of the use of electron spins as quantum bits (qubits) for quantum computing and quantum information processing. Electrons are electrically injected into two neighboring quantum dots and interact with each other through the exchange coupling, after which they tunnel out of the dots and are incident on a beam splitter, which introduces quantum interference between electron states. Depending on the state of the electrons exiting the dots, the outgoing states of electrons scattering off the beam splitter are different, corresponding to different shot noise in the electrical currents flowing into the channels after the beam splitter. Our experimental data is consistent with most theoretical predictions and provides

initial evidence of electron spin entanglement.

A comprehensive study of the shot noise in mesoscopic semiconductor tunnel barriers is also reported. Besides the theoretically predicted full shot noise, suppressed and enhanced shot noise are also observed. Normal conductance measurements and numerical simulations are done to understand the shot noise deviation. Our study shows that shot noise in mesoscopic systems is extremely sensitive to the microscopic details, such as potential disorder and impurity configuration.

SEARCHING FOR ENTANGLED ELECTRON SPIN  
STATES WITH SHOT NOISE DETECTION

by

Yuanzhen Chen

Dissertation submitted to the Faculty of the Graduate School of the  
University of Maryland, College Park in partial fulfillment  
of the requirements for the degree of  
Doctor of Philosophy  
2005

Advisory Committee:

Professor Richard A. Webb, Chair/Advisor  
Professor Steven M. Anlage  
Professor H. Dennis Drew  
Professor Ichiro Takeuchi  
Professor Frederick C. Wellstood

© Copyright by  
Yuanzhen Chen  
2005

## ACKNOWLEDGEMENTS

First of all I want to thank my family for their constant support and encouragement during my time in graduate school. To my wife, Qing, who shared with me my happy and sad moments. Her company has made my graduate life a good memory even with so much hard work. To my parents, sister, and brother, whose support helped me get through some of the toughest moments in the last seven years.

I am very grateful to have had the opportunity to work with Professor Richard Webb. I want to thank him for his great help and patience. His enthusiasm for physics and dedication to research are models for all physicists.

I want to thank my labmates, Samir and Tarek. Their company and conversations made the lab a very nice environment for working. I specially thank Samir for his encouragement during the last two years. Part of my thesis work was the result of close collaboration with him. I also want to thank David for his help on my thesis writing.

I would like to thank all the dissertation committee members, Professors An-lage, Drew, Takeuchi, and Wellstood, for their time on reading my thesis and for

giving me very valuable suggestions. Professors Lobb and Anderson also deserve special thanks for reading the thesis and for their encouragement.

I want to give special thanks to Xuedong, our theoretical collaborator. Discussions with him clarified many confusing issues related to my experimental work. His work made me think deeper in physics.

The staff in the Center for Superconductivity Research were always very helpful. They kept the center as an enjoyable research environment. In the Physics Department, Lorraine was very efficient on helping solve technical problems in our lab, and Jane was always willing to help and made all the paperwork an easier task.

I want to thank all my friends for making my life outside the lab very delightful. They have brought me a lot of joyful moments besides those I had in my research. I want to give special thanks to Chi, Huizhong, Jianyang, and Jianguai, all PhD students in physics and astronomy. They kept me inspired and motivated. Without their help and encouragement, my graduate life would have been much more lonely.

# TABLE OF CONTENTS

List of Figures	vii
List of Tables	xiii
1 Introduction	1
1.1 Quantum computing . . . . .	2
1.2 Quantum entanglement . . . . .	4
1.3 Shot noise . . . . .	6
1.4 Detecting electron spin entanglement . . . . .	9
2 Mesoscopic Physics	10
2.1 Two dimensional electron gas . . . . .	10
2.2 Quantum point contact and quantum dot . . . . .	18
2.2.1 Split-gate technique . . . . .	18
2.2.2 Quantum point contact . . . . .	19
2.2.3 Quantum dots . . . . .	23
2.3 Shot noise . . . . .	30
2.3.1 General theory of shot noise . . . . .	30
2.3.2 Shot noise in mesoscopic systems . . . . .	34
3 Quantum entanglement	43
3.1 Entanglement . . . . .	43
3.1.1 A short history of studies of entanglement . . . . .	43

3.1.2	Properties of entangled states . . . . .	47
3.2	Entanglement of electron spins . . . . .	48
3.2.1	Using coupled quantum dots as an entangler . . . . .	48
3.2.2	Detection of entangled electron spins . . . . .	51
3.2.3	Related theoretical work . . . . .	58
4	Fabrication and Instrumentation	61
4.1	Sample fabrication . . . . .	61
4.2	Cryogenic amplifiers . . . . .	70
4.3	Dilution refrigerator wiring . . . . .	79
4.4	Noise reduction . . . . .	82
5	Shot noise of mesoscopic tunnel barriers	88
5.1	Overview . . . . .	89
5.2	Experimental data . . . . .	92
5.3	Numerical simulation and modelling . . . . .	106
5.4	Summary . . . . .	125
6	Shot noise study of quantum entanglement	127
6.1	Experimental preparation . . . . .	127
6.2	Experimental data . . . . .	138
6.3	Potential problems in the experiment . . . . .	147
6.4	Summary . . . . .	151

7	Conclusion and future work	153
7.1	Shot noise measurements . . . . .	153
7.2	Shot noise in mesoscopic tunnel barriers . . . . .	154
7.3	Quantum entanglement . . . . .	156
	Bibliography	158

## LIST OF FIGURES

2.1	Epitaxial structure and conduction band energy diagram of the wafer.	12
2.2	Schematic of a QPC.	19
2.3	Conductance of a QPC as the function of the gate voltage.	22
2.4	Lithography pattern and depletion region of a QD.	24
2.5	Potential profile through a QD.	26
2.6	Coulomb oscillation in a QD.	27
2.7	Potential profile in a QD as the bias is changed.	28
2.8	$ I  - V$ curve for a QD.	30
2.9	Shot noise in a QPC as a function of gate voltage.	40
3.1	Two electrostatically coupled quantum dots.	49
3.2	Schematic diagram of entanglement detection method of Burkard.	53
3.3	Different scattering patterns of two particles at a beam splitter.	54
4.1	Sample fabrication.	64
4.2	SEM picture of the intermediate and inner gates.	68
4.3	Schematic of the cryogenic amplifier.	73
4.4	FET noise models.	75
4.5	Calibration of the cryogenic amplifier at 4.2 K.	78
4.6	Dilution refrigerator wiring schematic.	80
5.1	SEM picture of a sample.	92

5.2	Noise of tunnel barriers as a function of dc current. . . . .	94
5.3	Shot noise as a function of dc bias. . . . .	96
5.4	Shot noise as a function of gate voltage. . . . .	99
5.5	Shot noise data and fit. . . . .	103
5.6	Enhanced shot noise. . . . .	105
5.7	Tunnel barriers with different localized states configurations. . . . .	108
5.8	Fano factor for tunneling through one localized state. . . . .	109
5.9	Fano factor for tunneling through two independent localized states. . . . .	111
5.10	Fano factor for tunneling through two localized states in series. . . . .	112
5.11	One localized state with two correlated tunneling paths . . . . .	114
5.12	Simulation results of $F$ as a function of $\beta$ when $\alpha = \gamma$ . . . . .	115
5.13	Simulation results of $F$ as a function of $\gamma$ when $\alpha = 1$ . . . . .	117
5.14	Time sequence of tunneling events. . . . .	118
5.15	Fit of the data in Fig. 5.4. . . . .	123
5.16	Gate voltage dependence of parameters. . . . .	124
6.1	SEM picture of a sample used in the entanglement experiment. . . . .	128
6.2	Experimental arrangement for the entanglement experiment. . . . .	133
6.3	Noise model of the system. . . . .	135
6.4	Background noise of the system. . . . .	137
6.5	Typical cross-spectrum data. . . . .	139
6.6	Beam splitter resistance and exchange gate resistance. . . . .	140
6.7	Reproducibility check and single dot partition noise. . . . .	143

## LIST OF TABLES

- 2.1 Electronic properties of the 2DEG in a GaAs/AlGaAs heterostructure. 17

# Chapter 1

## Introduction

This thesis reports on experimental research into the possibility of using shot noise detection in a transport measurement to detect the entangled states of electron spins. The study is part of an effort towards the demonstration of the use of electron spins as quantum bits (qubits) for quantum computing and quantum information processing.

The outline of this thesis is as follows. In this chapter, I discuss the motivation of the experimental work reported in this thesis by reviewing relevant progress in the study of quantum computing, quantum entanglement and shot noise in mesoscopic systems. The theoretical proposal on which my experimental work is based is also discussed briefly.

Chapter 2 introduces some basic mesoscopic physics. The electrical properties of the studied system and the transport properties of quantum point contacts and quantum dots are discussed. A general theory of shot noise and its application to mesoscopic systems is also discussed.

In Chapter 3, I first give a brief introduction to quantum entanglement and then discuss in detail the theoretical proposal for the generation and detection of entangled electron spins using coupled quantum dots and a beam splitter. Chapter 4 contains a discussion of the sample fabrication process and the experimental setup

used for the measurements reported in Chapters 5 and 6. The purpose, design, construction, and calibration of two cryogenic amplifiers is discussed in detail. Chapter 5 presents the results of shot noise measurements in mesoscopic tunnel barriers. Numerical simulation results are given for tunnel barriers with different microscopic details which affect charge transport and are used to explain the experimental data.

Chapter 6 reports on the first experimental results from the measurement of the shot noise from two coupled quantum dots to detect entangled electron spins. I give a detailed description of the experimental preparation and present data which provides initial evidence of electron spin entanglement. Some potential problems of this experiment are also discussed. The last chapter concludes with an overview of existing results and some future directions for research.

## 1.1 Quantum computing

The representation of information by classical quantities such as voltage levels in a microprocessor is well-known. Much less well-known is that information can be encoded in a two-state quantum system [1], such as: the two internal states of a trapped ion [2]; the two lowest energy levels of a current biased Josephson junction [3]; or the two spin eigenstates of an electron [4, 5] or atomic nucleus [6] in a magnetic field. A single quantum bit in this form has come to be known as a “qubit”. With two or more qubits it becomes possible to consider quantum logical gate operations in which a controlled interaction between qubits produces a (quantum mechanically coherent) change in the state of one qubit that is contingent upon the state of

another. These gate operations are the building blocks of a quantum computer. It is believed that if a quantum computer can be built, it will be able to solve some difficult problems in computational science, such as factorization of very large integers [7], searching one entry in a large unsorted database [8], and quantum modelling [9, 10].

Unique resources in quantum mechanics such as quantum superposition and quantum entanglement are essential for achieving the expected superior computing power of a quantum computer. For a system with  $N$  qubits, the set of all possible quantum states comprises a Hilbert space of  $2^N$ -dimensions. In general, a quantum computation process can be viewed as a unitary transformation in such a space. The resulting parallelism confers a quantum computer exponential information processing ability for certain types of computations.

Many physical systems have been proposed for implementing quantum computing and quantum information processing. Among the various proposals those based on solid state systems have mainly attracted interest because of their potential for being scaled up to create complex quantum circuits. One category of these systems is superconducting devices [11], such as Cooper pair boxes [12, 13], current biased Josephson junctions [3] and superconducting quantum interference devices (SQUID's) [14]. In these devices, two macroscopically distinct quantum states are used to represent a qubit. Another category uses microscopic states of real particles as qubits, for example, the nuclear spin states of a phosphorus atom [6].

In an electron spin-based quantum computing proposal by DiVincenzo *et al.*

[4, 5], the two spin eigenstates of a conduction electron are used as a qubit. Qubits can be electrically transported to desired places or be trapped in devices known as quantum dots, thus in principle they can be easily addressed. A quantum dot is simply a solid state device that traps a few electrons in a known location. It consists of a small island of electrons surrounded by several controlling gates and is usually connected to two electron reservoirs. By adjusting the voltage on the controlling gates, electrons are allowed to tunnel into and out of the quantum dot. The initialization of qubits can be realized by applying a global magnetic field which aligns all electron spins into one direction. In principle single qubit operations can be achieved by coherently manipulating electron states in a single quantum dot with carefully engineered local magnetic fields and/or external microwave pulses. Two qubit operations would be realized by using two electrically coupled quantum dots to introduce exchange couplings between two qubits. A universal set of quantum logic gates could then be constructed based on the above two types of operations.

## 1.2 Quantum entanglement

The search for experimental proof of quantum coherence between two or more macroscopically distinct quantum states in condensed matter systems has been a very active field over the past 20 years [15, 16, 17, 18, 19, 20, 21]. Much progress has been made in producing coherent superpositions between different states contained within a quantum system. For example, the existence of quantum coherence was first inferred and later clearly demonstrated by the experiments carried out in the energy

domain in a superconducting single electron transistor [22, 23, 24], in a persistent current superconducting loop device [20] and in a SQUID device [19]. Coherent temporal oscillations between two quantum states have also been observed in a single Cooper pair box [18] and in a current biased Josephson junction [17].

Recently the new focus has been to produce entangled quantum states. Quantum entanglement is a manifestly non-classical and non-local property of the quantum state of a composite system (e.g., two or more distinct particles) where the entangled composite state cannot be decomposed into a product of the individual states of local constituents. Therefore these objects are entangled no matter how far they are separated spatially. A classical example of entangled states is the singlet state of two electron spins.

The study of entanglement is important for both fundamental physics and practical applications. For example, pair-wise entangled electron spins (e.g., a singlet state) should be equivalent to Einstein-Podolsky-Rosen (EPR) pairs [25] whose main feature is their non-locality and should give rise to violations of Bell's inequalities [26, 27]. Testing Bell's inequalities is important for understanding the foundation of quantum mechanics. So far almost all tests that have been done were carried out with photons [28, 29, 30, 31], and no such test has been done for massive particles in a condensed matter environment. Condensed matter systems are inherently highly correlated many particle systems. Entanglement in such systems with strong interactions is an interesting and challenging topic.

The recent progress in quantum computing and quantum information process-

ing boosts the study of entanglement for practical applications. Spectroscopic evidence for entanglement between both the charge states of two coupled Cooper pair boxes [32] and two capacitively coupled Josephson junctions [33] has been reported, although the observed entanglement has not been tested in the context of Bell's inequalities and there are still debates on its nature. Conditional gate operations using coupled Cooper pair boxes have already been demonstrated [34]. The research on electron spin based quantum computing, however, has not reached this stage yet. The main effort is still on obtaining well characterized qubits. For example, semiconductor quantum dots containing one electron have been successfully fabricated only recently [35, 36] and coherent control of single electron states has not been achieved yet. How to entangle two electron spins remains an outstanding problem in this community.

### 1.3 Shot noise

In general, shot noise describes the fluctuations in any transport process in which the transported quantity has a discrete nature. For example, counting the number of photons arriving at a detector or the number of rain drops falling into a collector as a function of time reveals shot noise. For electrical transport in a conductor, shot noise is due to charge quantization of the current carrying particles. This is directly observed in the well known result for the full shot noise power spectrum density:  $2eI$ , where  $e$  is the electron charge and  $I$  is the time averaged current. If  $e \rightarrow 0$ , charge transport would be continuous and shot noise would vanish. Correspondingly, the

shot noise of the current at a normal-superconductor interface where the Andreev reflection mechanism [37, 38] dominates should be  $4eI$ , since the transport is now essentially the transfer of particles with a charge of  $2e$  [37]. On the other hand, theory predicts that the current in a system in the fractional quantum Hall regime is carried by quasi-particles with fractional charges [39], thus the electron charge  $e$  in the  $2eI$  should be replaced by the corresponding fractional charge [40]. Both predictions have been verified experimentally [41, 42, 43].

Experimentally, it is convenient to measure the power density of shot noise in the frequency domain. In almost all cases, the power density is frequency independent at low frequencies<sup>1</sup>, so shot noise is usually considered to be white. Mathematically, the noise power spectrum density of a current  $I(t)$  is defined as:

$$S(\omega) = \int_{-\infty}^{\infty} e^{-i\omega\tau} \left[ \int_{-\infty}^{\infty} I(t)I(t+\tau)dt \right] d\tau, \quad (1.1)$$

where  $\omega$  is the frequency. According to this definition, shot noise is sensitive to the temporal correlation of a current, or the correlation between consecutive charge transfer events. Compared to the time averaged current, shot noise contains additional information about the transport process. For example, shot noise has a power spectrum density of  $2eI$  only for transport processes that can be described by Poissonian statistics and usually deviates from that value in non-Poissonian processes.

---

<sup>1</sup>“Low frequencies” means frequencies lower than the inverse of the average transition time of one unit (e.g., one electron). For semiconductor devices, shot noise is white up to the GHz range or even higher.

However, a standard conductance measurement that detects the time averaged current cannot distinguish these different processes.

The deviation of shot noise from the Poissonian value  $2eI$  in mesoscopic conductors has attracted much interest in recent years [44]. For example, it has been shown theoretically and experimentally that due to the Pauli principle and Coulomb interaction between electrons, shot noise is often suppressed to below  $2eI$  [45, 46]. In some special cases, shot noise can also be much enhanced due to various mechanisms [47, 48]. Therefore the study of shot noise deviations helps illuminate details of the transport processes in mesoscopic conductors.

More recently, progress in the study of the shot noise in mesoscopic systems has been made by probing quantum statistics of particles in multi-terminal conductors [44, 49]. These studies have examined the effect of quantum statistical properties of a system on its shot noise. This new direction has much interplay with the field of quantum optics. Indeed, the theory of shot noise in mesoscopic physics borrows many ideas from quantum optics, where certain aspects of noise have been much better studied than in condensed matter systems. A few elegant mesoscopic experiments have recently demonstrated a fermionic analogy to high order quantum interference measurements in quantum optics [50, 51, 52]. This work will be discussed further in Chapter 3.

## 1.4 Detecting electron spin entanglement

DiVincenzo *et al.* [4, 5] have proposed using the spin eigenstates of single conduction electrons as qubits for quantum computing. They have suggested theoretically that the entanglement of two electron spins can be achieved by using two electrostatically coupled quantum dots as an entangler. To verify this possibility Loss *et al* [53] have suggested a scheme using shot noise measurements to detect entangled electron spin pairs. The basic idea is as follows. Electrons are electrically injected into two electrostatically coupled quantum dots and interact with each other through the exchange coupling. The electrons then tunnel out of the dots and traverse a beam splitter, which introduces quantum interference between the electron states. Depending on the type of entangled state of the electrons exiting the dots, the outgoing states of electrons scattering off the beam splitter are different, corresponding to different shot noise in the electrical currents flowing into the channels after the beam splitter. Thus the idea is that by measuring shot noise one can test the use of coupled quantum dots for generating entangled spin states.

In this entanglement detection proposal, the quantum statistical properties of the electron pairs exiting the two dots will determine the level of shot noise. This type of experiment belongs to the same class of measurements that probe quantum statistical properties in mesoscopic systems that I mentioned in the previous section. Therefore this experiment is interesting not only in the context of demonstrating entanglement but also in the sense that it enriches our understanding of shot noise in mesoscopic systems.

## Chapter 2

### Mesoscopic Physics

In this chapter, I give an introduction to transport processes in mesoscopic systems. Since this is a very broad field, only those subjects relevant to the experimental work reported in this thesis will be discussed. The first section is a brief review of the electrical properties of a two dimensional electron gas (2DEG) system in GaAs/AlGaAs heterostructures. The second section summarizes some recent experimental transport measurements obtained in these systems, focusing on quantum point contacts and quantum dots. The last section covers a general description of shot noise in mesoscopic systems.

#### 2.1 Two dimensional electron gas

In the last 50 years the general trend in microelectronics industry has been to minimize device sizes so that chips with higher density, operation speed, and more complex functionality could be made. This trend has been very successful. However, it is expected that progress will slow dramatically in the near future because of at least two factors: the limitations of the current lithography technology to produce even smaller features and the fact that classical transport theory does not adequately describe device operation at the nano-scale. As the dimension of devices approaches the deBroglie wave length of the charge carriers, the wave nature of the

particles dominates the transport characteristics. The first problem may be solved by developing new lithographic techniques or completely new ways of fabricating chips, such as the bottoms-up paradigm used in the chemical synthesis technology [54]. The second factor, however, is a more fundamental matter, which may or may not limit the performance of computers, but will certainly require new type of devices. The solution to this problem requires knowledge from the field of mesoscopic physics.

Mesoscopic physics involves the study of devices on a length scale between the microscopic atomic regime and the macroscopic classical regime. For transport in electronic mesoscopic devices, two important length scales are involved: the de-Broglie wavelength of electrons,  $\lambda$ , and the phase coherence length  $L_\phi$ , defined as the length scale over which the electron wave function maintains its phase coherence. In the classical regime, the typical size  $L$  of a device is much larger than  $L_\phi$ . In this limit, electrons can be treated as particles and classical transport theory works very well. For transport in these classical devices, electrons experience many scattering events caused by various interaction mechanisms and lose their phase information very fast, so their wave nature only introduces minor corrections to the classical transport theory. In the other limit where the device size  $L$  approaches the atomic scales, electrons must be described using quantum mechanics. Wave characteristics such as diffraction and interference become dominant. The transition region between these two limits is the realm of mesoscopic physics.

Low dimensional electronic systems based on semiconductor heterostructures

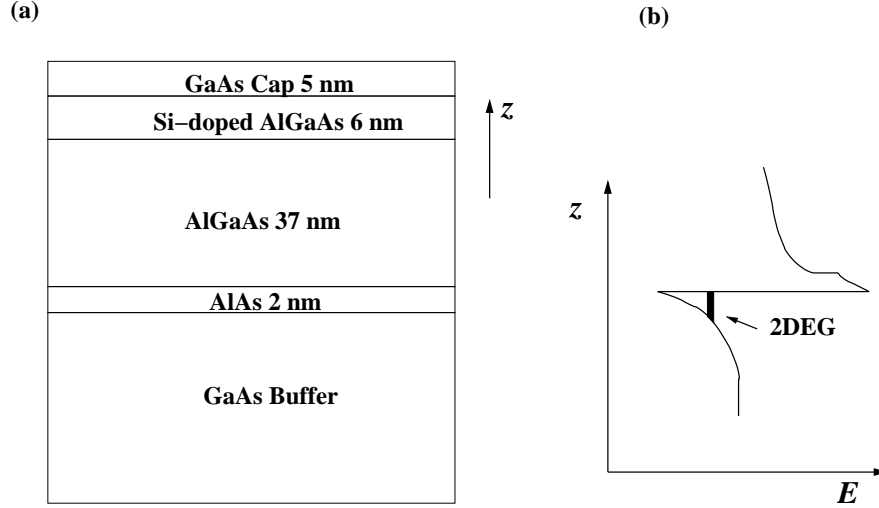


Figure 2.1: ((a) The epitaxial structure of the wafer used for the work in this thesis; (b) Conduction band energy diagram near the interface between the GaAs and AlGaAs. A two dimensional electron gas forms in the triangular well.

are ideal for studying mesoscopic phenomena. With the help of modern crystal growth and microelectronics fabrication techniques, the electrons in these systems are confined in one or more dimensions. Compared to metals, these systems usually have a lower electron concentration and smaller effective electron mass. This results in a large deBroglie wavelength (typically  $\sim 50$  nm) which is comparable to the size of the devices. Two well studied semiconductor heterostructure systems are the two dimensional electron gas (2DEG) formed in Metal Oxide Semiconductor Field Effect Transistors (MOSFETs) [55] and GaAs/AlGaAs heterostructures [56].

Figure 2.1 shows the epitaxial structure and conduction band energy diagram of the GaAs/AlGaAs heterostructure used for the experimental work reported in this thesis. The wafer I used was grown by Molecular Beam Epitaxy (MBE). Starting

with a standard GaAs wafer, a thick GaAs buffer layer is grown followed by 2.0 nm AlAs and 37.0 nm  $\text{Al}_{0.3}\text{Ga}_{0.7}\text{As}$  spacer layer. Next, 6.0 nm of doped  $\text{Al}_{0.3}\text{Ga}_{0.7}\text{As}$  (10 layers of  $\delta$ -doped Silicon with a dopant concentration of  $1 \times 10^{12} \text{ cm}^{-2}$  for each layer and separated by 0.6 nm of  $\text{Al}_{0.3}\text{Ga}_{0.7}\text{As}$ ) are grown followed by a final 5.0 nm GaAs cap layer. Due to the conduction band offset between GaAs and AlAs, a triangular potential well is formed at the interface between them. At low temperatures, electrons contributed by the silicon donors are trapped in this well. Typically electrons are confined within 1.0 nm in the  $z$  direction, so they can only move freely in the  $xy$  plane.

A 2DEG of this type is a many electron system. A full quantum mechanical calculation would take into account the lattice potential, confinement potential, electron-phonon interaction and electron-electron interaction, etc. However, this is neither practical nor necessary. As is well justified in many solid state systems, the independent electron picture is a good approximation. Within this picture, electrons are described by the following time-independent single particle Schrödinger equation:

$$\left[\frac{\hat{p}^2}{2m_e} + V_l(\vec{r}) + V_c(\vec{r})\right]\Psi(\vec{r}) = E\Psi(\vec{r}), \quad (2.1)$$

where  $m_e$  is the free electron mass and  $V_l(\vec{r})$  and  $V_c(\vec{r})$  are the lattice potential and confinement potential for a single electron. Since  $V_l(\vec{r})$  and  $V_c(\vec{r})$  have very different length scales<sup>1</sup>, they can be treated separately. In other words, the slowly varying

---

<sup>1</sup> $V_l(\vec{r})$  has the periodicity of the lattice while  $V_c(\vec{r})$  reflects the band bending due to band offset and usually varies on a much larger scale.

$V_c(\vec{r})$  can be viewed as a perturbation on  $V_l(\vec{r})$ . With this in mind, we proceed by solving the following equation:

$$\left[\frac{\hat{p}^2}{2m_e} + V_l(\vec{r})\right]\Psi(\vec{r}) = E\Psi(\vec{r}). \quad (2.2)$$

Solving this equation leads to the well known band structure in solids where  $\Psi(\vec{r})$  has the Bloch form [57]:

$$\Psi(\vec{r}) = u_{n\vec{k}}(\vec{r})e^{i\vec{k}\cdot\vec{r}}, \quad (2.3)$$

where  $u_{n\vec{k}}(\vec{r})$  has the periodicity of the lattice.  $n$  and  $\vec{k}$  are the band index and wave vector. They are good quantum numbers in a periodic potential. Another way to view the result is that  $\Psi(\vec{r})$  is a periodic wave function modulated by an envelope function, which is a plane wave.

For GaAs, it can be shown that the conduction band has the following dispersion relation [56]:

$$E_c(\vec{k}) = E_{c0} + \frac{\hbar^2\vec{k}^2}{2m^*}, \quad (2.4)$$

where  $E_{c0}$  is the bottom of the conduction band and  $m^* = 0.067m_e$  is the effective mass of electrons.

The next step is to treat the confinement potential  $V_c(\vec{r})$  as a perturbation and solve the full Schödinger equation 2.1 with the Bloch wave as a basis for expansion:

$$\Psi(\vec{r}) = \sum_{n,\vec{k}} c_{n,\vec{k}} u_{n\vec{k}}(\vec{r}) e^{i\vec{k}\cdot\vec{r}}, \quad (2.5)$$

Under the assumption of that  $V_c(\vec{r})$  is a slowly varying potential, equation 2.1 can be reformulated into the following single band equation [58]:

$$\left[ \frac{\hat{p}^2}{2m^*} + V_c(\vec{r}) \right] \Phi(\vec{r}) = E \Phi(\vec{r}), \quad (2.6)$$

where  $\Phi(\vec{r}) = \sum_{n,\vec{k}} c_{n,\vec{k}} e^{i\vec{k}\cdot\vec{r}}$  is the new envelope function. Notice that in equation 2.6 the effective mass  $m^*$  was used in the kinetic energy term and the  $V_l(\vec{r})$  term disappeared. The physical meaning is that the effect of the lattice can be fully taken into account by a single parameter  $m^*$  and  $V_c(\vec{r})$  only affects the envelope function. This is reasonable; since  $V_c(\vec{r})$  is a slowly varying potential, it should not alter the total wave function at the atomic scale.

Equation 2.6 can be decomposed into a one-dimensional equation in the  $z$  direction and an equation of free motion in the  $xy$  plane. As a result,  $\Phi(\vec{r})$  has the following form:

$$\Phi(\vec{r}) = Z_j(z) e^{i\vec{k}\cdot\vec{r}_{xy}}, \quad (2.7)$$

where  $Z_j(z)$  is the wave function in the  $z$  direction due to the confinement and  $\vec{r}_{xy}$  is the position vector in the  $xy$  plane.  $j$  is an index of solutions. The energy of the eigenstates are [56]:

$$E_{j\vec{k}} = E_{c0} + E_j + \frac{\hbar^2 \vec{k}^2}{2m^*}. \quad (2.8)$$

Here  $E_j$  is the quantized energy levels due to the confinement in the  $z$  direction and  $\frac{\hbar^2 \vec{k}^2}{2m^*}$  is the kinetic energy in the  $xy$  plane. From Eq. 2.8, we see that the dispersion relation is a set of paraboloids with the bottoms at  $E_j$ . For GaAs/AlGaAs heterostructures, the triangular well is very shallow and only one sub-band is formed (see Fig. 2.1).

So far I have not discussed the effect of scattering in the 2DEG. Depending on the magnitude of scattering, the transport in the system can be in different regimes: ballistic, diffusive but phase coherent and phase incoherent. Scattering mechanisms in semiconductor heterostructures include electron - phonon interactions, electron - electron interactions, interfacial scattering and impurity scattering. At very low temperatures, the electron-phonon interaction can be neglected. For MBE grown GaAs/AlGaAs heterostructures, the interface roughness is at the atomic scale; since the roughness is much less than  $\lambda$ , interfacial scattering is highly reduced. The high purity sources used in MBE growth help to guarantee a low impurity concentration in the 2DEG plane. In this case, the dominant impurity scattering comes from the silicon donors. With the modulation doping technique shown in Fig. 2.1, the scatterers are spatially separated from the 2DEG, so the scattering strength is much weaker than that in the 2DEG in MOSFETs, where scatters and carriers are not spatially separated. As a result, the 2DEG in GaAs/AlGaAs heterostructures usually has much higher electron mobility. With present day MBE technologies, mobilities as high as  $10^7$  cm<sup>2</sup>/V-s at 4.2 K can be achieved and correspond to a mean free path of 100  $\mu$ m.

At low temperatures, the 2DEG is a degenerate Fermi liquid. Once the electron concentration and mobility are known, key parameters such as Fermi energy and Fermi wave length can be calculated. Table 2.1 gives the analytical results and typical values of the electronic properties of a 2DEG in GaAs/AlGaAs heterostructures [56]. The electron concentration  $n$  and mobility  $\mu_e$  tabulated are the values appropriate for my experiments.

Table 2.1: Electronic properties of the 2DEG in the GaAs/AlGaAs heterostructure I used for experiments in this thesis.

	analytical	value	units
Effective mass	$m^*$	0.067	$m_e = 9.1 \times 10^{-31}$ kg
Density of states	$\rho(E) = m^*/2\pi\hbar^2$	0.28	$10^{11}$ cm <sup>-2</sup> meV <sup>-1</sup>
electron desity	$n$	2	$10^{11}$ cm <sup>-2</sup>
Fermi wave vector	$k_F = (2\pi n)^{1/2}$	1.12	$10^6$ cm <sup>-1</sup>
Fermi wavelength	$\lambda_F = 2\pi/k_F$	57	nm
Fermi velocity	$v_F = \hbar k_F/m^*$	1.9	$10^7$ cm/s
Fermi energy	$E_F = (\hbar k_F)^2/2m^*$	7	meV
Electron mobility	$\mu_e$	$4 \times 10^5$	cm <sup>2</sup> /V·s
Scattering time	$\tau = m^*\mu_e/e$	15.2	ps
Diffusion constant	$D = v_F^2\tau/2$	2800	cm <sup>2</sup> /s
Resistivity	$\rho = (ne\mu_e)^{-1}$	80	$\Omega$
Mean free path	$l = v_F\tau$	2.89	$\mu\text{m}$

## 2.2 Quantum point contact and quantum dot

Quantum point contacts (QPC) and quantum dots (QD) are among the simplest of mesoscopic devices and can serve as building blocks for more complicated structures. In this section, I discuss the transport properties of QPCs and QDs. The first subsection is on the split-gate technique [59, 60] used to fabricate mesoscopic samples. The next two subsections discuss QPCs and QDs respectively.

### 2.2.1 Split-gate technique

In a 2DEG, the electrons are confined to on a plane. To further control the dimensions of the sample, a way to achieve lateral confinement is required. Gating technology has long been used in semiconductor industry for this purpose. For example, surface gates are used in MOSFETs to change the effective channel width. For GaAs devices, a metal is deposited on the surface to form Schottky gates. A negative voltage (relative to the 2DEG) is then applied to the metal. Due to the Coulomb interaction, electrons under the metal will be depleted and a potential barrier is formed, thus constraining the electron flow. Since these gates are very close to the 2DEG, the potential profile in the 2DEG created by them mimics the pattern of the metal. By designing different patterns, one can achieve almost any desired sample configuration. With modern e-beam lithography, surface gates with features as small as 30 nm can be fabricated, i.e. down to the size scale as the Fermi wave length. This is why the 2DEG in GaAs/AlGaAs heterostructures is an ideal test bed for mesoscopic physics. Details of the e-beam lithography technique I used

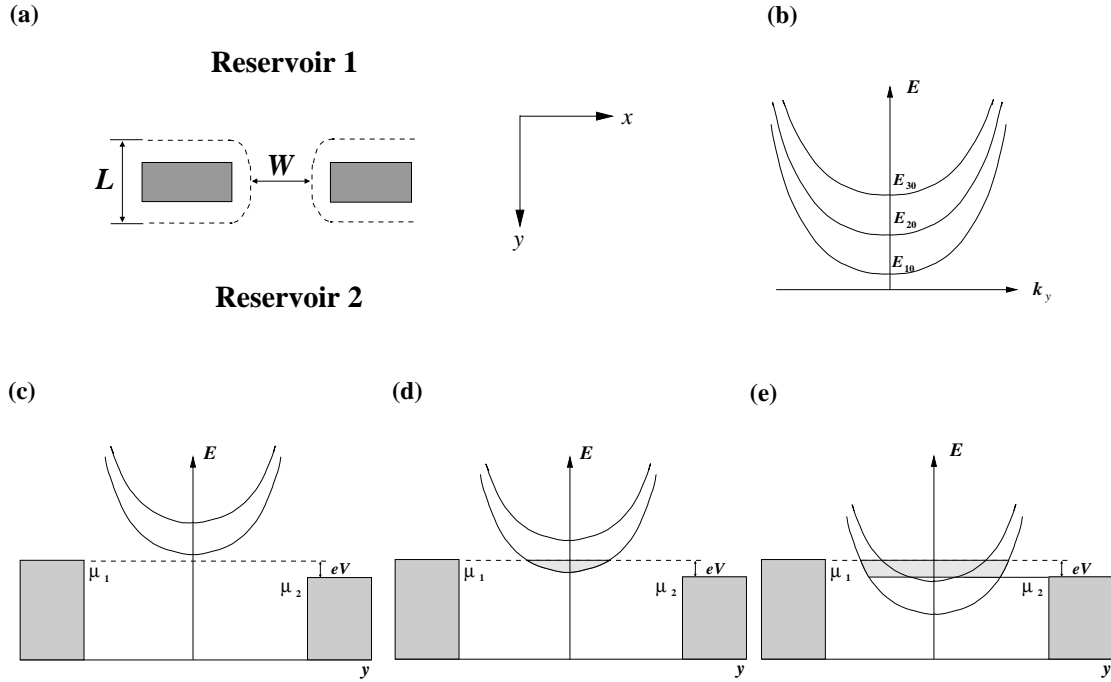


Figure 2.2: (a) Schematic of a QPC; lithography pattern (grey) and depletion region (between dashed curves); (b) subband electronic structure of a QPC; (c), (d) and (e) subbands with respect to the chemical potential in the reservoirs at different gate settings.

will be discussed in Chapter 4.

### 2.2.2 Quantum point contact

Figure 2.2(a) shows the schematic of a QPC. The dark area represents two metal gates on the sample surface. When a negative voltage is applied to the gates, potential barriers are formed underneath them. The dashed lines represent the edge of the electron depleted area. A channel of length  $L$  and width  $W$  is formed. Electron

flow between the two reservoirs can only happen through the channel. When  $L$  and  $W$  are comparable to the Fermi wave length, the wave nature of the electrons must be taken into account to understand the transport through such a QPC.

A simplified model treats this channel as quasi one dimensional [61]. If we further assume the confinement in the  $x$  direction due to the depletion is parabolic, the electronic properties of the channel can be calculated analytically. The Schödinger equation of electrons can be decomposed into two independent parts, one for each direction. In the  $x$  direction, the solution is a set of equally spaced energy states of a harmonic oscillator due to the parabolic confining potential. In the  $y$  direction, electrons can move freely, so the solution is a set of plane waves. As a result, the dispersion relation has the form (see Fig. 2.2(b)):

$$E(k_y) = E_{n0} + \frac{\hbar^2 k_y^2}{2m^*}, \quad (2.9)$$

where  $n$  is the index of the harmonic states. Another way to view this result is that a set of energy subbands are formed in the channel.

The bottom of each subband,  $E_{n0}$ , depends on the profile of the confining potential, which, in turn, depends on the gate voltages. Figure 2.2(c), (d) and (e) show how the relationship between the subbands and the chemical potential in the two reservoirs changes as a function of the gate voltage settings. Figure 2.2(c) represents the case of a very negative applied voltage, which generates a strong confinement, so all the subbands are above the chemical potential. In this case there are no energy states in the channel available for transmitting electrons. Figure

2.2(d) and (e) represent the cases of more positive gate voltages, so the subbands are lowered and one or two of them are now available for electron transmission. In either case, the energy states within the window of the bias ( $eV$ ) applied across the QPC can fully transmit electrons<sup>2</sup>. The total current carried by one subband can be calculated as following:

$$\begin{aligned}
 I &\approx \frac{2e}{h} \int_{\mu_2}^{\mu_1} dE \rho_{1D}(E) v(E) f(E) \\
 &= \frac{2e^2}{h} V,
 \end{aligned} \tag{2.10}$$

where  $\rho_{1D}(E)$  and  $v(E)$  are the 1D density of states and velocity of electrons;  $f(E)$  is the Fermi-Dirac function. For the second line in equation 2.10, note that  $\rho_{1D}(E) \propto E^{-1/2} \propto v(E)^{-1}$ , so  $\rho_{1D}(E)v(E)$  is a constant. According to equation 2.10, the conductance of one subband at zero magnetic field is  $G_0 = 2e^2/h$  where the factor of 2 takes into account electron spin degeneracy. If we consider the change from Fig. 2.2(c) to (e), as the subbands are lowered, more and more subbands become available for conduction. Each time the bottom of a subband moves below  $\mu_1$ , the total conductance  $G$  of the QPC should increase by  $G_0$ . As a result, a quantized  $G$  as a function of  $V_g$  is expected (see Fig. 2.3(a)).

The quantized conductance plateaus in a QPC were first observed in 1988 in a GaAs 2DEG by B. J. van Wees *et al.* [61] and Wharam *et al.* [62], as shown in Fig. 2.3(b). The slope at each step is due to thermal smearing.

---

<sup>2</sup>Since  $W$  and  $L$  are much less than the mean free path (which is  $2.9 \mu\text{m}$  according to table 2.1), electrons are assumed to transport ballistically, or there is no scattering in the channel.

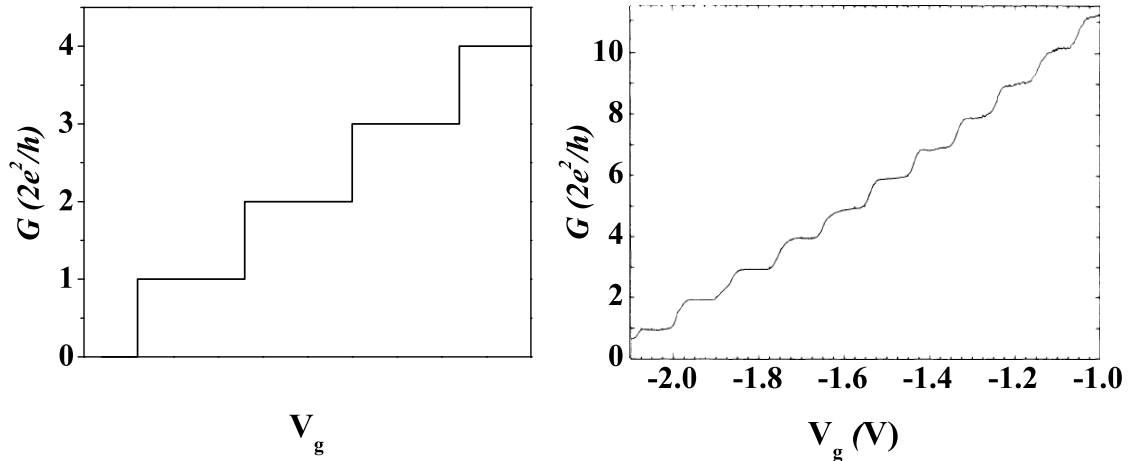


Figure 2.3: (a) Theoretical prediction of the conductance of a QPC as the function of the gate voltage; (b) experimental data (from Ref. [61]).

While it is able to capture the main features of the experimental data, the above model is certainly oversimplified. For example, it predicts that  $G$  should go to zero suddenly at some  $V_g$ , corresponding to the point at which the bottom of the lowest subband aligns with  $\mu_1$ . This never happens in a real system for two reasons. First, at finite temperatures the energy width of any subband is increased by an amount proportional to temperature. Second, tunneling between the two reservoirs causes smearing even at zero temperature.

Thus far the transport I have discussed has involved occupation of the energy states in the subbands. However, transmission of electrons is possible even when there is no available state in the channel. In such a case, the gates are so negatively charged that effective  $W$  decreases to zero or the QPC is pinched off. Electrons in both reservoirs see a potential barrier. At low temperatures, the only possibility

for electron transmission is tunneling through the barrier. A significant difference between this process and the transport through channel states is that electrons now encounter a potential barrier so scattering occurs. Nevertheless, both processes can be characterized by a parameter  $T_j$ , the transmission coefficient of the QPC, which is the transmission probability of electrons incident on the QPC. For  $0 < T_j < 1$ , electrons tunnel through the QPC and for  $T_j = 1$ , electrons are fully transmitted through the channel states without scattering.

The scattering by the potential barrier is phase coherent, so the Landauer-Büttiker theory [63, 64, 65, 66] of mesoscopic transport applies. The total conductance  $G$  of a QPC is related to its transmission coefficients by:

$$G = \frac{2e^2}{h} \sum_j T_j, \quad (2.11)$$

where  $j$  is the index for subbands (more details can be found in section 2.3.2).

### 2.2.3 Quantum dots

Figure 2.4(a) shows a schematic of the lithography pattern and depletion region of a quantum dot. The black regions are metal gates. The dashed line represents the edge of the horizontal depletion layer. The small pool of electrons enclosed by all gates forms a QD. The two point contacts formed by the upper and lower pairs of gates control the coupling between the QD and the drain and source reservoirs. The middle pair of gates (also called plunger gates) are used to change the overall potential of the QD without significantly changing the tunneling rates through the

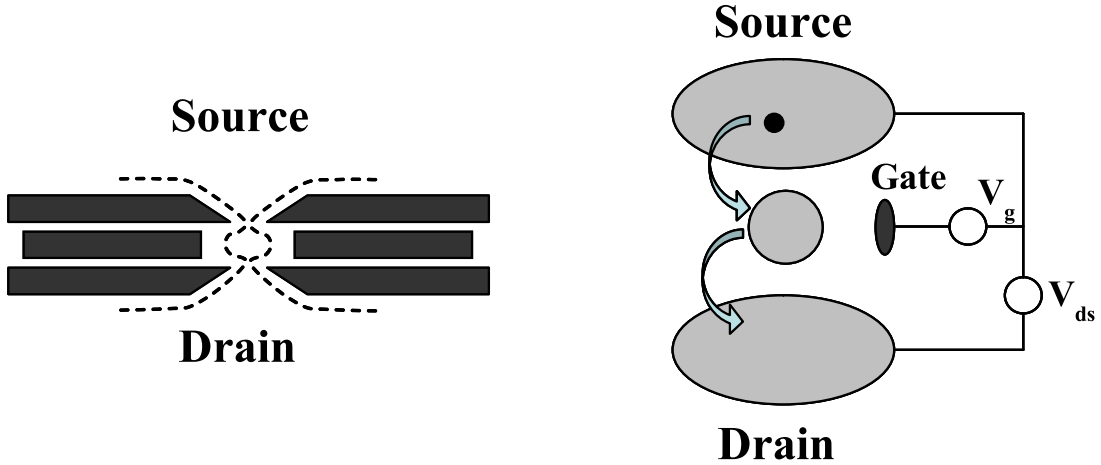


Figure 2.4: (a) Top view of lithography pattern and depletion region of a QD; (b) a circuit model of a QD.

two point contacts.

Classically a QD can be viewed as a small island of  $N$  electrons with a total capacitance  $C$ . Electrons transfer can happen between the QD and the two reservoirs. The plunger gate is capacitively coupled to the QD. There are three contributions to the total capacitance  $C$ ; the self capacitance of the QD, capacitive coupling between the QD and the reservoirs, and coupling to the plunger gates. Figure 2.4(b) shows an equivalent circuit model of a QD. Due to the Coulomb interaction, adding one electron to a QD requires certain amount of charging energy. In the classical model discussed here, the charging energy is  $E_C = e^2/2C$ , so the Coulomb interaction is characterized by a single parameter  $C$ .

The classical model ignores the details of the electronic states in the QDs. While this usually works fine for QDs in metallic systems provided they are not

too small, the situation is more complicated for QDs fabricated in the 2DEG in semiconductors. From Table 2.1, the density of states in the 2DEG is  $\rho(E) = m^*/2\pi\hbar^2$ , so the average energy spacing between the states in these QDs is about  $\Delta E = 1/(\rho(E)A) = 2\pi\hbar^2/(m^*A)$ , where  $A$  is the area of the QD. The typical size of my QDs is on the order of 100 nm, so  $\Delta E$  is  $\sim 0.03$  meV. At temperatures below 100 mK (so  $k_B T < 8.6 \mu\text{eV}$ ) this spacing becomes observable. In metallic QDs,  $\Delta E$  is usually much smaller and can be neglected due to the very large  $\rho(E)$ .

Now let us consider transport in a QD in which both the charging energy  $E_C$  and the level spacing  $\Delta E$  are taken into account. Usually two types of transport measurements are performed. In the first, a small bias voltage (usually a few  $\mu\text{V}$ ) is applied across the QD and the conductance is measured as a function of the gate voltage  $V_g$ . This type of measurement is also called a spectroscopic measurement. The second standard transport measurement is the current-voltage  $I - V$  characteristic of the dot. I first discuss the spectroscopic measurement.

Figure 2.5 shows the potential profile through a QD at zero temperature with different gate voltages, where a small bias  $eV$  is applied. Figure 2.5(a) shows the case of Coulomb Blockade [67, 68, 69] where  $eV \ll E_C = e^2/2C$ . In this range, there are no energy states available between  $\mu_1$  and  $\mu_2$  for electrons to tunnel through, so the electron transport is blocked. The gap between the lowest available state and the electrochemical potential  $\mu(N)$  of the QD is  $\Delta E + E^2/2C$ .

By tuning the gate voltage  $V_g$ , one can change the electrostatic potential of the QD, thus shifting the energy levels. Figure 2.5(b) shows the case when one

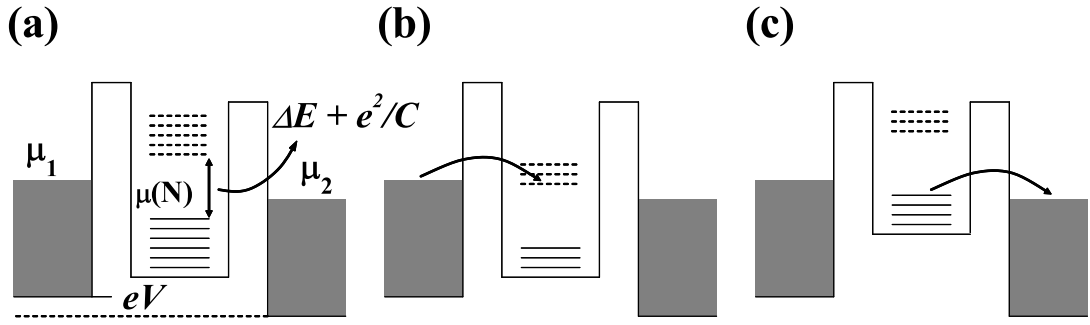


Figure 2.5: Potential profile through a QD. (a) Coulomb blockade; dashed lines show unfilled levels, solid lines filled levels, with splitting caused by Coulomb blockade; (b),(c) degenerate point where the QD has either  $N$  or  $N + 1$  electrons.

energy level is within  $\mu_1$  and  $\mu_2$  so one electron can tunnel from the left reservoir onto the QD. When such a tunneling occurs, the electrostatic potential of the QD will be raised by an amount of  $e^2/2C$  and the overall potential profile is shown in Fig. 2.5(c). In this case, the QD has one more electron, but that extra electron can now tunnel into the right reservoir. Figure 2.5(b) and (c) are for the same  $V_g$ . At this specific gate voltage, the system is in two degenerate states, one with  $N$  electrons and the other one with  $N + 1$  electrons. The switching between these two states as electrons tunnel on and off generates a current through the QD. As  $V_g$  is swept across this value, a conductance peak appears.

To be more quantitative, the electrochemical potential of the QD is given by [70]:

$$\mu(N, V_g) = E_N + \frac{(N - N_0 - 1/2)e^2}{C} + e \frac{C_g}{C} V_g, \quad (2.12)$$

where  $E_N$  is the  $N$ th single particle state and  $C_g$  is the capacitance between the QD and the plunger gate.  $N_0$  is the number of electrons at zero gate voltage. At the degeneracy points discussed above, one has:

$$\mu(N, V_g) = \mu(N + 1, V_g + \Delta V_g). \quad (2.13)$$

Solving equation 2.12 with this constraint gives:

$$\Delta V_g = \frac{C}{eC_g}(\Delta E + \frac{e^2}{C}), \quad (2.14)$$

where  $\Delta E = E_{N+1} - E_N$  is the level spacing between two single particle states. As a result, plotting the conductance  $G$  vs  $V_g$  yields a series of peaks separated by  $\Delta V_g$ . This phenomenon is called Coulomb Oscillations [68, 71, 72].

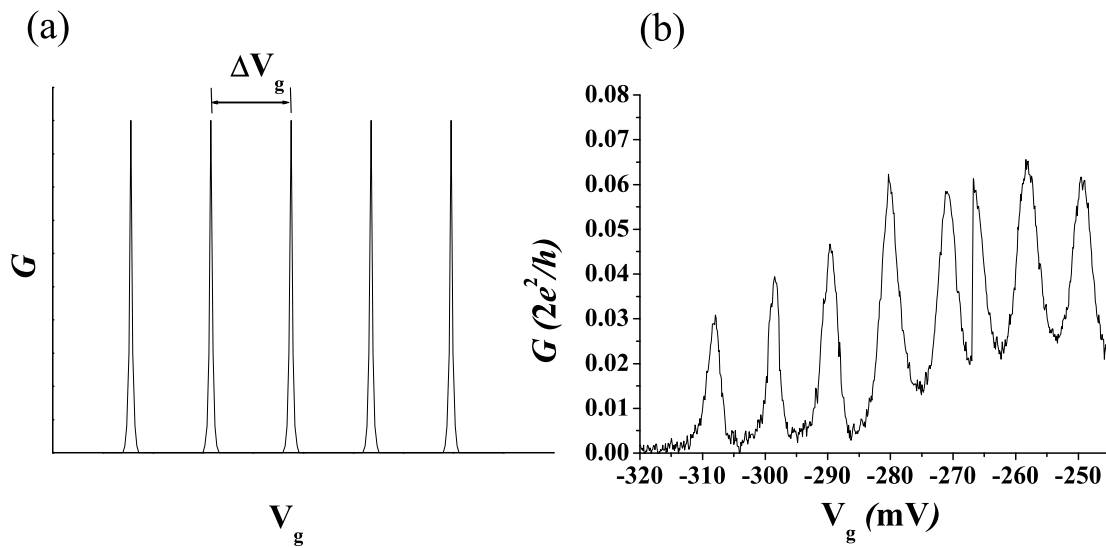


Figure 2.6: Coulomb oscillation in a QD. (a) theoretical prediction; (b) experiment result.

Figure 2.6 gives the theoretical prediction along with my experimental measurements of Coulomb Oscillations. The experimental data was taken on a QD fabricated in the GaAs/AlGaAs heterostructure discussed in section 2.1. The data shows many interesting features not present in the simple model discussed here, such as the gate voltage dependence of the peak height and line width. For a more detailed discussion of the cause of these effects, I refer the reader to a review on QDs [73].

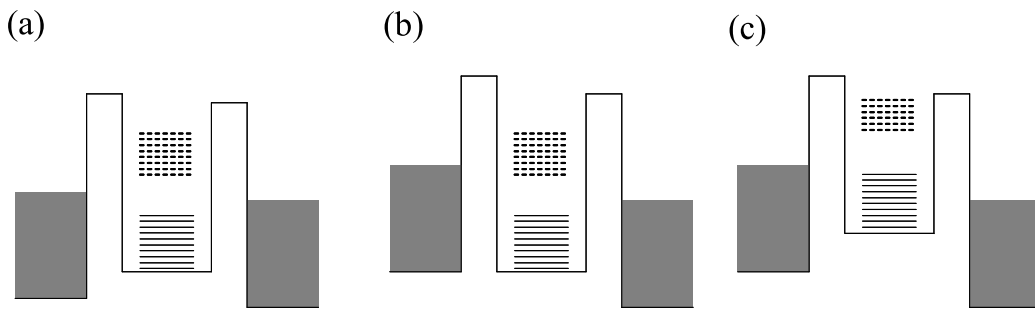


Figure 2.7: Potential profile in a QD as the bias is changed. (a) Coulomb blockade; (b) at the bias where one charge state is available; (c) at the same bias as in (b) but with one electron tunneled into the QD.

Besides the spectroscopy measurement, an  $I - V$  measurement can also be used to study the electronic structure of a QD. The difference between these two is that in the spectroscopy method, the energy levels in the QD are shifted with respect to the two reservoirs, while in the  $I - V$  measurement the chemical potential of the reservoirs change. Figure 2.7 shows the potential profile in a QD when the bias

voltage is changed. Figure 2.7(a) is the case of Coulomb Blockade. Due to the Coulomb charging energy, there are no energy states available for tunneling. As the bias is increased to overcome the charging energy, some energy states now become available for transport, as shown in (b). Electrons can tunnel through any of these levels. However, once one electron tunnels, the potential of the QD will be changed by an amount of the charging energy, as shown in (c). As a result, other electrons in the left reservoir will be blocked until one electron in the QD tunnels into the right reservoir, then the potential profile changes back into (b). Equivalently, we can say that increasing the bias opens a conducting channel, thus an increase in the conductance should be observed. As the bias is increased further, more channels will be available. Each time when such a channel becomes available, the conductance of the QD increases, so a pattern called Coulomb staircase [70, 74, 75] is produced if the current through the dot is plotted as a function of bias voltage.

Figure 2.8 shows an  $I - V$  curve measured for a QD fabricated on my wafer. The absolute value of the current is plotted on the vertical axis. As can be seen, the conductance increases in a stepwise manner, although the steps are noticeably rounded.

Further analysis [73] reveals that the Coulomb staircase should only show up for QDs having two very asymmetric tunnel barriers (with very different impedance). For symmetric QDs, the  $I - V$  curve shows a Coulomb blockade with a size of  $e/2C$  around the zero bias. Ideally, outside of the blockade regime the  $I - V$  relation is simply Ohmic [73].

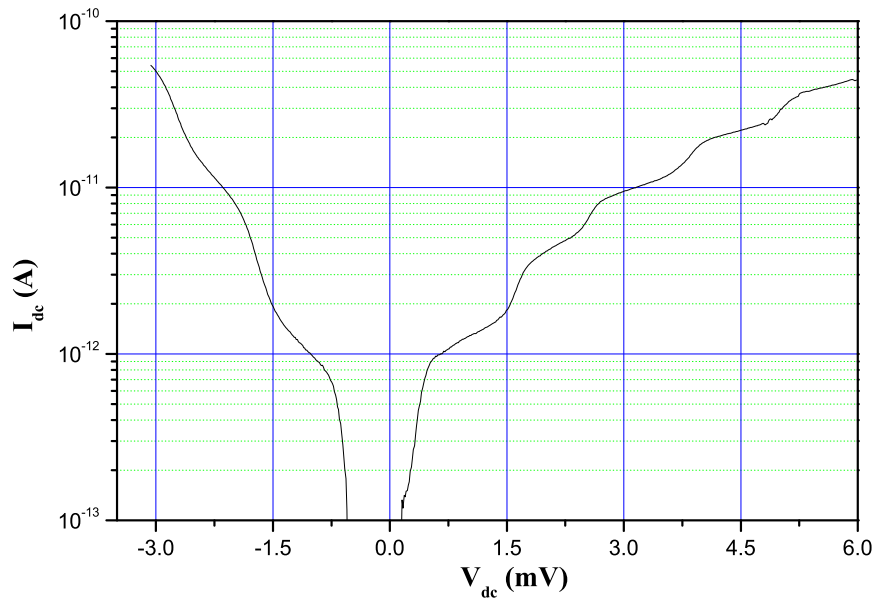


Figure 2.8:  $|I| - V$  curve for a QD.

## 2.3 Shot noise

In this section, I discuss the shot noise theory that is related to the experimental work reported in this thesis. The first subsection gives a general discussion of shot noise. The second subsection is on the shot noise in mesoscopic systems.

### 2.3.1 General theory of shot noise

Shot noise is the time-dependent fluctuations present in a current  $i(t)$  due to the discreteness of the charge carriers. That is, it originates from the discrete nature of the current carrying particles. In the following, I will first discuss a general noise theory and then apply it to the case of shot noise.

While noise is a random fluctuating quantity in the time domain, perhaps the

most natural way to study it is by analyzing its Fourier spectrum. Mathematically, the Fourier spectrum of a random signal is calculated for an infinite time interval. Experimentally, the current  $i(t)$  is always measured over a finite time interval  $[-T, T]$ , so I will calculate the spectrum for the interval  $[-T, T]$  and take the limit as  $T \rightarrow \infty$  at the end. Thus

$$i(t) = \begin{cases} i_T(t) & \text{if } -T < t < T \\ 0 & \text{otherwise} \end{cases}$$

The Fourier transform is:

$$I_T(f) = \int_{-\infty}^{\infty} i(t)e^{-i2\pi ft} dt. \quad (2.15)$$

Since  $i(t)$  is real,  $I_T(-f) = I_T^*(f)$ , where  $*$  represents the complex conjugate.

According to Parseval theorem[76], one has:

$$\int_{-\infty}^{\infty} i^2(t) dt = \int_{-\infty}^{\infty} |I_T(f)|^2 df, \quad (2.16)$$

As  $T \rightarrow \infty$ , both sides of the above equation go to infinity, so one considers the time averaged noise<sup>3</sup> (or the mean square value):

$$M[i^2(t)] = \frac{1}{2T} \int_{-T}^T i^2(t) dt = \frac{1}{2T} \int_{-T}^T |I_T(f)|^2 df. \quad (2.17)$$

---

<sup>3</sup>For a random variable  $i(t)$  with a zero mean value, its standard deviation is  $\overline{i^2} - \bar{i}^2 = \overline{i^2}$ . By definition, this is the total noise associated with  $i(t)$ , which is shot noise in the case considered here.

With this equation, the total noise can be calculated once the Fourier spectrum  $I_T(f)$  is known. A new quantity, power density, is defined as:

$$S(f) = \lim_{T \rightarrow \infty} \frac{1}{T} |I_T(f)|^2 \quad 0 < f < \infty. \quad (2.18)$$

Note here  $f$  is limited to positive values since experimentally only a one-sided power spectrum can be measured. As a result, the average factor changes from  $2T$  to  $T$ .  $S(f)$  has the units of  $A^2/Hz$ . It represents the total noise power in a unit bandwidth.

It can be shown [76] that for the case where electrons arriving at a detector have a Poissonian distribution, the power density has the following form:

$$S(f) = 2eI, \quad (2.19)$$

where  $I = \overline{i(t)}$  is the time averaged value of the current. This is the well known form of full shot noise.  $S(f)$  is a constant at all frequencies, namely, a white noise. This result can be generalized to any random process governed by Poissonian statistics. On the other hand, for non-Poissonian processes the power density have other values. This will be shown shortly.

To better understand the physical meaning of shot noise, I will consider the cross-correlation of two random variables  $i_1(t)$  and  $i_2(t)$ :

$$\Gamma(\tau) = \frac{1}{2T} \int_{-\infty}^{\infty} i_{1T}(t) i_{2T}(t + \tau) dt. \quad (2.20)$$

The Fourier spectrum of  $\Gamma(\tau)$  is:

$$X(f) = \int_{-\infty}^{\infty} e^{-i2\pi f\tau} \left[ \frac{1}{2T} \int_{-\infty}^{\infty} i_{1T}(t) i_{2T}(t + \tau) dt \right] d\tau. \quad (2.21)$$

After completing the integration, one has:

$$X(f) = \frac{1}{2T} I_{1T}(f) I_{2T}^*(f). \quad (2.22)$$

$X(f)$  is also called the cross-spectrum of  $i_1(t)$  and  $i_2(t)$ .  $X(f)$  and  $\Gamma(\tau)$  both characterize the correlation between the two signals at different time. Now consider a special case where  $i_1(t) = i_2(t)$ , then  $\Gamma(\tau)$  and  $X(f)$  describe the auto-correlation of  $i(t)$ . By taking the  $T \rightarrow \infty$  limit and combining equations 2.22 and 2.18, one has:

$$X(f) = \frac{1}{2} S(f). \quad (2.23)$$

The power density of a random variable is related to its auto-correlation function. For a Poissonian process,  $X(f) = \frac{1}{2} S(f) = eI$ . The Fourier transform of  $X(f)$ , which by definition is  $\Gamma(\tau)$ , is thus a  $\delta$  function. The physical meaning of this result is that for a Poissonian process  $i(t)$ , there is no correlation between its values at different times. Equivalently, one can say things the other way around: if  $\Gamma(\tau)$  has a finite width, then  $X(f)$ , thus  $S(f)$ , will not have a white spectrum. In an electron transport process, if for any reason there is a correlation between the motion of electrons at different times, the shot noise will then deviate from a white spectrum of  $2eI$ . In this sense, shot noise detection is a powerful tool to explore the temporal correlation of the motion of electrons.

So far I have only discussed the auto-correlation function. This is enough for two terminal devices where there is only one continuous current present, or only one random variable. For multiple terminal devices, however, currents in different terminals are different variables. In such a case, the cross-correlation, or the cross spectrum, between them carries important information about the system [44]. The entanglement experiment reported in this thesis belongs in this category. The theory of this experiment will be discussed in the next chapter.

### 2.3.2 Shot noise in mesoscopic systems

Historically, shot noise was first studied theoretically in a vacuum tube by Schottky [77]. When a vacuum tube is operated in the saturation region<sup>4</sup>, the emission of electrons at the cathode is a Poissonian process. Electrons come off of the cathode randomly and independently, so there is no correlation between the tube current at different times. According to the result in section 2.3.1, this process yields a white shot noise with a power density of  $2eI$ . However, if the tube is operated in the space charge regime where electrons accumulate around the cathode, the shot noise is found to be less than  $2eI$  [76]. This is because Coulomb interaction between the electrons in the cathode and the space charge regulates the emitting process. It turns out that such a regulation can introduce a correlation between the emitting time of subsequent electrons. As a result, the emission is now a sub-Poissonian

---

<sup>4</sup>In the saturation region, the tube current is independent of the voltage between the cathode and anode. Microscopically, all electrons coming out of the cathode will be swept into the anode, so no space charge accumulation happens around the cathode.

process, and thus less random fluctuations in the tube current are observed.

In mesoscopic systems, the Coulomb interaction between electrons becomes extremely important due to the small size scale. For example, as discussed in section 2.2, the Coulomb interaction determines the transport in QDs. The Coulomb blockade effect correlates consecutively tunneled electrons. This reduces the shot noise significantly. Another essential feature of mesoscopic devices fabricated in 2DEGs is that at low temperatures, the system is degenerate Fermi liquid, so the effect of the Pauli principle becomes important. According to the Pauli principle, each occupied state in the Fermi liquid contains exactly one electron and there are no fluctuations in the occupation numbers. This introduces another type of regulation for transport which suppresses shot noise [44]. In the following, I will first discuss the general formalism of the shot noise in mesoscopic samples and then give some examples.

Shot noise in mesoscopic samples can be theoretically studied by different methods, such as the master equation approach [78, 79], the Green's function method [38, 80] or the scattering approach [44]. The Landauer-Büttiker transport theory [63, 64, 65, 66] for mesoscopic samples has been a great success, and a scattering approach based on such a theory is a very natural way to understand the shot noise in mesoscopic systems.

The basic idea of the Landauer-Büttiker formulation is to relate the conductance of a mesoscopic sample to its scattering properties, for example, to the scattering matrix. Phase coherent transport is assumed for the system under study. This is

especially suitable for mesoscopic samples since their typical dimensions are smaller than the phase coherence length. Another important feature is that this formulation does not use ensemble averaging over many samples with different scattering sites. Instead, it concerns individual samples. Classical transport theory usually ignore the microscopic details of samples because it averages over all possible impurity configurations and takes the limit as the size of the system goes to infinity (ensemble averaging), so some sample specific information is inevitably lost in this process. For macroscopic samples, this procedure works well and only small corrections are needed. On the other hand, in mesoscopic samples the sample specific fluctuations can be of the same order of magnitude as the quantities (conductance, etc.) measured. In such a case ensemble averaging makes no sense.

Within the second quantization formalism, this approach first defines creation and annihilation operators for electron states. The operators of current and shot noise can then be constructed and evaluated. The shot noise operator is defined as the temporal correlation between currents, and its Fourier spectrum is the noise power density. The transport in the sample is viewed as a scattering process where incoming electrons are coherently scattered to the outgoing channels. Incoming and outgoing currents are related by the scattering matrix of the system, which can be obtained by a quantum mechanical calculation. I will not discuss the full mathematical details here. Instead, I will give some basic results and refer the reader to a review article [44] for details.

At zero temperature and for a small voltage bias, the conductance of a two

terminal device is:

$$G = \frac{2e^2}{h} \text{Tr}[t^\dagger(E_F)t(E_F)]. \quad (2.24)$$

Here  $t(E_F)$  is the transmission matrix of the sample, which relates the amplitude of the outgoing states to that of the incoming states. For low bias, the matrix only needs to be evaluated at the Fermi energy  $E_F$ . The matrix  $t^\dagger t$  can be diagonalized. The eigenvalues  $T_n$  are usually called the transmission coefficients, each of them having a value between 0 and 1. The conductance can then be rewritten in the form:

$$G = \frac{2e^2}{h} \sum_n T_n, \quad (2.25)$$

which is identical to equation 2.11.

At zero temperature the shot noise of a two terminal device has the form:

$$S(f) = \frac{4e^2}{h} \text{Tr}(r^\dagger r t^\dagger t) e|V|, \quad (2.26)$$

where  $r$  is the reflection matrix and  $V$  is the applied bias voltage.  $r$  also has a set of eigenvalues  $R_n$  which satisfy  $R_n = 1 - T_n$ , so the shot noise can be rewritten as:

$$S(f) = \frac{4e^3|V|}{h} \sum_n T_n(1 - T_n). \quad (2.27)$$

According to this result, neither closed ( $T_n = 0$ ) nor fully transmitting ( $T_n = 1$ ) channels (also called open quantum channels) contribute to shot noise. For closed

channels, no transport of electrons happens, while for the other case, electrons get transmitted without any scattering. In either case, no shot noise should be generated. The maximum contribution comes from those channels with  $T_n = 1/2$ .

If all channels are nearly closed such that  $T_n \ll 1$ , then:

$$S(f) \approx \frac{4e^3|V|}{h} \sum_n T_n = 2e\langle I \rangle, \quad (2.28)$$

where  $\langle I \rangle$  is the time averaged current and the equation 2.24 is applied to get the final result. This is the well known form of full shot noise.

At finite temperatures, a device exhibits both shot noise and thermal noise. Within the scattering approach, these two noise sources can be united in one form:

$$S = \frac{e^2}{\pi\hbar} [2k_B T \sum_n T_n^2 + eV \coth\left(\frac{eV}{2k_B T}\right) \sum_n T_n(1 - T_n)]. \quad (2.29)$$

In the limit that  $V \rightarrow 0$ ,  $S \rightarrow 4k_B T G$  ( $G$  is given by Eq. 2.25), so the thermal noise is recovered. For the case of  $T_n \ll 1$  for any  $n$  (which means a very resistive device according to equation 2.25),  $S$  reduces to the following form:

$$S = \frac{e^3 V}{\pi\hbar} \coth\left(\frac{eV}{2k_B T}\right) \sum_n T_n = 2eI \coth\left(\frac{eV}{2k_B T}\right). \quad (2.30)$$

Again,  $S = 4k_B T G$  at  $V = 0$  and  $2eI$  for  $eV \gg k_B T$ . Equation 2.30 thus describes the transition from the thermal noise to full shot noise for a resistive device (e.g., a tunnel barrier with an impedance well above the resistance quanta  $h/2e^2$ ).

A convenient factor to measure shot noise is the Fano factor defined as:

$$F = \frac{S}{2eI}. \quad (2.31)$$

It is the ratio between the measured shot noise power density and the full shot noise power density for the same current. For the case discussed above,

$$F = \frac{\sum_n T_n(1 - T_n)}{\sum_n T_n}. \quad (2.32)$$

From this we see that the Fano factor is always expected to be less than 1, namely, suppressed shot noise.

The transport in a QPC was studied in section 2.2.2. The total conductance is given by equation 2.11. In the plateau regime, all conducting channels have a transmission coefficient of 1. According to equation 2.27, there should be no shot noise generated on a plateau. In a real system, the transition from one plateau to the next occurs over a finite range in the gate voltage and this should give a rise to a nonzero value for the shot noise. Figure 2.9 shows the theoretical prediction and the first experimental evidence of shot noise suppression in a QPC by Reznikov *et al.* [81].

I note that Reznikov *et al.*'s experimental data is not in quantitative agreement with the theory. The authors addressed this issue in their paper. Nevertheless, the suppression of shot noise at the plateau regime is clearly demonstrated. A more precise measurement was later given by Kumar *et al.* [82]. They found excellent agreement between their results and the theory. The experimental data validated two main predictions of the theory (see equation 2.29): the suppression of Poissonian

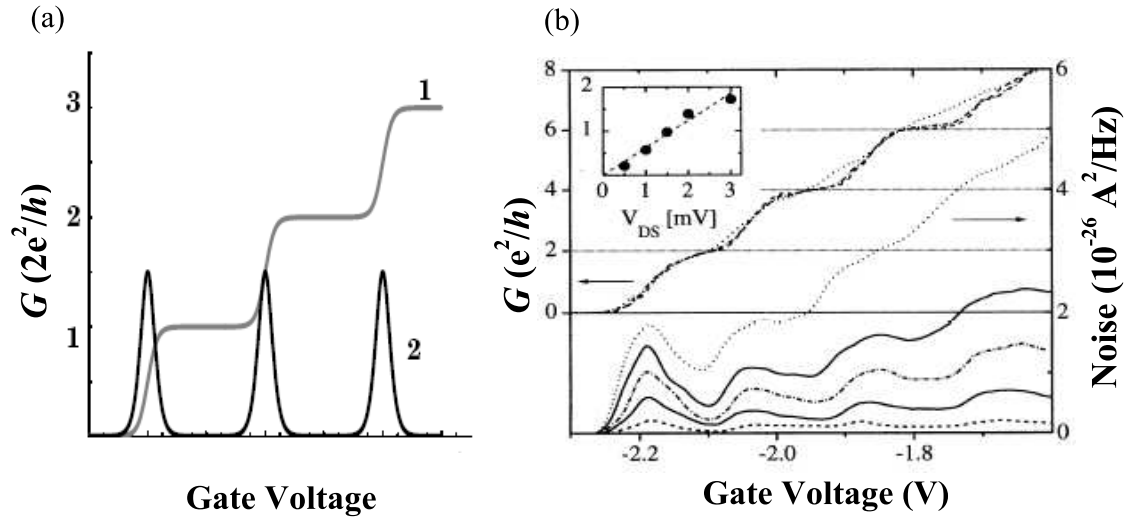


Figure 2.9: Shot noise in a QPC as a function of gate voltage: (a) theoretical prediction; curve 1 is the conductance in unit of  $2e^2/h$ ; curve 2 is the shot noise in unit of  $e^3|V|/3\pi\hbar$ . (b) First experimental evidence of suppressed shot noise in a QPC, measured by Reznikov *et al.* The upper plot is the conductance and the lower plots are the shot noise. Different curves correspond to different bias voltages.

shot noise and the transition from thermal noise to shot noise as the bias voltage is increased.

While the scattering approach is suitable for describing many mesoscopic systems in which the independent electron picture is valid, it certainly does not include the Coulomb interaction between electrons. Thus it is not surprising that this method is not applicable in the cases where electron-electron interaction can not be neglected, such as in a QD. The shot noise in a QD is much more complicated than in a QPC. In general, in strongly correlated systems there is no universal approach to study shot noise. In addition, different approaches may apparently lead to different or even contradictory results [44]. Experimentally, there is no systematic study on this subject yet. In the following, I will outline some theoretical results.

Similar to the conductance discussed in section 2.2.3, the shot noise of QDs can be also studied in the linear ( $V \ll e/C$ ) and non-linear regime. Wang *et al.* [83] investigated shot noise in semiconductor QDs in the linear regime, both analytically and numerically. Their analytical result shows that as a function of the gate voltage, the Fano factor  $F = 1$  (Poissonian shot noise) everywhere except at the gate voltages corresponding to the position of the conductance peaks where shot noise is suppressed. Their numerical result shows that a suppression of  $F$  below  $1/2$  is possible. However, other people argued that  $F \ll 1/2$  is quite unlikely to happen in the simple model of Coulomb blockade [44]. This is still a subject in debate.

In the non-linear regime, depending on whether a Coulomb staircase is present, the shot noise is quite different. The case without a staircase was studied by Ko-

rotkov *et al.* [84] using the master equation approach. Their results show that the shot noise is zero in the Coulomb blockade regime and is Poissonian at the onset of current. For high voltages the Fano factor is:

$$F = \frac{\Gamma_1^2 + \Gamma_2^2}{(\Gamma_1 + \Gamma_2)^2}, \quad (2.33)$$

where  $\Gamma_{1,2}$  are the tunneling rates through the two barriers. Hershfield *et al.* [85] have studied the case when a Coulomb staircase is present. They showed that in the plateau regime  $F$  is one, and near the degenerate points (where the conductance has a stepwise change)  $F$  has the form of equation 2.33. According to these results, the shot noise of a QD in the non-linear regime is always between  $F = 1$  and  $F = 1/2$ .

From the discussion above, it is very obvious that the shot noise from quantum dots is still a field with many unsolved problems. An accepted theoretical model has not been produced. In addition, very few experimental results are available, especially for QDs in semiconductor materials. This lack of reliable experimental data is due to several technical problems. The first is that measuring shot noise at small currents is an extremely difficult task. The second is that shot noise may be extremely sensitive to microscopic details in the sample (potential disorder and impurities) and these details are very difficult to characterize in mesoscopic samples. In Chapter 5, I will discuss these issues further.

## Chapter 3

### Quantum entanglement

The main motivation for the work reported in this thesis is performing an experiment that would demonstrate the entanglement of electron spins. In this chapter I discuss the theoretical background of such an experiment. The first section covers some basic aspects of quantum entanglement, including a short history of entanglement studies, some important theoretical results, and a brief review on existing experiments. In the second section I discuss the proposal upon which my experiment is based.

### 3.1 Entanglement

#### 3.1.1 A short history of studies of entanglement

Quantum mechanics is one of the pillars of modern physics. It has achieved great success in various branches of physics because it allows us to understand experimental phenomena that could not be described using classical physics. In spite of this, many people believe it remains one of the most mysterious scientific theories ever invented. How to interpret predictions based upon quantum mechanical calculations has been frequently debated from the beginning.

The surprising behavior implied by quantum mechanics can be best illustrated with a few experiments in which any classical theory cannot interpret the observed

results. For example, in a double slit interference experiment, the result can only be explained when each particle is assumed to go through both slits simultaneously. Quantum mechanics explains this phenomenon with the concept of wave-particle duality: wave and particle are two complementary and necessary elements of the nature of microscopic particles; the behavior of these particles (wave-like or particle-like) depends on the type of measurements performed. Quantum mechanics does not answer the question of “What kind of reality (in the classical sense) is the origin of the wave-particle duality?”, but rather emphasizes that the duality is the reality. In the microscopic world, the effort of trying to recover a classical picture usually fails. Quantum mechanics simply refuses to answer certain questions, or, according to the orthodox Copenhagen interpretation, these questions may not be meaningful in the microscopic world. Einstein and his followers tended to think that the refusal of quantum mechanics to answer these questions meant that it was not a complete theory and thus could not provide a complete description of reality. On the other hand, the Copenhagen interpretation argues that objective reality in the classical sense simply does not exist, so the refusal to answer certain questions is actually a great virtue of quantum theory instead of being a defect. According to the complementarity principle, one can only learn part of the knowledge of a microscopic system at one time (e.g., the position or the momentum of a particle, but not both), not due to technical difficulties but rather to intrinsic limits: there is simply no such state with both definite position and momentum.

However, in 1935 **E**instein, **P**odolsky and **R**osen (EPR) wrote a paper [25]

in which they proposed a thought experiment showing how to generate quantum states with definite values for both members of a pair of complementary variables. A system of two particles was considered in this paper. At some initial time the particles interact with each other for a while, then they are spatially separated so that the interaction between them is turned off. Due to the interaction at the beginning there is a correlation between the position and momentum of the two particles even when they are separated. By measuring the position or momentum of one particle the experimenter can deduce those of the other one. Since the experimenter has the choice of which quantity to measure, the other particle must have definite values for both position and momentum prior to the measurement. This conclusion disagrees with the complementarity principle.

Against this attack on quantum mechanics, Bohr argued that the assumptions of the EPR argument were questionable [86]. Later, inspired by the EPR paradox, Schödinger proposed the famous *gedanken* cat experiment [87]. He also gave a name to the strange correlation existing in an EPR system: quantum entanglement. David Bohm reformulated the EPR problem by considering systems where discrete quantities [88], such as spin, were studied, so there were only a finite number of possible results, unlike the case of continuous variables such as position and momentum.

At that time there was no way to implement the thought experiment in the EPR argument, and the debate remained at a philosophical level until 1964 when John Bell published the first of his two papers on this problem [26, 27]. These

two papers significantly changed the field of the foundations of quantum mechanics. The main results are now referred to as Bell's inequalities. These inequalities study the correlation between the results of independent measurements performed on two EPR particles. Quantum mechanics should violate these inequalities, while all other possible theories based on the assumptions made in the original EPR argument should satisfy the inequalities. This result is very general in the sense that it does not depend on things like the properties of the particles and the details of their interaction. The significance of Bell's result is that the profound difference between quantum mechanics and classical theories can be expressed in a direct quantitative way and becomes experimentally testable.

Many experiments have been implemented to test Bell's inequalities [28, 29, 30, 31]. In all tests, the inequalities were violated, which means quantum mechanics is correct. Most tests were carried out with photons and to date no similar work has been done in any condensed matter system. In solid state systems particles tend to strongly interact with each other so it is nearly impossible to isolate particles to generate EPR pairs. In addition, in strongly correlated systems quantum states are likely to suffer more from decoherence. Both factors make testing Bell's inequalities in condensed matter systems a formidable task.

Recently the entanglement problem has attracted more attention due to the rising interest in quantum computing and quantum information processing. Unique resources in quantum systems, such as superposition and entanglement, are believed to be essential for achieving the expected superior computing power of a quantum

computer. A few experiments have demonstrated (not in the context of testing Bell's inequalities) entanglement in condensed matter systems [32, 33]. For quantum computing applications, a demonstration of basic quantum gate operations with entangled states is the current goal.

### 3.1.2 Properties of entangled states

Entanglement is a non-classical property of the quantum states of a multiple particle system. An entangled state cannot be decomposed into a product of the states of the constituents. For example, the singlet and one of the triplets of two electron spins are entangled states:

$$\psi = |\uparrow\downarrow\rangle \pm |\downarrow\uparrow\rangle. \quad (3.1)$$

These states cannot be written as the product of the spin states of two electrons. In this sense, an entangled state is actually one quantum object although it contains two particles. If the two particles are non-interacting, an EPR pair is generated.

Let us consider the singlet of two electron spins. Suppose the two electrons are denoted as  $A$  and  $B$  and their spins are to be measured by two independent sets of apparatus. In principle, it is always possible to separate the two electrons so far away that the measurement performed on one electron does not disturb the other electron. This can be guaranteed by the fact that no signal can be transmitted faster than the speed of light.

Before any measurement both electrons are not in a single spin eigenstate. Suppose we make a measurement of electron  $A$  and spin up is found, then after this measurement electron  $B$  must be in the spin down state, although  $B$  is not affected by this measurement. This correlation between  $A$  and  $B$  implies that there is some sort of quantum non-locality in the system. Due to this non-locality, an entangled state must be always treated as one entity no matter how far away the two particles are separated. The fact that the measurement performed on one particle has no dynamical effect on the other particle does not mean the two entangled particles are independent.

The test of Bell's inequalities is more complicated than the simple measurement discussed above. I will not discuss the details here but refer the reader to the literature [89].

## 3.2 Entanglement of electron spins

### 3.2.1 Using coupled quantum dots as an entangler

In recent years many physical systems have been proposed as potential candidates for quantum computing and quantum information processing. Loss and DiVincenzo have proposed a quantum computing scheme using electron spins as qubits and quantum dots to manipulate the spins [4, 5]. Each electron has two spin eigenstates, so it is a qubit given by nature. This type of qubits can be easily initialized by applying a global magnetic field and waiting a time  $T_1$  for the system to relax to the ground state. Single qubit operations can be realized by applying carefully

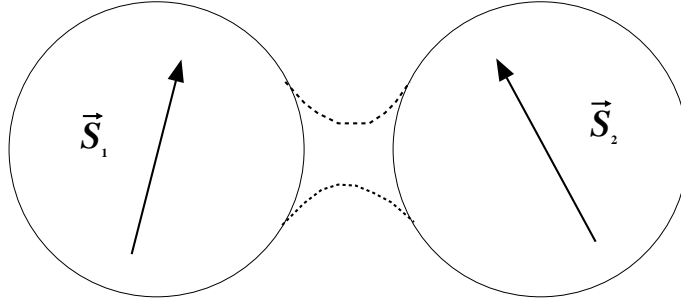


Figure 3.1: Two electrostatically coupled quantum dots, each containing one electron spin. A gate (not shown in the figure) controls the tunnel barrier separating the two dots. Intra-dot tunnelling becomes possible when the gate voltage is pulsed to be low (dashed line) and prohibited when that voltage is high (solid line).

engineered local magnetic fields or external microwave pulses. Two-qubit gate operations can be realized by using the exchange interaction between neighboring spins. With the single qubit and two-qubit operations, a set of universal quantum gates required for quantum computing can be constructed. Electron spins usually have a longer decoherence time compared to other degrees of freedom such as orbital states [90, 91]. This is a welcome feature for quantum computing since in general quantum computation processes are expected to be very fragile to decoherence.

As discussed in the last section, entanglement is essential for quantum computing and quantum information processing. In the spin-based scheme, entangled spin states are generated by the exchange coupling between two neighboring spins.

Experimentally, two quantum dots, like those discussed in Chapter 2, can be fabricated very close to each other (see Fig. 3.1). One electron spin is placed in each dot, denoted as  $\vec{S}_1$  and  $\vec{S}_2$ . Each dot has a Coulomb charging energy  $u = e^2/2C$

where  $C$  is the capacitance of the dots. The tunneling between the two dots is controlled by the voltage on a gate (not shown in the figure) separating them. When the potential barrier formed by the gate is high so that no tunneling is allowed (solid lines in Fig. 3.1), the two spins are held in stationary states without evolution in time. If the barrier is low (dashed lines in Fig. 3.1), the two spins interact with each other through the exchange coupling Hamiltonian <sup>1</sup>:

$$H(t) = J(t)\vec{S}_1 \cdot \vec{S}_2, \quad (3.2)$$

where  $J(t) = 4t_0^2(t)/u$  is the strength of the exchange coupling between the two electron spins. Here  $t_0(t)$  is the intra-dot tunneling matrix element. In general,  $J(t)$  is a time varying quantity determined by the gate voltage settings and external magnetic fields. For the static case in which  $J(t)$  is a non-zero constant, the two coupled spins have four eigenstates: a singlet and three triplets. The energy difference between the triplets and singlet is defined as  $J = E_t - E_s$ . Depending on the sign of  $J$ , the system could have the singlet or triplets as its ground state(s). Thus by carefully tuning the coupled quantum dots, it is possible to use this system to generate entangled electron spin states.

---

<sup>1</sup>Besides the exchange coupling, there is also a direct term of Coulomb interaction between the two electrons. The effect of that term will be briefly analyzed in section 6.3

### 3.2.2 Detection of entangled electron spins

It has been shown theoretically that a coupled quantum dot system can be used as an entangler for electron spins. An outstanding problem in this field is to demonstrate this experimentally. This is really a measurement problem, that is, how to detect spin entangled states. Performing an EPR test would be an ideal demonstration. However, to date there is no efficient way to detect the spin state of single electrons. In general, up-to-date nano-technology is not efficient enough to carry out even fairly complicated manipulations of the states of single electrons. Alternatively, Burkard *et al.* have proposed a scheme of performing ensemble measurements on many entangled electron spin pairs [53]. This scheme utilizes the quantum statistical properties of entangled electrons and the resulting shot noise properties of electrical currents.

It is well known that bosons, such as photons, exhibit a phenomenon called "bunching" behavior when the correlation between particle currents is measured [92]. In other words, bosons tend to aggregate. On the other hand, fermions are expected to avoid each other due to the Pauli principle and Coulomb interaction (for charged particles), thus showing an "anti-bunching" behavior [93]. This difference originates from the different quantum statistical properties of bosons and fermions.

The correlation experiments on photons are the famous HBT (Hanbury Brown and Twiss) type of measurements in quantum optics [92], named after the work by the two pioneers who measured the correlation of the intensity of two light beams from a distant star to determine its angular diameter. In contrast to the Michelson-

type of measurements in which the interference of the electrical fields  $\vec{E}$  of light is measured, the HBT measurements detect the correlation of the intensity  $I \propto |\vec{E}|^2$  of light. Sometimes the Michelson-type detection is called the first order correlation, while the HBT type is called the second order correlation. Quantum mechanically,  $\vec{E}$  represents the wave function of photons, while  $I$  is proportional to the density of probability currents, or the number of photons. Thus the HBT measurement can be also viewed as the correlation of the fluctuations of particle numbers, which is basically equivalent to shot noise detection. The result is very sensitive to the quantum statistical properties of the light source, therefore the HBT measurement has been used extensively to study the statistics of different light sources.

In principle, the HBT measurement can also be used to study the statistics of fermionic systems. Recently, a few elegant experiments have been carried out in 2DEGs in GaAs/AlGaAs heterostructures [50, 51, 52]. The “anti-bunching” of electrons in non-entangled states has been demonstrated. Naively one would think that electrons should exhibit “anti-bunching” under any circumstance. However, as pointed out by DiVincenzo and Loss [94], “bunching” and “anti-bunching” are phenomena occurring in space, so the actual behavior of an electronic system should be sensitive, in the absence of spin-scattering processes, only to the symmetry of the spatial part of the overall wave function. While the overall wave function is always anti-symmetric for multiple electrons, the spatial part can have different symmetries; symmetric for the singlet state and anti-symmetric for the triplets. Thus one expects a “bunching” behavior for the spin singlet and an “anti-bunching” behavior for

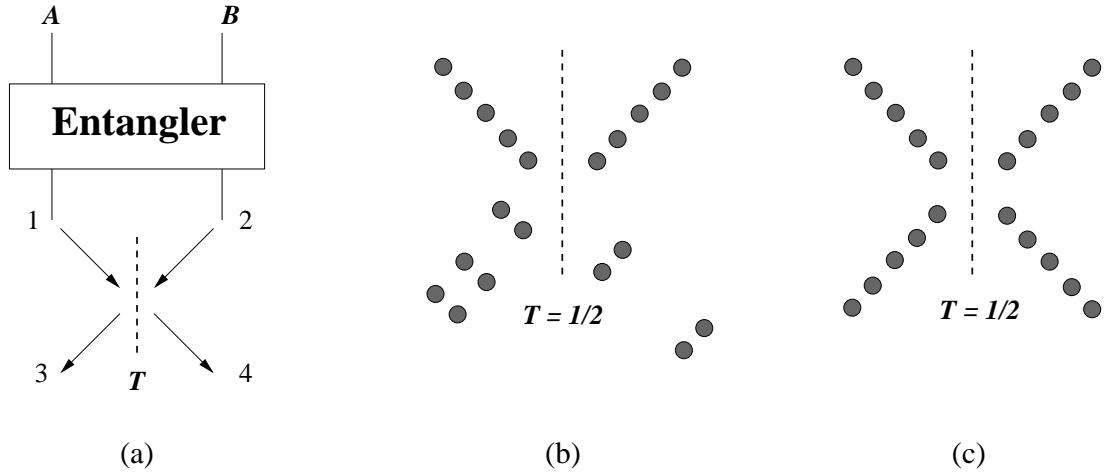


Figure 3.2: (a) Schematic diagram of entanglement detection method proposed by Burkard *et al.*; (b) collision of electron pairs in the singlet at a  $T = 1/2$  beam splitter; (c) collision of electron pairs in the spin triplet states.

triplets. The “bunching” and “anti-bunching” behaviors manifest themselves in a measurement of the correlation between particle currents, namely, in a shot noise measurement. The entanglement detection scheme by Burkard *et al.* is based on the above analysis. In the following, I will discuss the microscopic picture and experimental implementation of such a scheme.

In Fig. 3.2(a) an entangler, such as the coupled quantum dot system shown in Fig. 3.1, generates entangled electron pairs and injects them into leads 1 and 2, one electron in each channel. A beam splitter is inserted after the entangler to introduce quantum interference effects between the two electrons. A beam splitter is a tunneling barrier for electrons, characterized by its transmission probability  $T$ . It is basically the quantum point contact discussed in Chapter 2. Electrons incident on

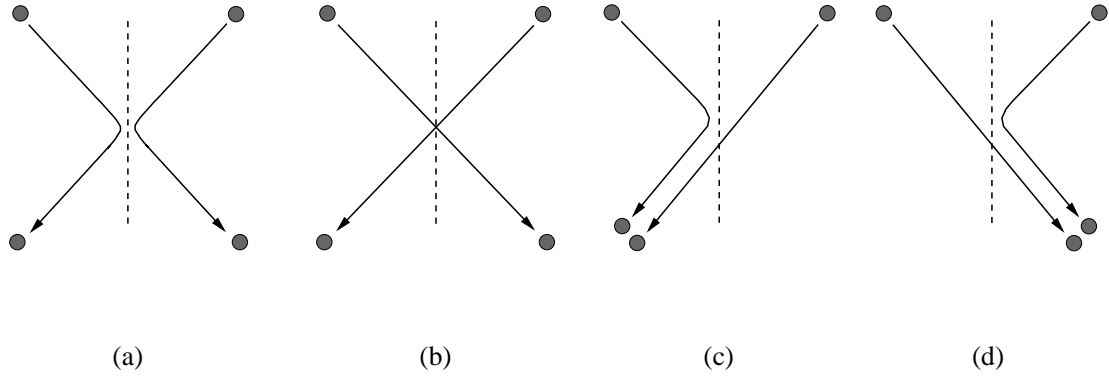


Figure 3.3: Different scattering patterns of two particles at a beam splitter.

the beam splitter are coherently scattered into leads 3 and 4 with certain probability. Within this picture, the transport through the beam splitter can be studied by the scattering approach discussed in Chapter 2. The wavefunctions of the outgoing particles in leads 3 and 4 are related to those of the incoming particles in leads 1 and 2 by the scattering matrix of the beam splitter. Consequently, electron pairs coming out of the entangler in different states will have different scattering patterns at the beam splitter, thus leading to different fluctuations in the electrical currents in leads 3 and 4.

In order to see why this is true, one can consider the special case where  $T = 1/2$ . Each particle incident on the beam splitter has a probability of  $1/2$  of being transmitted or reflected. For a pair of particles, there are four different scattering patterns, as shown in Fig. 3.3. If the two particles are distinguishable, the four patterns are independent events and each occurs with a probability of  $1/4$ . For identical particles, however, Figs. 3.3 (a) and (b) become indistinguishable.

According to quantum mechanics, they correspond to one event and its probability can be found by applying the Feynman rule: add the probability amplitude of (a) and (b) and then take the squared absolute value. At  $T = 1/2$ , the quantum mechanical calculation shows that for bosons, the probability amplitudes of Fig. 3.3 (a) and (b) have the same magnitude but opposite sign, so the probability of (a) and (b) happening is zero. As a result, two bosons are always scattered into the same lead, as shown in Figs. 3.3 (c) and (d). In other words, bosons exhibit “bunching” behavior.

For fermions the situation is more complicated. As pointed out earlier in this section, for two electrons in the singlet state, their spatial wavefunction is symmetric. If only the spatial part is concerned, the two electrons are expected to behave like bosons. A quantum mechanical calculation confirms this analogy [53], so for two electrons in the singlet state, they exhibit “bunching” behavior. On the other hand, for electrons in a triplet state, the probability amplitudes of Figs. 3.3 (c) and (d) are zero. As a result, the two electrons are always scattered into different leads exhibiting “anti-bunching” behavior.

If the entangler in Fig. 3.2(a) continuously generates electron pairs in the singlet state, the outcome after the beam splitter will look like Fig. 3.2(b) according to the analysis above, while for triplets the result is shown in Fig. 3.2(c). By measuring the average currents in leads 3 and 4, one finds no difference between Figs. 3.2(b) and (c) since on average the same number of electrons are scattered into both channels. However, it is obvious that Fig. 3.2(b) and (c) are different

if the fluctuation pattern in the current is concerned. For example, in Fig. 3.2(c), the current in each channel is composed of a series of electrons arriving at equally spaced times, so there should be no fluctuations in the current and the shot noise should be fully suppressed. Thus by measuring shot noise, one can distinguish Figs. 3.2(b) and (c), and therefore the cases of singlet and triplets.

To quantify the difference one needs to apply to the system the scattering approach for shot noise discussed in Chapter 2. The scattered states can be calculated with the help of the scattering matrix of the beam splitter. Based on that, current operators can be constructed and the shot noise can be calculated. Assuming the average current in both channels is  $I$ , the power density of the shot noise is [53]:

$$S_{34}(\omega) = -S_{33}(\omega) = -S_{44}(\omega) = \begin{cases} -4eIT(1-T) & \text{singlet} \\ 0 & \text{triplets} \\ -2eIT(1-T) & \text{independent electrons} \end{cases} \quad (3.3)$$

Here  $S_{34}(\omega)$  is the cross spectrum of the currents in leads 3 and 4, defined as  $I_3(\omega)I_4^*(\omega)$ , and  $S_{ii}(\omega)$  ( $i = 3,4$ ) is the shot noise of each channel, defined as  $I_i(\omega)I_i^*(\omega)$ . The case of independent electrons corresponds to the situation where two independent currents (to realize this, one can turn off the exchange interaction by tuning gate voltage settings) are incident on the beam splitter and each current contributes to the total shot noise independently. According to equation 3.3, the enhanced shot noise is a signature of the single state, while a fully suppressed shot

noise indicates the presence of any of the triplet states.

So far I have shown that by performing shot noise measurements one can distinguish the singlet from the triplets generated in an entangler such as a coupled quantum dot system. This is not, of course, a direct proof of entanglement. In such a measurement one cannot gain direct knowledge about the correlation between the spin states of the two electrons, but only deduce indirectly the information about the entangled states. However, I want to point out that two features in such an experiment resemble two crucial conditions required in a test of Bell's inequalities: turning off the initial interaction between particles and keeping the system away from any decoherence before a measurement. In the shot noise measurement discussed here the exchange interaction between the two electrons is turned off after they leave the quantum dots. This is true even when they are scattered at the beam splitter. In addition, in the absence of a spin-orbit coupling and other spin scattering mechanisms, the spin states of the two electrons are conserved.

A real test of Bell's inequalities for the entangled states generated by a coupled quantum dot system can be realized only when a few more conditions are fulfilled: a fast single spin detector and efficient bus lines for transporting electrons coherently. These requirements are beyond present day technology. Developing these techniques certainly represents one very important research direction for the quantum computing and spintronics community. On the other hand, as pointed out by Hu *et al.* [95], exploring new methods for studying entanglement in condensed matter systems is another interesting direction, especially in strongly correlated systems when

the generation of EPR pairs is very difficult. Nevertheless, an implementation of a shot noise detection experiment is an important step towards the demonstration of entanglement in such systems. In addition, this experiment is especially important for the study of quantum computing, since the coupled quantum dots system is essential for realizing the necessary gate operations for the quantum computing scheme based on electron spins and quantum dots.

### 3.2.3 Related theoretical work

A variety of theories have been developed to understand the electronic properties of a coupled quantum dot system [4, 5, 96, 97]. In general, this problem cannot be solved analytically, so calculations are all numerical. To proceed, a particular form for the confinement potential profile in the quantum dots is assumed, and the electron states in a single dot are calculated. Loss *et al.* [5] applied the Heitler-London method and the Hund-Mulliken approach to a coupled quantum dot system in GaAs/AlGaAs heterostructures. Both methods use electron wave functions of a single dot to construct molecular states for the coupled dots, taking into account the symmetry issues. The energy of these states is then evaluated. Although the two methods yield different results, they share some important qualitative features. It is predicted that at zero magnetic field the triplet states always have higher energy than the singlet state, as expected for a two particle system with time reversal symmetry. Both methods show a singlet-triplet crossing at some finite magnetic field. In both cases the energy difference between the singlet and triplet states, or

the exchange coupling strength  $J$ , decays exponentially as the intra-dot distance increases.

Recent work by Hu *et al.* [96] goes beyond the above two methods by using more single electron wave functions to construct molecular states. Their calculations have shown similar features. In addition, they studied the dependence of  $J$  on the height of the tunneling barrier between the two dots and found that  $J$  decays exponentially as the barrier height increases. Hu *et al.* also studied the more realistic case of multi-electron quantum dots. The original proposal assumed that each quantum dot has only one electron. However, for the quantum dots based on the gating technology in the 2DEG in GaAs/AlGaAs heterostructures, even with the most advanced fabrication process, it is still very difficult to make quantum dots containing only one electron. For quantum dots with multiple electrons, the electronic states usually have a shell structure similar to that of atoms. For example, in the case of an even number of electrons, they always pair up and form closed shells, while in the case of an odd number of electrons, one valence electron is left at the upmost state. In addition, in very small dots the energy difference between these shells is usually much larger than other relevant energy scales (e.g., the thermal energy, the Zeeman splitting, etc.). As a result, it is reasonable to expect that all the electrons in the closed shells have little effects on the dynamics of the valence electron, suggesting that two dots each having an odd number of electrons can be used to implement the proposed entanglement experiment. Indeed, Hu *et al.* showed theoretically [97] that quantum operations can still be performed with as many as

three electrons in each quantum dot.

## Chapter 4

### Fabrication and Instrumentation

In this chapter I discuss the sample fabrication and the instrumentation used for my experimental work. The first section explains the three level e-beam lithography technique I used for fabricating mesoscopic samples. Since my experiments require amplifiers with very low noise and relatively high frequency response, two cryogenic amplifiers were developed. They are discussed in detail in the second section. The third section describes the dilution refrigerator setup. Some critical noise reduction techniques are discussed in the last section.

#### 4.1 Sample fabrication

The starting material for my 2DEG samples is an MBE grown GaAs/AlGaAs heterostructure (see Fig. 2.1)<sup>1</sup>. At low temperatures, a 2DEG is formed about 50 nm below the surface. Compared to other similar structures, this is a shallow 2DEG. The dark mobility and carrier density of the 2DEG at 4.2 K are  $4 \times 10^5$  cm<sup>2</sup>/V·s and  $2 \times 10^{11}$  cm<sup>-2</sup> (This is the result from the wafer grower; my own characterization with a Hall bar geometry gave a similar result). Each time a 4 mm × 4 mm chip is cut from the wafer, and four samples can be made on this chip.

I used E-beam lithography techniques for fabricating all the samples used in

---

<sup>1</sup>The wafer was purchased from the Shayegan group at Princeton

the experiments reported in this thesis. This is the only reproducible way of fabricating the nano-scale high quality mesoscopic samples required for the entanglement experiment.

The fabrication process is composed of three main steps, as shown in Fig. 4.1(a): (1) forming Ohmic contacts to the 2DEG; (2) defining the active region by wet etching; and (3) depositing metallic gates. Each step includes e-beam lithography. An alternative to e-beam lithography for the first two steps, where there are no small features to be defined, consists of an optical lithography process. However, e-beam lithography is convenient for all steps since it allows me to make modifications to an existing design without going through the time consuming process of fabricating of optical masks.

The purpose of the first step is to make low resistance Ohmic contacts to the 2DEG so leads can be connected. The chip is first cleaned in hot acetone and hot IPA (Isopropanol Alcohol) (both at 80°C), each for 5 minutes. Sometimes I would spray the solution using with a syringe in order to remove dirt on the chip. In general, ultrasonic cleaning should not be applied to GaAs 2DEG heterostructures, since this may cause possible degradation of the electron mobility<sup>2</sup>. The chip is then coated with three layers of positive<sup>3</sup> e-beam resist [poly methyl methacrylate (PMMA)] (Fig. 4.1(b)). The first layer of PMMA has a molecular weight of 150,000. It is spun at 4000 rpm and then baked at 40°C for 1 minute, 80°C for 2 minutes,

---

<sup>2</sup>Ultrasound is expected to introduce defects or worsen existing ones in samples.

<sup>3</sup>A positive resist will be removed by a developer only if it is exposed to an e-beam while a negative one will be removed only if it is unexposed.

and 140°C for 30 minutes. The second layer of PMMA is processed in the same way except that the chip is baked at 140°C for 1 hour. The third layer of PMMA, with a molecular weight of 360,000, is spun at 6000 rpm and then baked at 40°C for 1 minute, 80°C for 2 minutes, and 140°C for 2 hours. The approximate thickness is 400 nm for the first two layers and 100 nm for the last layer. The baking for all three layers helps solidify the PMMA and thus avoid inter-layer mixing, which is very important for fabricating samples with small features.

I did e-beam lithography using a JEOL-420 Scanning Electron Microscope (SEM). Typical settings are an accelerating voltage of 30 kV, a working distance of 8 mm and a field scale of 1.5 mm. An e-beam current of about 6000 pA (and a dose of 10 pC/ $\mu\text{m}^2$ ) is used to expose the PMMA in the area where Ohmic contacts are to be made [Fig. 4.1(c)]. The chip is then developed in a solution of methyl isobutyl ketone (MIBK):IPA (1:3 by volume) at 23 °C for 30 seconds (Fig. 4.1 (d)), rinsed in IPA, and blown dry with research grade N<sub>2</sub>. An undercut profile is created in the resist due to the different sensitivity to the e-beam of the two types of PMMA and also due to the backscattering and secondary electrons, as shown in Fig. 4.1(d). After developing, the chip is immediately transferred into the vacuum chamber of an evaporator. The chamber is pumped down to  $1 \times 10^{-6}$  Torr by a cryo-pump. Metals are thermally evaporated in the following sequence: 5.0 nm Ni at 0.1 nm/sec, 100 nm AuGe alloy (Au:Ge = 85:15 by weight) at 0.15 nm/sec, 10 nm Ni at 0.1 nm/sec and 200 nm Au at 0.2 ~ 0.4 nm/sec (Fig. 4.1(e)). After waiting for about 20 minutes for the system to cool down, the chip is taken out of the chamber and immersed

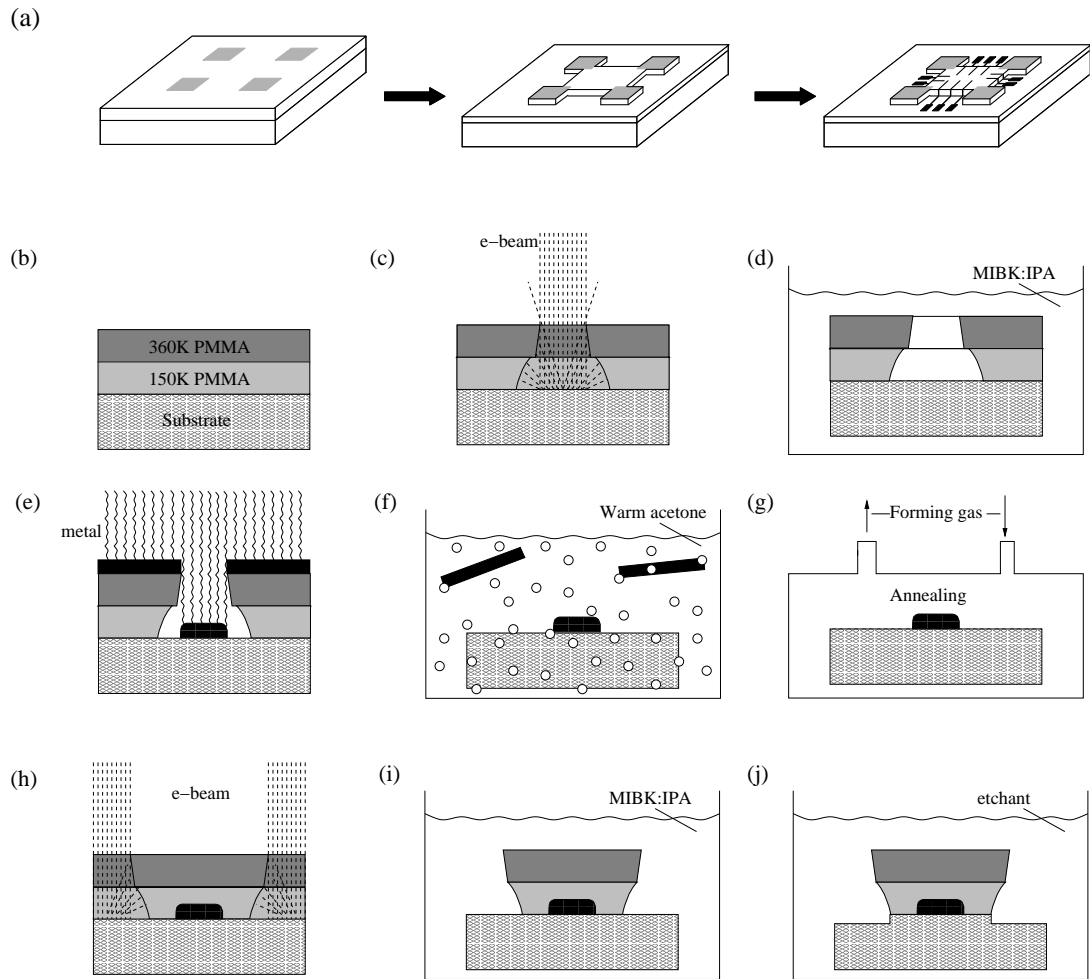


Figure 4.1: Sample fabrication. (a) The three level e-beam lithography: Ohmic contacts, etching and gate level; (b) PMMA configuration; (c) e-beam exposure; (d) developing; (e) thermal evaporation; (f) lift-off; (g) annealing; (h) e-beam exposure for etching level; (i) developing; (j) etching.

into acetone for a few minutes for lift-off (Fig. 4.1(f)), then rinsed in IPA and blown dry. The undercut profile in the resist is crucial for the lift-off step. Without such a profile, metal deposited on top of the resist could adhere to the metal deposited on the chip surface and the desired gate pattern would not be achieved. This is also true for the gate level process.

During the first level of lithography, a few small regions of PMMA are overexposed for the purpose of fine focus adjustment and alignment between different levels of lithography. Overexposed PMMA provides very good contrast with respect to unexposed PMMA and can be used to tune the focus and stigmatism precisely. In these focusing spots the PMMA molecular chains are cross-linked due to overexposure and cannot be removed by the developer. During the evaporation, metal is deposited on top of the cross-linked PMMA and can be used as an alignment mark for the second and third levels of lithography.

Annealing the chip at high temperatures is a very important step for creating Ohmic contacts [Fig. 4.1(g)]. It is a complex process sensitive to both temperature and annealing time. Different annealing parameters yield very different contact resistances, ranging from a few hundred  $\Omega$  to a few  $k\Omega$ . Over-annealing ( $> 10$  min) sometimes leads to a resistance of a few  $M\Omega$ . The smallest resistance ( $< 600 \Omega$ ) is achieved by using the following recipe:  $110^\circ\text{C}$  for 10 s,  $330^\circ\text{C}$  for 30 s, and  $430^\circ\text{C}$  for 1 min. The annealing is done in a forming gas (Nitrogen:Hydrogen = 87:13 by volume) atmosphere. After annealing, the chip is cleaned in hot acetone and hot IPA, each for 5 minutes.

The active region of a device includes the Ohmic contacts and the inner gate area where the mesoscopic samples are to be fabricated. For the entanglement experiment, these are two quantum dots and the beam splitter. The rest of the chip is etched to remove the 2DEG. Although the 2DEG is 50 nm below the surface, a shallow etch of 10 nm is enough to deplete the 2DEG due to a surface depletion. This not only defines the active area of the sample but also removes large areas of the 2DEG, reducing the gate to 2DEG leakage.

The e-beam lithography process for the etching level is very similar to that used for the Ohmic contacts, except that now only one layer of 150,000 PMMA is used for coating the chip. Focusing spots made in the first level of lithography are used as alignment marks to adjust the position of the chip. The PMMA outside of the active region is exposed and removed by the same developing procedure. The chip is then dipped into a solution of  $\text{H}_2\text{O}_2:\text{H}_2\text{SO}_4:\text{H}_2\text{O}$  (1:4:100 by volume) at  $22^\circ\text{C}$  for 1 minute. This solution etches GaAs at a rate of 0.5 nm/sec. However, the chip is usually covered with an oxidized layer, which takes about 20~30 s to remove, so the overall etching depth is about 15 ~ 20 nm. After etching, the chip is rinsed in deionized water and IPA and then blow dried.

Before the third level processing, the chip is cleaned again with hot acetone and hot IPA for 5 minutes each. A bilayer of PMMA is used for coating the chip for this stage. The first layer is 150,000 PMMA and the second layer is 300,000 PMMA, both spun at 8,000 rpm. The approximate thickness is 100 nm for the first layer and 60 nm for the second layer. The gate level process is similar to that for the Ohmic

level [Fig. 4.1(b) ~ (f)] except for some additional details described below.

The lithography for the gate level is done with a three field-scale self-alignment technique. In this technique, the coated chip is exposed to the e-beam sequentially at three different field scales:  $30\ \mu\text{m}$ ,  $100\ \mu\text{m}$ , and  $1.5\ \text{mm}$ . The first scale is for the finest features with a typical line width of  $30\ \text{nm}$ , including the two dots and the beam splitter [see Fig. 4.2(b)]; the  $1.5\ \text{mm}$  scale is for 16 bonding pads each with a size of  $150\ \mu\text{m} \times 150\ \mu\text{m}$ ; and the middle scale is for the leads connecting bonding pads and the inner small features (see Fig. 4.2(a)).

On my samples there are 12 gates altogether and they come very close to each other at the center of the device. Very fine focus and precise dose control are required to make narrow lines close to each other (separation  $< 30\ \text{nm}$ ) due to the proximity effect (the actual exposure area in PMMA is larger than the e-beam size due to the backscattering and secondary electrons). These fine features can only be made at small field scales. Self alignment means that after aligning the e-beam with the marker at the smallest field-scale, no further stage displacement is necessary to write the patterns at the three different field-scales, therefore a careful design should be made to join the features exposed at the three scales. Typical e-beam currents used for the three scales are:  $10\ \text{pA}$ ,  $20\ \text{pA}$ , and  $6000\ \text{pA}$ .

After lithography the chip is developed as before and immediately transferred into the vacuum chamber of an evaporator. At a base pressure below  $2 \times 10^{-6}\ \text{Torr}$ , 25 to  $30\ \text{nm}$  AuGe alloy (Au:Ge = 85:15 by weight) is thermally evaporated onto the chip at a rate of  $0.1\ \text{nm/sec}$ . To reduce the gate to 2DEG leakage, one can use

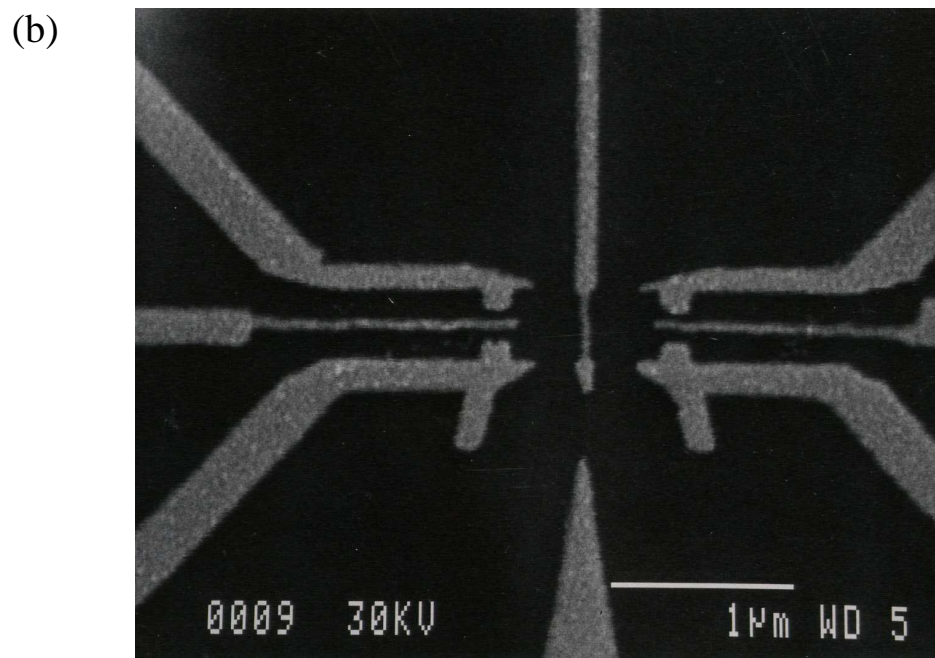
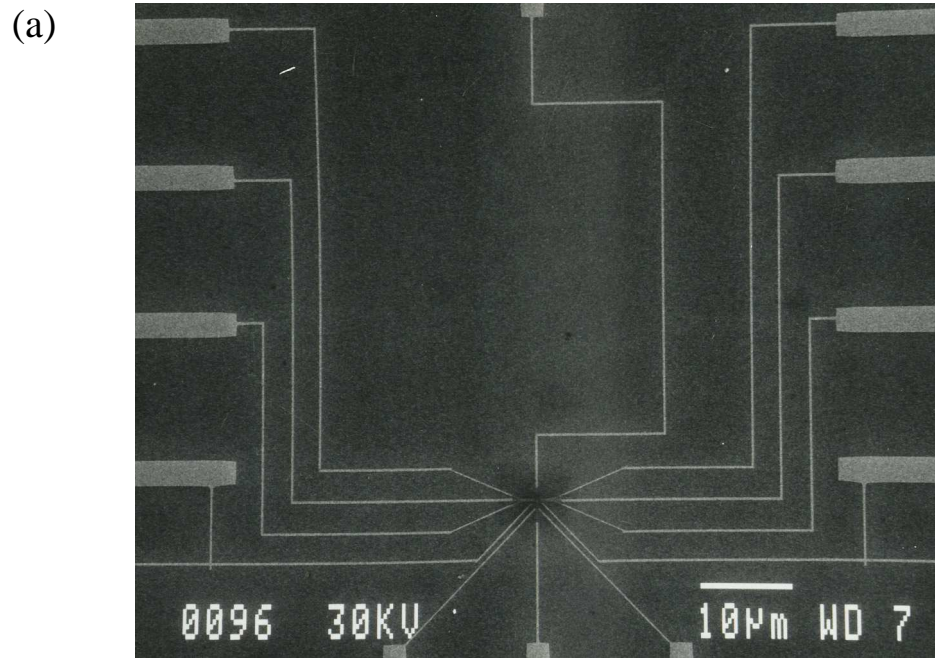


Figure 4.2: (a) SEM picture of the intermediate and inner gates (the bonding pads are not shown); (b) a sample used in the entanglement experiment.

the following recipe: deposit 1 nm Al and oxidize it with an oxygen pressure of 18 mTorr, and then repeating this a total of 5 times. AuGe alloy is then deposited on top of the  $\text{Al}_2\text{O}_3$  layer. The chip is then put into acetone for lift-off, rinsed in IPA and blown dry. The chip is glued onto a 16-pin sample header with silver paint for wire bonding. Aluminum wires are connected to the 16 leads (4 Ohmic contacts and 12 gates) using a Kulik and Soffa wire bonder. Before cooling, the resistance between the leads is measured to check for shorted and disconnected bonds.

Mesoscopic samples are delicate devices that have to be handled very carefully. In particular for GaAs/AlGaAs heterostructure 2DEGs, special care should be taken during fabrication to maintain the sample quality, i.e. the electron mobility. As mentioned early, ultrasonic power should not be used for either cleaning or lift-off to avoid possible 2DEG degradation and the possibility of ripping off very fine gate structures. Mesoscopic samples can also be very sensitive to electrostatic discharge, so all sample fabrication processes should be done in an environment with humidity control. The experimenter should ground himself properly when wire bonding and checking resistance. In general, the active region where fine gate structures are made should not be exposed to a high dose e-beam, because this can degrade the electron mobility in the 2DEG. The mechanism of this degradation is not very well understood. A possible explanation is that a high dose e-beam can cause surface contamination on the chip which partially depletes the 2DEG even at zero gate voltages.

## 4.2 Cryogenic amplifiers

I used two cryogenic amplifiers for the experimental work reported in this thesis. In this section I discuss their purpose, design, construction, and calibration.

For all types of measurements the signal to noise ratio (SNR) is an important quantity. In most transport measurements “signal” refers to some electrical quantity such as current or voltage at a fixed frequency or within a specific frequency span, while noise refers to all sorts of unwanted fluctuations including thermal noise, low frequency noise, and external interference. Many techniques have been developed to filter noise out of the frequency range of interest, so that high SNR can be achieved. A classical example is the lock-in technique in which phase sensitive detection is used to extract the signal. For shot noise detection, however, the “signal” now refers to the shot noise generated in the device under test. Since the shot noise is expected to have an almost flat power spectrum over the accessible measurement range, the “signal” is distributed over a very broad band. Therefore for my experiment the SNR is defined as the shot noise in a frequency span over the total noise in the same span. Many traditional noise reduction techniques will not work in such a situation. As a simple example, consider an ac current signal of 1 nA measured with a 1 Hz bandwidth and a shot noise signal with a RMS value of 1 nA measured with a bandwidth of 1 MHz. For a background thermal noise with a power density of  $10^{-22}$  A<sup>2</sup>/Hz, the SNR for shot noise detection is only 1%  $((1 \text{ nA})^2 / (10^{-22} \text{ A}^2/\text{Hz} \times 1 \text{ MHz}) = 0.01)$ . On the other hand, for the 1 nA ac current the total measured power is also  $10^{-18}$  A<sup>2</sup>, but the detected thermal noise power is only  $10^{-22}$  A<sup>2</sup> in a

1 Hz detection bandwidth, therefore the SNR is 10,000. This difference makes shot noise detection much more difficult, which is why a low noise broad band amplifier is required.

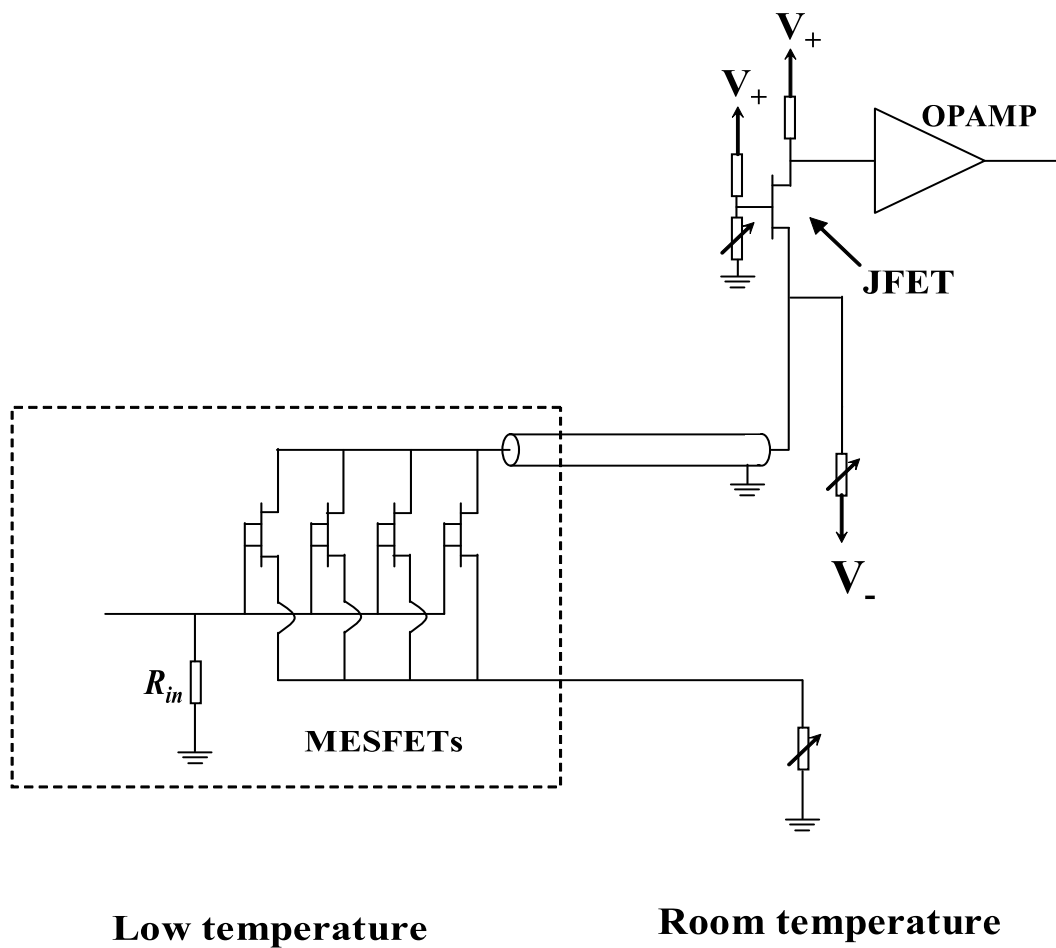
To determine the frequency range for shot noise detection, a few things must be taken into account. Both amplifiers and devices under test exhibit low frequency noise, such as  $1/f$  noise and random telegraph noise. In general, the magnitude of this noise depends on temperature, applied current, and frequency. In most cases, we found the frequency range below 100 kHz was not suitable for our experiment due to high excess noise levels. On the other hand, working at very high frequencies ( $\sim$  GHz) requires special wiring in the dilution refrigerator. In addition, most broadband amplifiers require the use of  $50 \Omega$  matching exclusively, which is not easy to achieve in our system. As a result, the ideal frequency range is from a few hundred kHz to a few MHz. In this range most commercial amplifiers do not have the performance required for our measurements; these amplifiers usually contribute too much background noise. Most of the amplifier noise comes from the thermal noise of the components of which the amplifiers are made, so the natural solution is a cryogenic amplifier.

Operating amplifiers at cryogenic temperatures has the following advantages. First, low temperatures tend to lower the noise contributed by the amplifiers themselves. Second, using a cryogenic amplifier minimizes stray capacitance of long wiring. In order to build these amplifiers, one has to carefully select the constituent components. They should function properly at low temperatures and dissipate little

power to avoid substantially heating the sample and the dilution refrigerator.

The amplifiers used in our experiment are based on a design by the Cabrera group at Stanford [98]. These amplifiers use a two stage cascode configuration as shown in Fig. 4.3. The cryogenic stage is four MESFETs (Metal-Semiconductor-Field-Effect Transistor) operating in parallel. This stage can be viewed as a transconductance amplifier in the sense that it converts the voltage signal present at the input to a current signal in the channels of the MESFETs. The current signal is then transmitted to the source of a JFET (Junction-Field-Effect-Transistor) through a coax cable. The JFET behaves like a transimpedance amplifier converting the current signal back to a voltage signal, which is further amplified by the operational amplifiers.

Specific design details can be found in the reference given above. Here I only discuss the essential features of the design. To achieve a superior performance, these cryogenic amplifiers should be as cold as possible and should be brought very close to the devices under test. In our dilution refrigerator, the ideal place for them is about 1 to 2 feet above the sample cell (see section 4.3 for details), where the ambient temperature is around 4 K. At this temperature, silicon based transistors suffer the carrier “freeze out” problem. Germanium devices can operate at this temperature but are not commercially available. The only choice left is GaAs based transistors, either MESFETs or HEMTs (High Electron Mobility Transistors). The MESFETs I used are GaAs N-channel dual gate MESFETs manufactured by SONY (model 3SK164). The JFET I used is silicon N-channel JFET manufactured by SONY



**Low temperature**

**Room temperature**

Figure 4.3: Schematic of the cryogenic amplifier.

(model 2SK152).

There are three benefits of using a cascode configuration [98]. First, for the cryogenic stage, the low source impedance of the JFET, typically  $100\ \Omega$ , is easy to drive. From the circuitry point of view, this gives a small RC time constant and thus a relatively large bandwidth (for a typical  $C = 300\ \text{pF}$ , the bandwidth is about 5 MHz). Second, this source impedance is a reasonable match to the coax cable at this frequency range, so a good high frequency response can be obtained. Finally, the Miller effect is reduced in such a configuration. The Miller effect refers to the effective increase of the input capacitance due to the gate-drain capacitive coupling and a high voltage gain. This effect can decrease the bandwidth and cause instabilities due to positive feedback. In a cascode configuration, this effect can be avoided because of the low voltage gain of the first stage.

Figure 4.4(a) shows a noise model of a MESFET [99]. The noise in a MESFET can be characterized by two noise current sources,  $i_g$  and  $i_d$ . Another more commonly used model is shown in Fig. 4.4(b), where the  $i_d$  in (a) is represented as a noise voltage source  $e_n$  at the input. These two models are related by the following equations:  $i_n = i_g$ ,  $e_n = i_d/g_m$ , with  $g_m$  being the transconductance of the MESFET. The model in (b) is useful because any signal at the gate can be compared to  $i_n$  and  $e_n$  directly. However, the model in (a) is more fundamental.

In the model shown in Fig. 4.4(b), the two noise generators can be expressed as [98]:

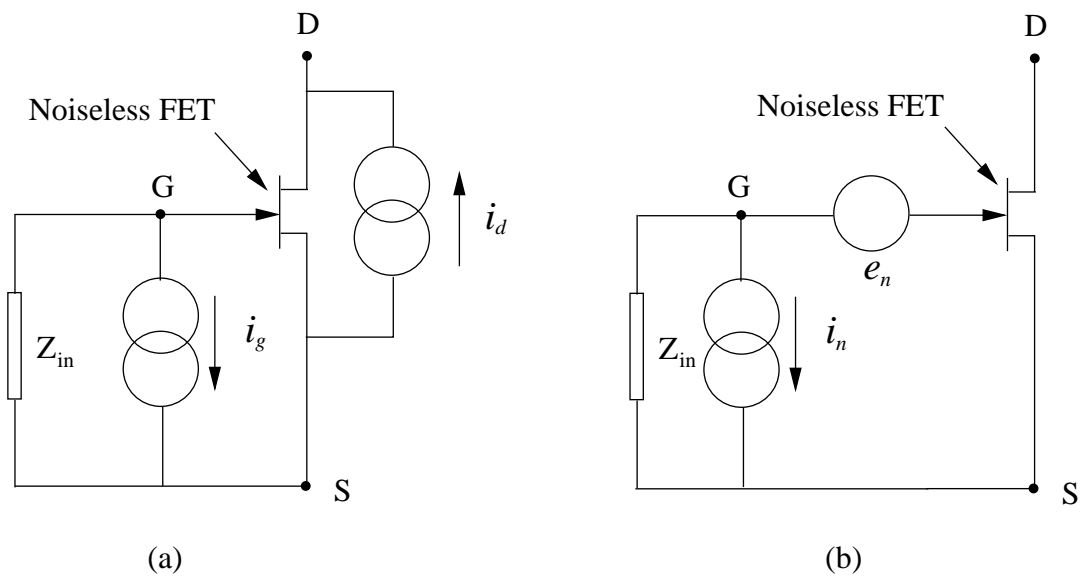


Figure 4.4: FET noise models. (a) the drain-current-noise model including two current-noise generators:  $i_g$  and  $i_d$ ; (b) the gate-voltage-noise model, in which the  $i_d$  in (a) is replaced by an equivalent voltage noise generator at the gate.

$$\begin{aligned}
i_n^2 &= 2eI_g + \frac{4k_B T}{g_m} \frac{4\omega^2 C_{gs}^2}{15} \\
e_n^2 &= \frac{4k_B T \alpha}{g_m}.
\end{aligned} \tag{4.1}$$

where  $I_g$  is the gate leakage current,  $T$  is the channel temperature,  $g_m$  is the transconductance,  $C_{gs}$  is the gate-source capacitance, and  $\alpha$  is a constant of the order of 1. There are two contributions to  $i_n^2$ : one is the shot noise of the gate leakage current; the other one is the thermal noise of the channel. Operating MESFETs at cryogenic temperatures highly reduces the gate leakage current. As a result, the first term in  $i_n^2$  is usually a few orders magnitude less than the second term [98]. Therefore the optimum matching impedance can be found as:

$$Z_{opt}^2 = e_n^2 / i_n^2 = \frac{15\alpha}{4\omega^2 C_{gs}^2}, \tag{4.2}$$

For a typical  $C_{gs}$  value of 1 pF,  $Z_{opt} \approx 1 \text{ M}\Omega$  for a frequency of 200 kHz<sup>4</sup>, and is much higher than the source impedance (typically around 10 k $\Omega$ ) in all my measurements. In such a case, the contribution of the  $i_n^2$  to the total amplifier noise is much less than that of the  $e_n^2$  term, and this was experimentally verified for my amplifiers. In the following, the  $i_n^2$  term will be neglected.

Operating MESFETs in parallel reduces the background voltage noise contribution from the amplifiers. According to the model in Fig. 4.4(b), the total  $i_d$  of  $N$  MESFETs operating in parallel is:

---

<sup>4</sup>My experimental data in Chapters 5 and 6 was taken around this frequency.

$$i_{dN}^2 = Ni_d^2 \quad (4.3)$$

The noise power from different devices should be added since their noise sources are expected to be uncorrelated. From equation 4.3 one has  $i_{dN} = \sqrt{N}i_d$ . On the other hand, the transconductance of  $N$  MESFETs in parallel is  $Ng_m$ , so  $e_{nN} = \sqrt{N}i_d/(Ng_m) = e_n/\sqrt{N}$ . As a result of operating  $N$  devices in parallel, the noise voltage source  $e_{nN}$  decreases by a factor of  $\sqrt{N}$ . However, the power dissipated by  $N$  devices is also  $N$  times as that dissipated by one device, which can heat up the sample and dilution refrigerator significantly. A reasonable compromise is obtained by using 4 MESFETs in parallel (8 for the two cryogenic amplifiers) which results in the temperature of the sample cell increasing from 50 mK to 70 mK. The pressure in the still line of the refrigerator increases correspondingly, approaching the operation limit.

In general when these amplifiers are cooled to below liquid helium temperature, the bias conditions have to be readjusted in order to achieve the best performance. Figure 4.5 shows results for one amplifier at 4.2 K (the other is very similar). I found a constant voltage gain from about 10 kHz to 1 MHz. For the equivalent input voltage noise, it is clear that low frequency noise dominates below 200 kHz, while at higher frequencies a white thermal noise background with a magnitude of  $0.8 \text{ nV}/(\text{Hz})^{1/2}$  appears.

The FET noise model shown in Fig. 4.4(b) can be generalized to describe any amplifier. For an amplifier with an equivalent input voltage noise  $e_n^2$  and an

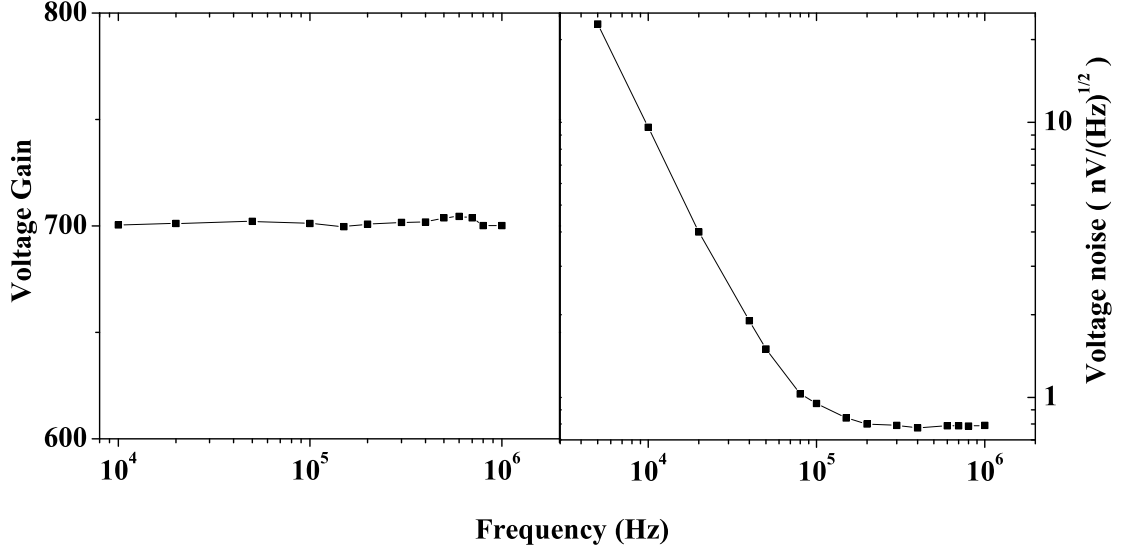


Figure 4.5: Calibration of the cryogenic amplifier at 4.2 K. (a) voltage gain; (b) equivalent input voltage noise  $e_n$ .

equivalent input current noise  $i_n^2$ , the total background noise contributed by the amplifier is  $e_n^2 + i_n^2 Z_{in}^2$ , where  $Z_{in}$  is the input impedance of the amplifier. If the shot noise to be detected has a power density  $i_s^2$ , the signal to noise ratio will be  $S/N = i_s^2 Z_{in}^2 / (e_n^2 + i_n^2 Z_{in}^2)$ . Amplifiers with both a small  $e_n^2$  and a small  $i_n^2$  are required to detect the shot noise of a very small current. Commercial amplifiers can be roughly categorized into two groups: current amplifiers and voltage amplifiers. They are designed to have very low voltage noise or current noise but usually not both. The unique feature of the cryogenic amplifiers discussed in this section is the combination of a small  $e_n^2$ , a small  $i_n^2$ , and a good frequency response. Such a combination is crucial for the low noise measurements reported in this thesis. With the cross correlation technique that I will discuss in section 4.4, the sensitivity of

our amplifiers is one order of magnitude higher than what was achieved in similar works using a much more complicated setup.

### 4.3 Dilution refrigerator wiring

The experimental shot noise data in this thesis was taken at low temperatures. The cooling system consists of a “home-built” dilution refrigerator (see Fig. 4.6).

The dilution refrigerator consists of two parts: a helium gas circulation system and a top-loading probe (see grey area in Fig. 4.6). The low temperature part of the refrigerator is enclosed in a vacuum can immersed in a liquid helium bath. Its inner shell is a tubing for the top-loading probe, which can be removed from and inserted into the tubing for sample exchange without warming up the whole system. The space between the outer shell and inner shell of the helium circulation system serves as a still line. Cold  $^3\text{He}$  vapor from the mixing chamber is pumped out through the still line and cools the gas returned via the condensing line. At the bottom of the tubing for the top-loading probe there is a thin metallic foil separating the sample cell and the mixing chamber. In operation, pure  $^3\text{He}$  is liquified in the tubing and makes good thermal contact with the solution in the mixing chamber via the thin foil. When the top-loading probe is completely inserted, the sample is thus immersed directly in liquid  $^3\text{He}$  and can be cooled down to 70 mK. The main part of the top-loading probe is a rigid supporting structure made of nonmagnetic stainless steel tubing. The bottom part of the probe (below the cryogenic amplifier) is a plastic rod that provides good thermal isolation. The part between the stainless steel and

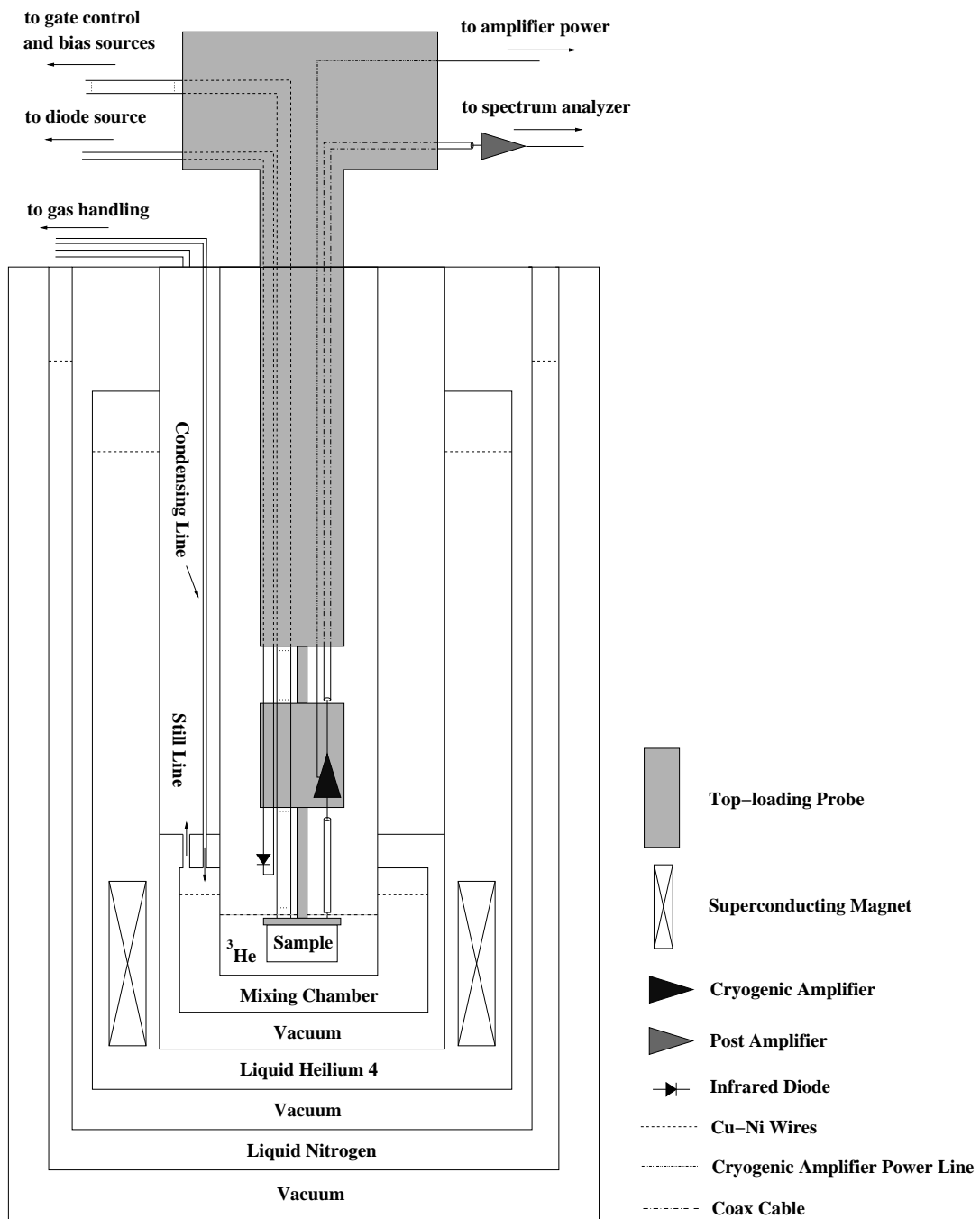


Figure 4.6: Dilution refrigerator wiring schematic.

the plastic rod is a brass plate where the two cryogenic amplifiers are mounted. The plate is thermally grounded through the tubing for the top-loading probe. A 16 Tesla superconducting magnet sits at the bottom of the helium bath.

Five groups of wires are used. The first group, not shown in the figure, is for thermometry. A ruthenium dioxide resistor located right beside the sample holder (about 5 mm away horizontally from the sample) is used as a thermometer by monitoring its resistance in a four terminal configuration. The second group is a pair of wires for an infrared diode used to excite electrons in the sample. The diode is located about 2 inches above the sample and controlled by a Keithley current source. The third group is a set of wires for gate control and sample biasing. A typical sample has 4 Ohmic leads and 12 gates, so the minimum number of wires for this group is 16. I chose Cu-Ni wires for their low thermal conductivity and low thermoelectric coefficient (which means low thermal emf). Using wires with very low thermal emf is crucial for implementing low level signal cryogenic experiments to avoid unaccounted for dc biases. The fourth group of wires is a set of power lines for the two cryogenic amplifiers, and the last group is a pair of coax cables that transmit the shot noise signal from the cryogenic amplifiers to the post amplifiers at room temperature. The coax cables connecting the sample to the cryogenic amplifiers have both the inner and outer conductors made from nonmagnetic stainless steel. They are chosen for their low thermal conductivity. To avoid coupling between the different groups and also for convenience, a few Cu-Ni shielded tubes enclose the different groups of wires in the probe.

Due to the limited space (the diameter of the top-loading probe is about  $\frac{3}{4}$ "), installing five groups of wires and two cryogenic amplifiers is a challenge. One has to be very careful, since any modification may damage nearby parts. Also, frequent removal and insertion of the top-loading probe can damage the wires and other parts. Before every cool down, a routine check should be performed on the diode, the amplifiers, the thermometer, and all the electrical leads for the sample. Another major problem caused by the limited space is the grounding for the cryogenic amplifiers. In principle, the ground of these amplifiers should be isolated from the metal supporting structure of the dilution refrigerator. However, in our system it is extremely difficult to make a full isolation. This causes some noise problems, that can, however, be improved as discussed in the next section.

#### 4.4 Noise reduction

For the experimental work in this thesis, the shot noise of very small currents ( $\sim 100$  pA) is to be detected. To have an idea of the order of magnitude of the signal, consider for example that the full shot noise power spectrum density of 100 pA, which is  $3.2 \times 10^{-29}$  A<sup>2</sup>/Hz. The RMS value of this noise in a frequency span of 1 MHz is only 5.7 pA. In order to detect such a small signal, the experiment has to be designed very carefully. The main effort was to develop low noise broadband amplifiers, as discussed in section 4.2. In this section, I discuss some additional noise reduction techniques I used.

All the wires in the top-loading probe are well shielded. As mentioned above,

the wires are grouped and placed in different Cu-Ni tubes and these tubes are further shielded by the main support tube of the top-loading probe. The head of the probe is an aluminum box with BNC connectors. Two feed-through SMA connectors are used for the outputs of the cryogenic amplifiers.

For most cases, gates are controlled by batteries. When a variable gate voltage source is needed, a home-made  $RC$  low pass filter is used to filter out the high frequency noise generated by the instrument. Other instruments are powered by batteries whenever possible. The cryogenic amplifiers are powered by Scorpion  $\pm$  15 Volts dc voltage sources with low pass filters. All instruments to be added to the measurement system are checked before any real data acquisition to avoid introducing extra noise.

The head of the top-loading probe is grounded with a 3 cm wide grounding braid. The outputs of the post amplifiers are fed into differential amplifiers with both inputs isolated from the chassis ground, so ground loops can be avoided. This is a crucial arrangement for achieving low noise circuitry. Since the outer shell of the input BNC connectors of the spectrum analyzer is also its chassis ground, connecting the post amplifiers directly to the spectrum analyzer would produce ground loops. The gate control battery box is floating at all time, while the Scorpion voltage sources for the cryogenic amplifiers have their own neutral terminals and are isolated from the ac power ground.

The most serious problems associated with grounding in this system have two sources. One source of problem is interference from noisy apparatus sharing the

same ground, such as the circulation pump in the gas handling system. In principle, these noisy parts should be grounded separately. Since the dilution refrigerator was not built specifically for a shot noise measurement, the grounding is not ideal. However, this can be much improved by carefully choosing the main grounding point (where the grounding braid is connected). Another source of problem is from ground loops formed when electrical instruments are added to the measurement system. Usually, these instruments are not battery powered and do not have differential inputs isolated from the normal ac power ground. As a result, we have multiple grounding in the measurement system. This situation is avoided whenever possible; otherwise, a comparison between the noise before and after the instrument is added should be done to assure that no significant increase in noise occurs.

Given the complexity of the measurement system, it is hard to find a routine way to achieve good grounding. Often a working configuration can become noisy when some changes are made to the system. The general rule is to always monitor the output of the spectrum analyzer to find the best configuration.

With all the techniques used above, one can get rid of most external interference coupled to the system by means of radiation, conducting channels and grounding loops, etc. However, the intrinsic noise sources, such as the thermal noise from the sample and the cryogenic amplifiers, are always present together with the shot noise signal. In the following, I discuss how spectrum analysis can be used to solve this problem.

Due to the broadband nature of shot noise, a spectrum analyzer is a proper

instrument to do the measurement. I used an Agilent 89410A spectrum analyzer for all the noise detection. This is a dual-channel broadband (dc to 10 MHz) digital spectrum analyzer using a fast Fourier transform (FFT) technique. It can be used to measure the Fourier spectrum of a signal, its noise power, and the cross spectrum of two signals, among many other quantities.

An FFT spectrum analyzer samples a signal presented at its input at a certain frequency (25 MHz for the Agilent 89410A) and then digitizes the samples. The outcome is a sequence of digitized voltages in the time domain. An FFT is then performed on the sequence to calculate the spectrum in the frequency domain. These spectrums can be further used for calculating more complex functions, such as the cross spectrum. Due to the limited number of time domain samples, the resulting spectrum has large fluctuations from point to point even for a white noise signal. Usually many averages are required to achieve a stable and uniform spectrum.

For shot noise detection, the total signal  $V(t)$  detected by the analyzer includes the shot noise  $V_1(t)$ , the thermal noise from the sample  $V_2(t)$ , and the noise from the amplifier  $V_3(t)$ . The Fourier spectrum of  $V(t)$  is:

$$V(\omega) = V_1(\omega) + V_2(\omega) + V_3(\omega), \quad (4.4)$$

where  $V_i(\omega)$  are Fourier spectrums of the three voltages. The total noise power is then

$$P = V(\omega)V^*(\omega) = V_1(\omega)V_1^*(\omega) + V_2(\omega)V_2^*(\omega) + V_3(\omega)V_3^*(\omega), \quad (4.5)$$

where I assume there is no correlation between any of the noise sources. Typically the shot noise power is only 10% of the thermal noise power of the sample and 1% of the amplifier noise. To increase the signal to noise ratio, a cross correlation technique is used. The basic idea is using two independent amplifiers to measure the voltage across the device under test, which is  $V_1(t)+V_2(t)$ . The outcomes of the two amplifiers are then fed into two independent channels ( $A$  and  $B$ ) of the spectrum analyzer. Now the spectrums coming out of the two channels are:

$$\begin{aligned} V_A(\omega) &= V_{1A}(\omega) + V_{2A}(\omega) + V_{3A}(\omega) \\ V_B(\omega) &= V_{1B}(\omega) + V_{2B}(\omega) + V_{3B}(\omega). \end{aligned} \quad (4.6)$$

Instead of measuring the noise power in each channel, we measure the cross spectrum of both channels, which is defined as

$$\begin{aligned} X(\omega) &= V_A(\omega)V_B^*(\omega) \\ &= V_{1A}(\omega)V_{1B}^*(\omega) + V_{2A}(\omega)V_{2B}^*(\omega) + V_{3A}(\omega)V_{3B}^*(\omega), \end{aligned} \quad (4.7)$$

where  $*$  means complex conjugation. Since  $V_{3A}(\omega)$  and  $V_{3B}(\omega)$  are the spectrum of the noise from two independent amplifiers, there should be no correlation between them. However, this is only statistically true, in other words, the average value of  $V_{3A}(\omega)V_{3B}^*(\omega) = 0$ . By averaging many times, one has

$$\langle X(\omega) \rangle = \langle V_1(\omega)V_1^*(\omega) \rangle + \langle V_2(\omega)V_2^*(\omega) \rangle, \quad (4.8)$$

where I assume the two amplifiers are identical so  $V_{iA}(\omega) = V_{iB}(\omega) = V_i(\omega)$  ( $i = 1,2$ ). Equation 4.8 basically says that by measuring the cross spectrum one can get rid of the noise contribution from the amplifiers. Practically there is always some residual correlation between the amplifiers, so  $\langle V_{3A}(\omega)V_{3B}^*(\omega) \rangle$  is never zero, but it is negligible in most cases.

## Chapter 5

### Shot noise of mesoscopic tunnel barriers

In this chapter I discuss shot noise measured I made in mesoscopic tunnel barriers fabricated in GaAs/AlGaAs heterostructures [100]. There are two main motivations for making these measurements. First, mesoscopic tunnel barriers have been well studied in the context of standard transport properties. However, as pointed out in Chapter 2, a lot of useful information about the transport processes is contained in the temporal correlation in the current, which is not accessible by standard transport measurements but is readily probed by shot noise detection. Therefore the study of shot noise will enrich our understanding of these systems. Second, tunnel barriers are one of the basic building blocks for more complicated mesoscopic structures and a thorough understanding of their noise properties will be helpful for the study of other mesoscopic structures. One example is the coupled quantum dot system proposed for quantum entanglement in Chapter 3, where a shot noise measurement is suggested for demonstrating electron spin entanglement. Thus knowledge of the shot noise properties of all components of such a system are crucial for implementing the entanglement experiment.

## 5.1 Overview

In 1918 Schottky first predicted [77] that a vacuum tube has two intrinsic sources of time-dependent current fluctuations: thermal noise and shot noise. Thermal noise is due to the thermal agitation of electrons. It is universal in all dissipative electrical conductors at finite temperatures and is well characterized by the Johnson-Niquist theorem. Shot noise is caused by the discrete nature of electron charge. In a vacuum tube, the cathode emits electrons randomly and independently. Such a Poisson process leads to a shot noise of  $2eI$  or full shot noise. This result can be generalized to other electrical transport processes that have Poisson statistics [99]. For example, full shot noise was experimentally observed in semiconductor diodes, bipolar transistors, and field effect transistors. In all of these systems, electrons encounter tunnel barriers. It is the random and independent scattering of electrons occurring at the barriers that generates the shot noise. However, these systems generally cannot be considered as mesoscopic conductors.

Recently shot noise in smaller tunnel barriers has been studied by different groups. Theoretical results are discussed in Chapter 2. For example, Birk *et al.* [101] measured the shot noise of a tunnel junction formed by an STM tip and a metallic surface. In their experiment the distance between the tip and the surface was kept constant, and the potential difference between them was varied. The tunnelling current and the shot noise were measured simultaneously as a function of the potential difference. Their result is in very good agreement with theory, especially the crossover between thermal noise and shot noise. Cron *et al.* [102] per-

formed similar shot noise measurements in aluminum atomic contacts (fabricated by a break-junction technique) in both the normal and the superconducting regime. Again, they found good agreement between theory and experiment. I want to point out that these measurements were all done in metallic conductors with tunnel barriers. Since the transport in these systems occurs at the atomic size level, these tunnel barriers are considered to be microscopic. In general, they suffer less from impurity problems than barriers fabricated in semiconductor systems. Indeed, shot noise has been used as a tool to obtain information about the conduction details in gold atomic contacts [103].

Another often studied system is the tunnel barrier formed in the 2DEG in GaAs/AlGaAs heterostructures by means of the split-gate technique discussed in Chapter 2. The fabrication details were summarized in Chapter 4. One main advantage of this type of barrier is that its transmission properties can be easily tuned by changing the voltages on the gates forming the barriers. For a single device, one can study both highly resistive tunnel barriers and quantum point contacts (QPCs). As explained in Chapter 2, open quantum channels in QPCs suppress the shot noise due to the Pauli principle. The first experiment was carried out by Li *et al.* [104] in 1990. They observed shot noise suppression below the Poissonian value, although the measurement was done at low frequency ( $f < 100$  kHz) where  $1/f$  noise and random telegraph noise dominate, and the measured shot noise did not have the expected linear dependence on dc current. Reznikov *et al.* [81] measured the shot noise of a QPC from 8-18 GHz by using cryogenic microwave amplifiers.

With a constant bias current, shot noise was measured as a function of the gate voltages. Minima of the shot noise were observed whenever the point contact had a conductance of an integer times  $G_0=2e^2/h$ , indicating that shot noise was suppressed by open quantum channels. However, the data was only in qualitative agreement with theory. With a noise correlation technique, Kumar *et al.* [82] were able to measure the shot noise of a QPC in the sub-nA regime at very low frequencies (a few kHz). The  $1/f$  noise from the sample could be ignored at the low currents used, while the correlation technique helped remove the low frequency noise from the amplifiers. They studied a point contact in the pinch-off regime with different transmission coefficients and found quantitative agreement between their results and theory.

The experiments just discussed focused on the shot noise suppression issue for QPCs where the barrier has either multiple fully conducting channels or/and one partially conducting channel with  $T \sim 1$ . At the other extreme where  $T \ll 1$ , only full shot noise was expected. More recently Safonov *et al.* [105] reported a measurement of shot noise in a tunnel barrier in an n-GaAs MESFET. Surprisingly they observed enhanced shot noise in the pinch off regime ( $T \sim 1$ ). Meanwhile, they identified resonant tunneling processes in their samples. They explained the enhancement by a model of interacting resonant tunneling states. To our knowledge, this is the first experimental work explicitly showing that the microscopic details, such as potential disorder and impurity configuration, can alter a barrier's shot noise significantly. Unfortunately, they could only do the noise measurement at relatively

high temperature ( $T > 1.5$  K), thus only a Fano factor of 1.5 was observed.

## 5.2 Experimental data

In this section I present the experimental data taken on our tunnel barrier samples fabricated in GaAs/AlGaAs heterostructures. For sample fabrication and measurement system details I refer the reader to Chapter 4.

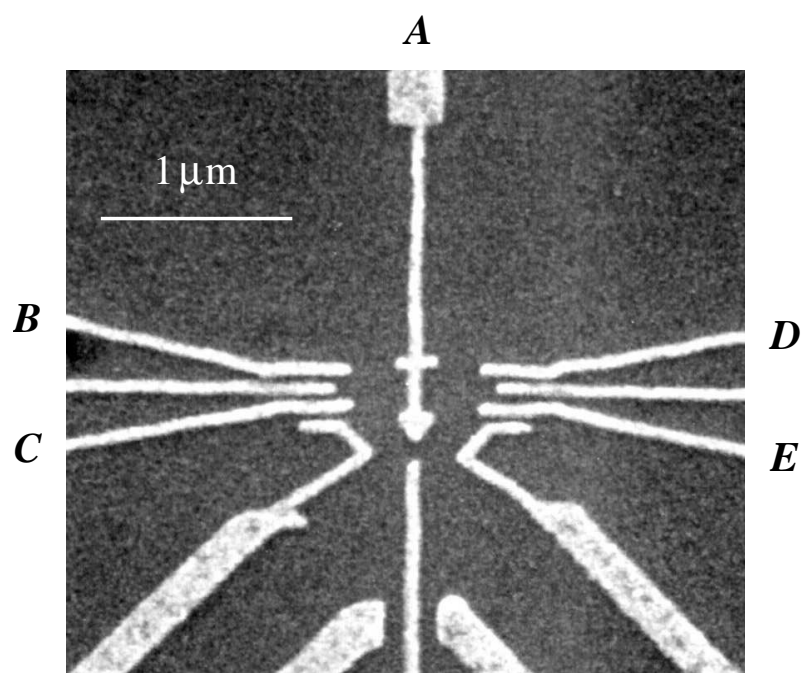


Figure 5.1: SEM picture of a sample I used to measure shot noise in tunnel barriers.

Gate *A* in combination with one of *B*, *C*, *D* and *E* form a tunnel barrier.

Figure 5.1 shows a SEM picture of a typical sample used for the experiments. These samples were designed for the entanglement experiment discussed in Chapter 6. On each sample two quantum dots are fabricated. For the measurements in this

chapter, only gates A, B, C, D, and E are used, while all other gates are grounded. Gate A in combination with any of B, C, D, and E form a tunnel barrier when negative voltages are applied, so on each sample four tunnel barriers can be tested. The data presented in this chapter are from 4 different samples with very similar design. In the following I will denote gate A as gate 1 and any of B, C, D, and E as gate 2.

According to the theory discussed in Chapter 2, a very resistive ( $G \ll e^2/h$ , or  $T_j \ll 1$ ) tunnel barrier at temperature  $T$  should have a total noise power

$$S_I(f) = \frac{e^3 V T_j}{\pi \hbar} \coth\left(\frac{eV}{2k_B T}\right) = 2eI \coth\left(\frac{eV}{2k_B T}\right), \quad (5.1)$$

where  $\omega$  is the frequency and  $I$  and  $V$  are the time averaged current and bias. For all the measurements in this chapter,  $T=70$  mK, corresponding to  $6 \mu\text{eV}$ , and  $V$  used is between  $40 \mu\text{V}$  and  $25 \text{mV}$ , so  $k_B T \ll eV$  is satisfied at all times. Under this condition equation (5.1) reduces to the classical Poissonian value  $2eI$ , so full shot noise is expected for a resistive tunnel barrier at low temperatures.

Figure 5.2 shows the noise measured in four different barriers. This measurement detects the noise as a function of the applied dc current by measuring the voltage across a bias resistor in series with the barrier. Power spectrum of noise was measured in a 20 kHz window centered at 220 kHz and then integrated over the frequency span to find the average value. The value at zero dc current (including the thermal noise from the sample and the noise contributed by amplifiers) was taken as a background and subtracted from all data points. Different current levels that

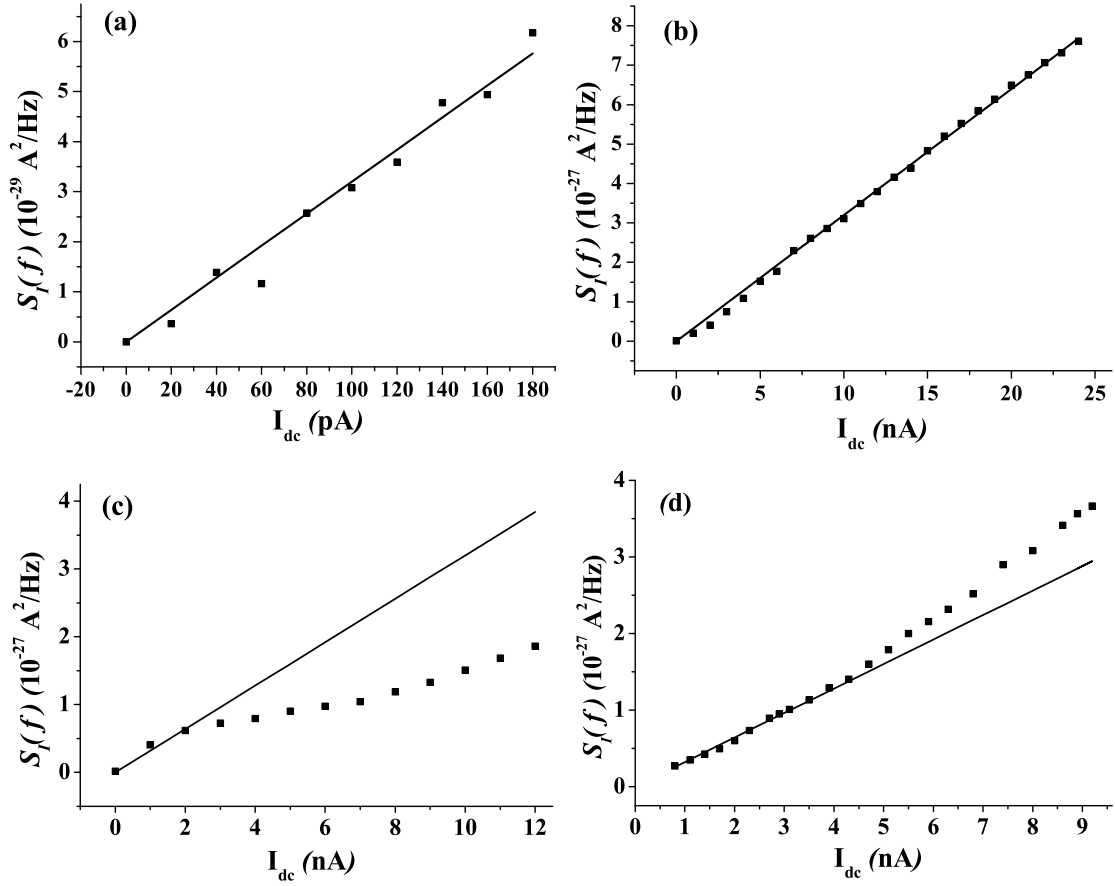


Figure 5.2: Noise power  $S_I(f)$  of tunnel barriers as a function of dc current. Solid line represent full shot noise with the Fano factor  $F = 1$  (see Chapter 2 for the definition of  $F$ ). (a),(b) full shot noise at low and high currents; (c) suppressed shot noise; (d) enhanced shot noise.

ranged from a few tens of pA to a few tens of nA were used. All barriers had a conductance of around  $0.01 e^2/h$  and changed by less than 5% over the whole measurement range. For reference, the theoretical prediction  $2eI$  is also plotted with solid lines. Some barriers exhibited a noise that was linearly dependent on the dc current and in excellent agreement with the full shot noise result (see Fig. 5.2 (a) and (b)). The theoretical value  $2eI$  fits the data reasonably well, so for these barriers  $F = 1$ . However, on other barriers, I observed both suppressed and enhanced shot noise, as shown in (c) and (d). In these cases, the measured shot noise does not have a simple dependence on the dc current.

All results were reproducible when the gate voltages were turned off and back on, as long as the sample was kept at low temperatures. After a thermal cycle to room temperature and back to low temperature, barriers showing full shot noise usually do not change, while barriers showing deviations still showed deviations but often of a different magnitude. Unknown problems in the measurement system would have caused systematic errors in noise detection. For example, passing large currents through the sample may introduce extra  $1/f$  noise. However this is not the reason for the deviation observed here since it was common to see full, suppressed and enhanced noise in different barriers in the same sample. In other words, the observed deviation does not resemble systematic errors, but rather a barrier specific phenomenon. In addition, the measured noise power was always frequency independent, excluding  $1/f$  noise as a possible case.

Figure 5.3 shows noise in one barrier as a function of the dc bias at different

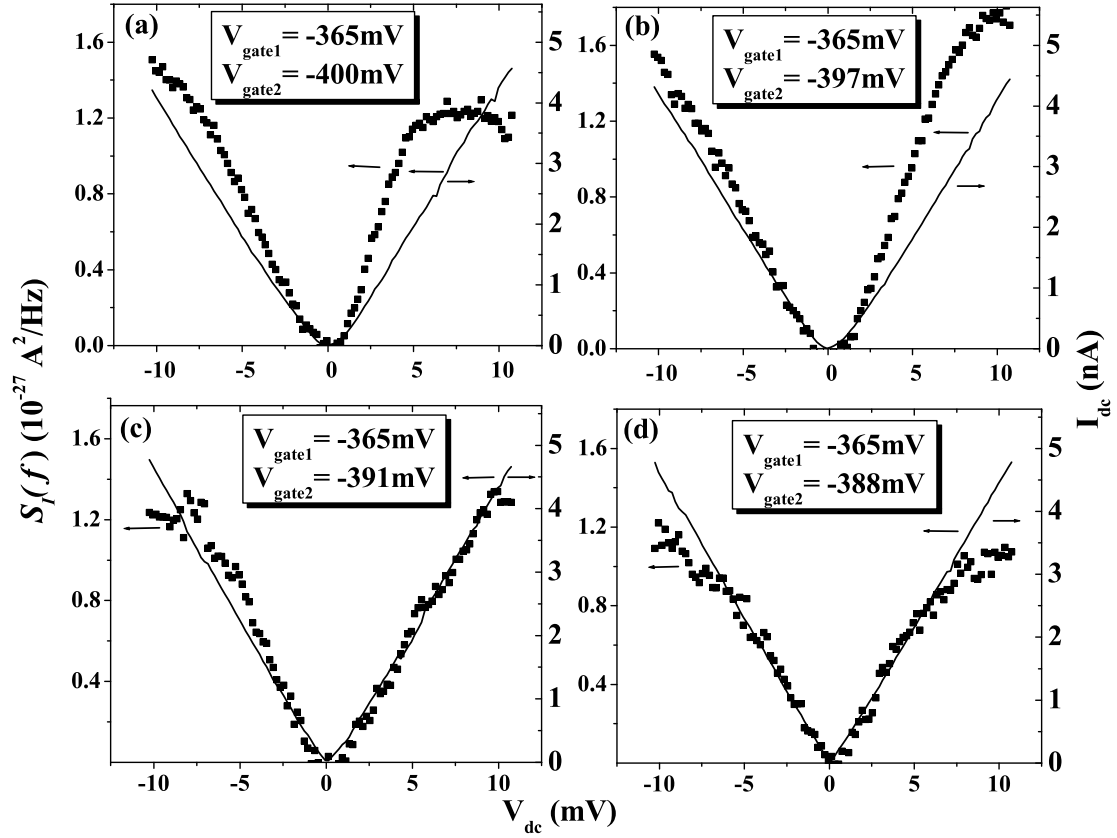


Figure 5.3: Shot noise as a function of dc bias for the same barrier at different gate settings. Points are measured noise (left scale). Solid lines are for  $F=1$  and are obtained by multiplying the  $|I| \sim V$  data by  $2e$  (left scale). They also represent the  $|I| \sim V$  data when the right scale is used.

gate settings. In this type of measurement the conductance and noise are measured simultaneously while the dc bias is swept slowly by a function generator. The data acquisition procedure was the same as used in Fig. 5.2. The conductance data, namely the  $I \sim V$  curve, is multiplied by  $2e$  to give the theoretical value for  $F=1$ , shown as solid lines in the figure. The actual Fano factor can be calculated by dividing the experimental data (dotted curve) by the solid curve.

At all four different gate settings, the conductance of the barrier increased as the bias increased from zero to finite values. For example, in (a)  $G=0.0025 e^2/h$  for zero bias and increases to about  $0.011 e^2/h$  for the highest positive bias. Correspondingly, the Fano factor changes from 2 to 0.75. This general trend is also true when the noise at different gate voltages are compared. As the voltage on gate 2 is changed from -400 mV to -388 mV ((a)  $\rightarrow$  (b)), the conductance at 1 mV bias changes from  $0.008 e^2/h$  to  $0.011 e^2/h$  and the fano factor changes from bigger than 1 to less than 1. Other than this trend, the measured shot noise is a complex function of both the bias and gate voltages. Again suppressed, enhanced, and full shot noise were observed. Even for a fixed gate setting the Fano factor can have significant changes as the dc bias is swept, going from enhanced to suppressed as in (a). In general there is no simple dependence of the measured noise on the parameters.

Given the fact that the shot noise theory of a tunnel barrier has been well established and tested in other systems, our data suggests that the transport mechanism in our samples may be more complicated than in simple tunnel barriers.

Indeed, people have measured deviations from full shot noise in various mesoscopic samples. For instance open quantum channels ( $T_j \sim 1$ ) or the ensemble averaging process in diffusive conductors can suppress shot noise [106, 107]. These two effects should not take place here since our samples have very high resistance ( $T_j \sim 0.005$ ) and the scattering range of the barrier (a few hundred nm) is very short compared to the mean free path (several  $\mu\text{m}$ ). Shot noise enhancement has been reported for a resonant tunneling diode biased in the negative differential conductance regime [47]. However, no negative differential conductance was observed in our samples. Actually the purpose of the measurement in Fig. 5.3 was to relate the shot noise of a barrier to its conductance. However, the measured conductance actually has the simple behavior of a typical tunnel barrier. This suggests that as the dc bias and gate settings change, the microscopic transport picture of the barriers undergoes changes that may not be detectable by simple conductance measurements but that can be revealed by shot noise measurements. In other words, shot noise depends on microscopic details in the vicinity of the tunnel barriers. Additional evidence is found in the asymmetry in dc bias evident in Fig. 5.3. Although in all cases the I-V curves are quite symmetric with respect to positive and negative bias, the shot noise can be very asymmetric. For a two terminal measurement, like the one shown in Fig. 5.3, the potential profile of the barrier seen by electrons is different for positive and negative bias. As a result, the noise may change as the bias is reversed.

To better understand the dependence of the noise on the microscopic details, spectroscopy measurements were used. For the data shown in Fig. 5.4, a constant

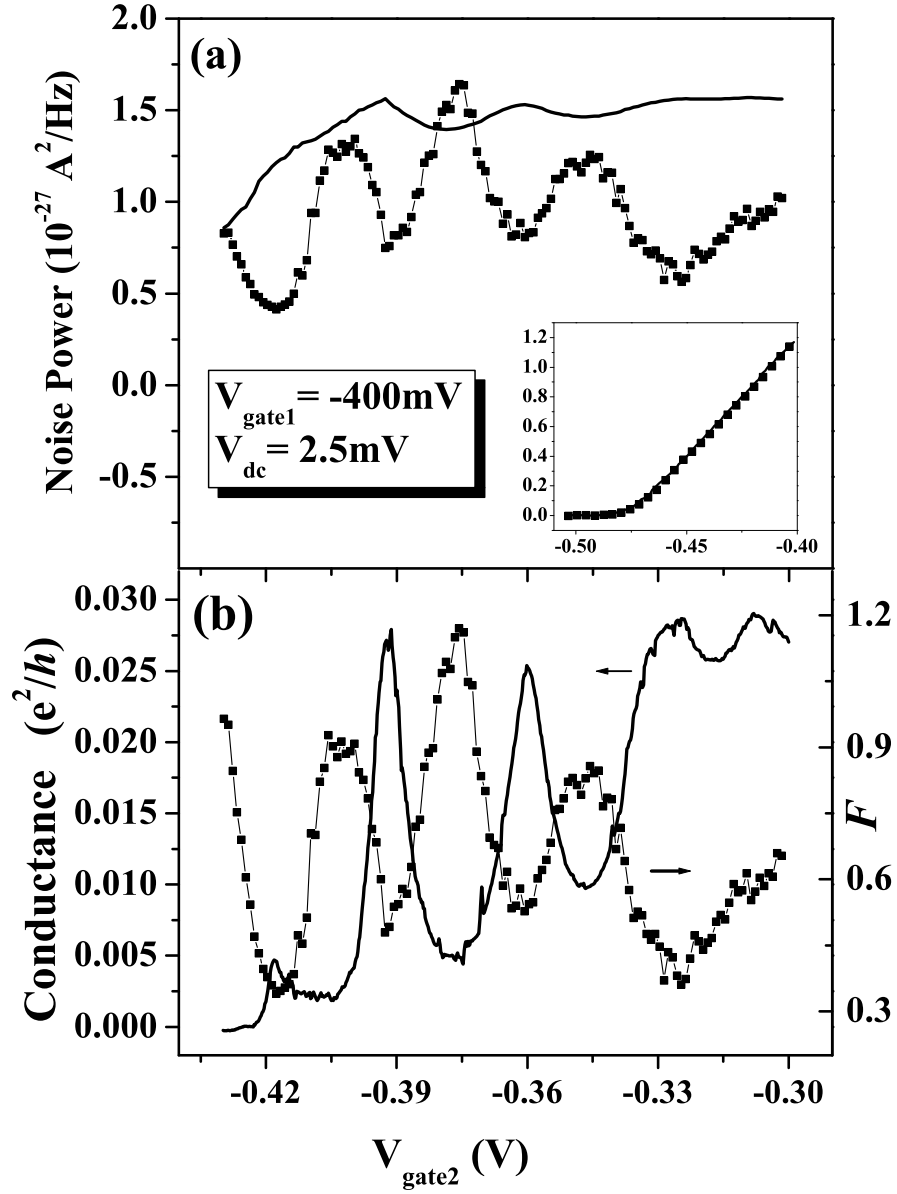


Figure 5.4: Shot noise as a function of gate voltage. (a) The squares show noise; the solid line is for  $F = 1$ , obtained by multiplying the I-V data by  $2e$ ; the inset shows the same measurement for a different barrier where experimental data agrees with the shot noise theory for an ideal tunnel barrier. (b) The solid line is the I- $V_{\text{gate}}$  curve measured at  $V_{\text{ac}} = 3\mu\text{V}$ ; the squares are the Fano factors of the measurement in (a).

dc bias of 2.5 mV was applied across the barrier while the current and noise were simultaneously measured as a function of the voltage on gate 2. Gate 1 was kept at a constant voltage. In the whole range of  $V_{gate2}$ , the conductance of the barrier varied between  $0.002 e^2/h$  and  $0.05 e^2/h$  (i.e.,  $T_j = 0.001$  to  $0.025$ ) so that full shot noise should be expected. Again, as in Fig. 5.3, the  $I-V_{gate2}$  curve is multiplied by  $2e$  to represent the theoretical value for  $F = 1$ , and the actual Fano factor is the ratio of two curves (plotted as the squared curve in Fig. 5.4(b)). For some barriers, we indeed observe full shot noise, as shown in the inset of Fig. 5.4(a). However, deviations from full shot noise were observed in some barriers, as shown in Fig. 5.4(a). For most of the measurement range the shot noise is suppressed. As the gate voltage changes the shot noise power oscillates, corresponding to  $F$  oscillating between 0.3 and 1.15. The  $I-V_{gate2}$  curve (the solid line in Fig. 5.4(a)) also has a complex structure. It is clear from this data that the pinch off process of the barrier is non-trivial. Due to the high dc bias used (2.5 mV), peaks in the  $I-V_{gate2}$  curve are not well isolated, so it is difficult to establish a correspondence between this curve and the shot noise data. Figure 5.4(b) shows the conductance (solid curve) of the same barrier measured at a small ac bias using a lock-in technique. Peaked structure is found on top of a decreasing background as the gate voltage is decreased. On the same plot is the Fano factor of the dc measurement in Fig. 5.4(a).  $F$  has minima wherever the conductance has maxima and vice versa.

The peaks on the conductance curve suggest resonant tunneling or phonon assisted tunneling (hopping) through localized states in the barrier. These transport

mechanisms have been studied in various mesoscopic samples [108, 109]. They have also been predicted to suppress shot noise [79, 110]. In the case of one localized state the tunneling can be described by two leak rates,  $\Gamma_{L,R} \propto \exp(-2r_{L,R}/r_0)$ , where  $r_{L,R}$  are the distance between the localized state and the two contacts and  $r_0$  is the localization radius of the state. Shot noise is suppressed by a Fano factor of  $F = (\Gamma_L^2 + \Gamma_R^2)/(\Gamma_L + \Gamma_R)^2$  [44]. This result applies to both resonant tunneling and hopping [44].  $F$  ranges from 0.5 to 1 depending on the relative size of  $\Gamma_L$  and  $\Gamma_R$ .

Resonant tunneling conductance through one localized state at zero temperature can be described by [111]:

$$G = \frac{e^2}{h} \frac{\Gamma_L \Gamma_R}{(\delta E)^2 + \left(\frac{\Gamma_L + \Gamma_R}{2}\right)^2}, \quad (5.2)$$

where  $\delta E = E_0 - \mu$ ,  $E_0$  being the resonant level energy and  $\mu$  being the chemical potential of the contacts.  $\delta E$  is related to the gate voltage  $V_g$  by  $\delta E = eaV_g - \mu$ . The factor  $a$  has a typical value of the order of 0.1 [71]. This equation can be written in the form

$$G = G_0 \frac{1}{1 + \left(\frac{2eaV_g - \mu}{\Gamma_e}\right)^2}, \quad (5.3)$$

where  $G_0$  is the peak value of  $\frac{4e^2}{h}(\Gamma_L \Gamma_R)/(\Gamma_L + \Gamma_R)^2$  and  $\Gamma_e = \Gamma_L + \Gamma_R$  is the line width of the resonant state. This result has a Lorentzian form.

At finite temperature, thermal broadening should be taken into account, so that

$$G = G_0 \int \frac{1}{1 + \left(\frac{2eaV_g - \mu}{\Gamma_e}\right)^2} \frac{df(E, \mu)}{dE} dE, \quad (5.4)$$

where  $f$  is the Fermi-Dirac distribution. For  $\Gamma_L + \Gamma_R \ll k_B T$  the Lorentzian in equation 5.3 looks like a  $\delta$ -function, and

$$G \sim \frac{df(E_0 - \mu)}{dE} = \frac{f(1-f)}{k_B T}, \quad (5.5)$$

which has a line width of  $3.5 k_B T$ . In order to use this form to fit the conductance data in Fig. 5.4(b), an unreasonably small  $a$  ( $\sim 0.002$ ) is needed, which is very unlikely in the current system. In the other extreme of  $\Gamma_L + \Gamma_R \gg k_B T$ , the  $df(E, \mu)/dE$  looks like a  $\delta$  function and  $G$  has the form given by Equation 5.3. The solid curve in Fig. 5.5 shows a fitting to the peak at  $V_{gate2} = -0.392$  V in Fig. 5.4(b) with equation 5.3. The following parameters are used:  $\Gamma_L = 795 \mu\text{eV}$ ,  $\Gamma_R = 5 \mu\text{eV}$  and  $a = 0.1$ .

I also tried to fit the conductance data with a modified resonant tunneling model which incorporates inelastic scattering. In such a case, the conductance has the form [112]

$$\begin{aligned} G &= \frac{e^2}{h} \frac{\Gamma_L \Gamma_R}{\Gamma_L + \Gamma_R} \frac{\Gamma}{(\delta E)^2 + (\Gamma/2)^2} \\ &= G_0 \frac{1}{1 + \left(\frac{2eaV_g - \mu}{\Gamma}\right)^2}, \end{aligned} \quad (5.6)$$

where  $\Gamma = \Gamma_L + \Gamma_R + \Gamma_{in}$  and  $\Gamma_{in}$  is the inelastic scattering line width. This is in the same form as equation 5.3 except that  $\Gamma_e$  is replaced by  $\Gamma$ . With this model

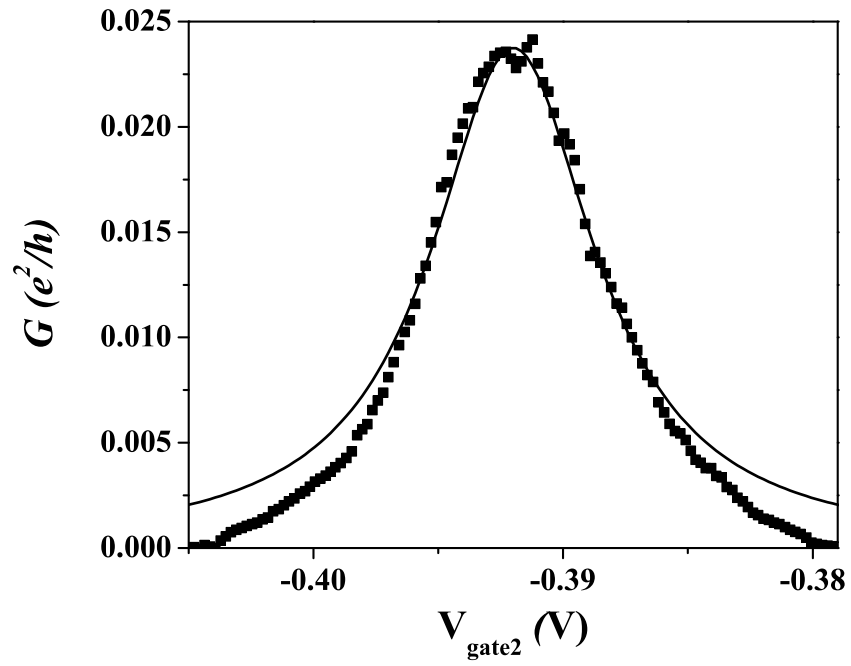


Figure 5.5: Shot noise data (squares) together with fit (line) to equations 5.3 or 5.6 using the conductance data.

the following fitting parameters are obtained:  $\Gamma_L = \Gamma_R = 9.5 \mu\text{eV}$ ,  $\Gamma = 800 \mu\text{eV}$  and  $a = 0.1$ . Both fittings fall too slowly on the tails, which suggests that resonant tunneling through one localized state is not the only transport mechanism. This is further confirmed by the fact the maximum  $F$  in Fig. 5.4(b) is 1.15 at  $V_{gate2} = -0.375 \text{ V}$ , while the shot noise theory for single state resonant tunneling predicts a maximum  $F$  of 1. The same argument applies to hopping processes. In the next section, I will try to develop a microscopic model to understand the results shown in this figure.

I also observed enhanced noise in some barriers, as shown in Fig. 5.6. This is the same type of measurement as that shown in Fig. 5.4. As the gate voltage changes, the noise exhibits both suppression and enhancement. Figure 5.6(b) is for the same barrier but with different settings. Compared to Fig. 5.6(a), the voltage on gate 1 is 20 mV higher; correspondingly the highest peak shifts by 30 mV and two peaks in Fig. 5.6(a) disappear.  $F$  of the highest peak increases by a factor of 3. The largest enhancement corresponds to a Fano factor  $F \approx 11$ . This barrier has a simple I-V, similar to that of the barrier in Fig. 5.3. No negative differential conductance was observed, so again the shot noise enhancement can not be related to that mechanism.

Figures 5.6(c) and (d) show closer views for the enhanced shot noise peaks observed in the same barrier at different gate settings. Figure 5.6(d) shows that the shot noise enhancement mechanism in the sample could be unstable. The enhancement experienced an abrupt change as the gate voltage was varied. The position

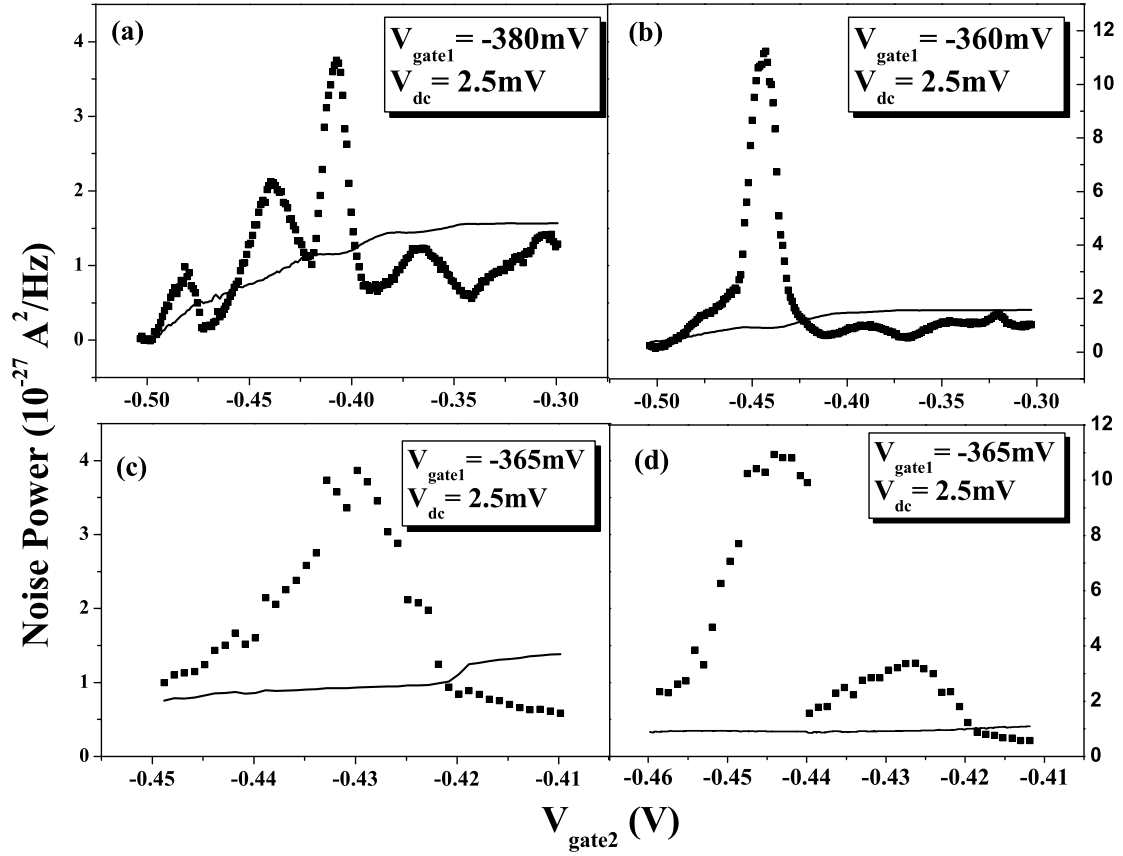


Figure 5.6: Enhanced noise for the same barrier at different gate settings; solid lines are for  $F = 1$ .

where this jump happens and the size of the jump may not be reproducible in different measurements. This implies that some other very slow (the time scale could be hours) mechanism, such as impurity motion may also exist in the system.

In this section, I have discussed the noise measured in tunnel barriers fabricated in GaAs/AlGaAs heterostructures. In contrast to expectations, our data shows that the noise of tunnel barriers contains very rich physics. In the next section, I will try to relate the shot noise of tunnel barriers to their microscopic structure and explain the data presented in this section.

### 5.3 Numerical simulation and modelling

In this section I present some numerical simulations of shot noise in tunnel barriers with different microscopic details. These simulations help us interpret deviations from full shot noise. I will then develop a microscopic model to explain some of the data presented in the previous section.

Equation 5.1 describes the shot noise of an ideal tunnel barrier in which electrons tunnel through the barrier. Under such a condition, electrons tunnel randomly and independently, thus a Poissonian process and full shot noise are expected. This picture is appropriate for systems like a STM tip very close to a metallic surface, where the tunneling occurs in an atomic size region. For mesoscopic barriers fabricated in semiconductor heterostructures, the situation is more complicated mainly due to two new features. First, potential disorder and impurities can cause localized states in semiconductor heterostructures. As a result, transport mechanisms

like resonant tunneling and phonon-assisted tunneling should be taken into account. Second, in mesoscopic samples Coulomb interaction and Fermi statistics are very important and they can change shot noise significantly.

In the following, I present some numerical simulations for a barrier with different localized state configurations. Coulomb interactions will also be considered in most cases. The essence of the simulation is the following: for a configuration with all the tunneling rates specified, the tunneling probability density function can be calculated; with this function and a random number generator, one can generate a series of random tunneling events in the time domain, namely the tunneling current  $i(t)$ . This simulation models a real tunneling process happening for a fixed configuration. The shot noise ( $\propto (\overline{i^2} - \bar{i}^2)$ ) can then be calculated.

The first case considered is that of an ideal tunnel barrier with no localized states, as illustrated in Fig. 5.7(a). Electrons directly tunnel through the barrier. The simulation always gives a Fano factor of 1, as expected.

The second case is with one localized state, characterized by two leak rates  $\Gamma_1$  and  $\Gamma_2$ , as illustrated in Fig. 5.7(b). The Coulomb interaction is taken into account in the following way: once an electron tunnels onto the localized state, it blocks all other electrons from tunneling. This effect regulates consecutive tunneling events and is expected to suppress shot noise. Theory predicts that the Fano factor in this case is [113, 114]

$$F = \frac{\Gamma_1^2 + \Gamma_2^2}{(\Gamma_1 + \Gamma_2)^2}. \quad (5.7)$$

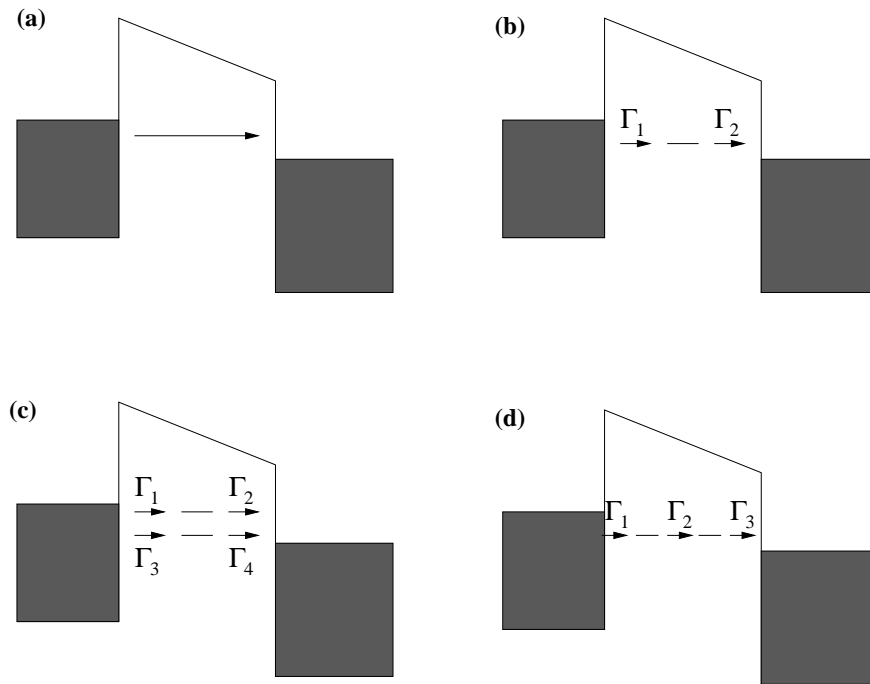


Figure 5.7: Tunnel barriers with different localized states configurations: (a) no localized state; (b) one localized state; (c) two independent localized states; (d) two localized states in series.

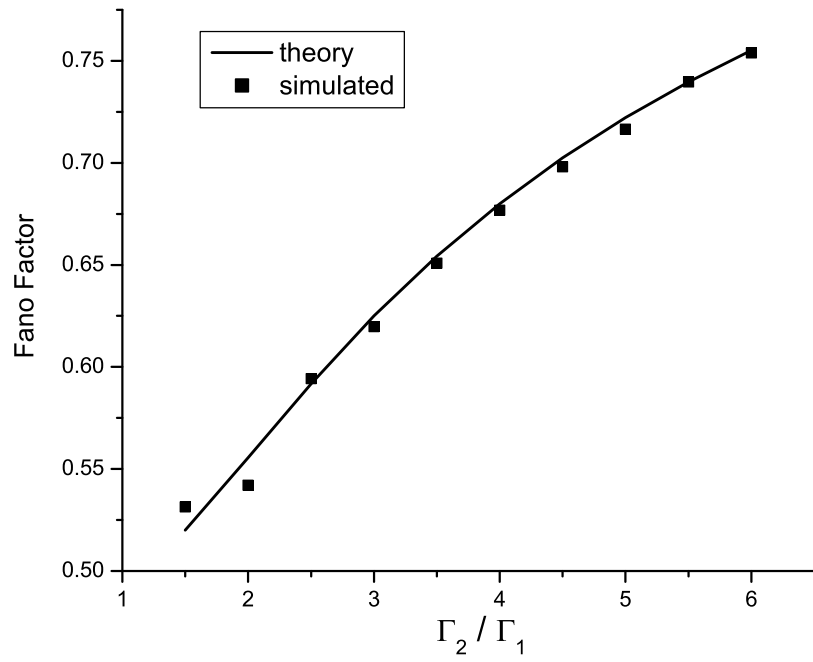


Figure 5.8: Numerical simulation and theoretical prediction for Fano factor for tunneling through one localized state.

Figure 5.8 shows numerical simulations and the theoretical prediction. Depending on the ratio of  $\Gamma_1$  and  $\Gamma_2$ ,  $F$  changes between 0.5 and 1. The simulation agrees well with the theory.

The third case is that of two independent localized states. Again, Coulomb interaction is considered for both states, but there is no correlation between them. The Fano factor for tunneling through two parallel channels is:

$$F = \frac{F_1 I_1 + F_2 I_2}{I_1 + I_2}, \quad (5.8)$$

where  $F_{1,2}$  and  $I_{1,2}$  are the Fano factor and current of the two states.  $F_1$  and  $F_2$  can both change between 0.5 and 1, while  $F$  always lies in between  $F_1$  and  $F_2$ . Figure 5.9 shows a simulation where  $\Gamma_1$  and  $\Gamma_2$  are fixed and the ratio of  $\Gamma_4/\Gamma_3$  changes.

For the first three cases, the simulation results agree well with the theory. The discrepancy between them at some points is likely caused by the finite number of samples used in the numerical simulations, and decrease as more samples are used. This agreement justifies our numerical simulation method, and suggests we can confidently simulate more complicated configurations where an analytical expression for  $F$  is not available or not easy to find.

The next case is that of two localized states in series, characterized by three leak rates, as shown in Fig. 5.7(d). Figure 5.10 shows the simulation result. The solid line is a fit of the simulation data to the formula

$$F = \frac{\Gamma_1^2 \Gamma_2^2 + \Gamma_2^2 \Gamma_3^2 + \Gamma_3^2 \Gamma_1^2}{(\Gamma_1 \Gamma_2 + \Gamma_2 \Gamma_3 + \Gamma_3 \Gamma_1)^2}. \quad (5.9)$$

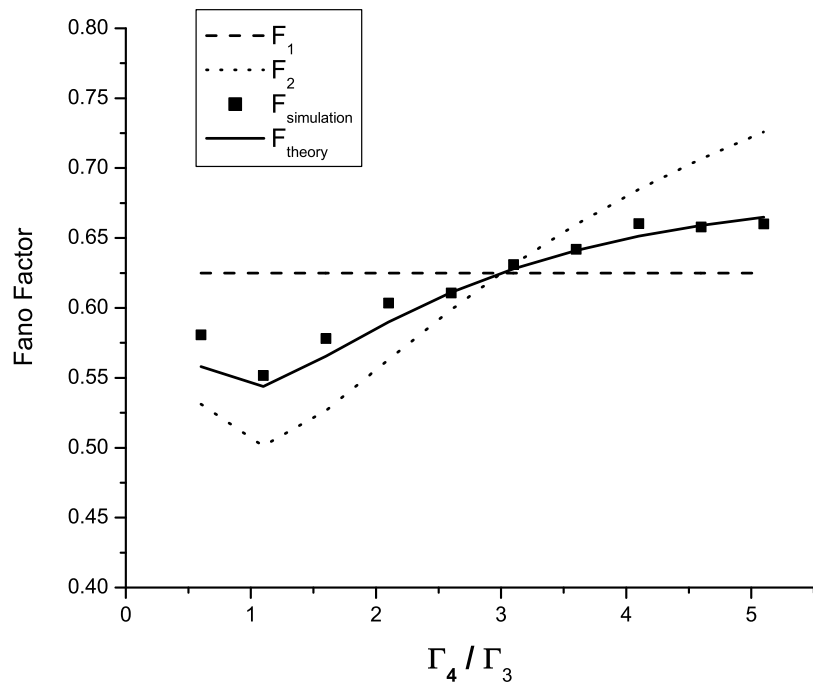


Figure 5.9: Numerical simulation and theoretical prediction for two independent localized states.

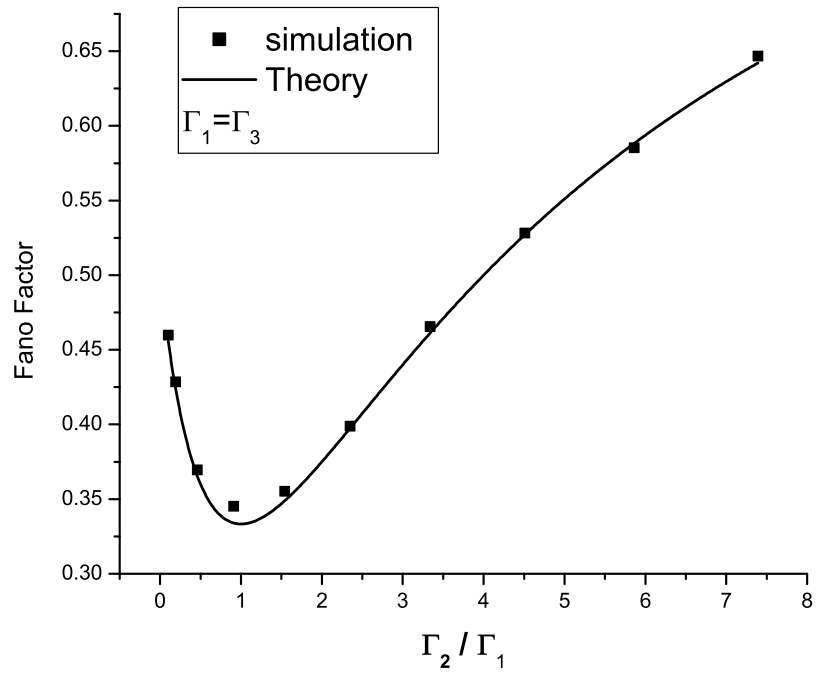


Figure 5.10: Numerical simulation and theoretical prediction for two localized states in series.

This formula was confirmed later by an analytical calculation. According to equation 5.9, the minimum of  $F$  occurs at  $\Gamma_1 = \Gamma_2 = \Gamma_3$  and is equal to  $1/3$ . For all the cases discussed so far, this is the only case where  $F$  can go below 0.5. On the other hand, if one of the  $\Gamma$ 's is much less than the others,  $F$  approaches one. This is expected since in that case one tunneling site dominates the whole transport process.

The simulation method and Fano factor calculation can also be done for more than two localized states. I will not discuss the details here but give some brief results. In the case of  $N$  localized states in series, shot noise can be suppressed by a Fano factor of  $1/(N + 1)$  if all  $(N + 1)$  tunneling rates are equal [115]. For multiple tunneling paths in parallel and without any correlation, the overall Fano factor is always within the range defined by the minimum and maximum of the  $F$ 's of all paths.

In the one localized state case considered in Fig. 5.7(b), only one tunneling channel is allowed. Now let us generalize this case by allowing two tunneling channels through the same state. In the first path, electrons first hop from the left contact to the localized state with rate  $\Gamma_1$  and then hop to the right contact with rate  $\Gamma_2$ . In the second path electrons resonantly tunnel through the localized state characterized by rates  $\Gamma_3$  and  $\Gamma_4$ . In both paths consecutive tunneling events are regulated by Coulomb interaction. Let us further assume there is also a Coulomb correlation between the two paths, that is, an electron in the localized state blocks both paths and the electrons in the reservoirs cannot tunnel into the localized state until this

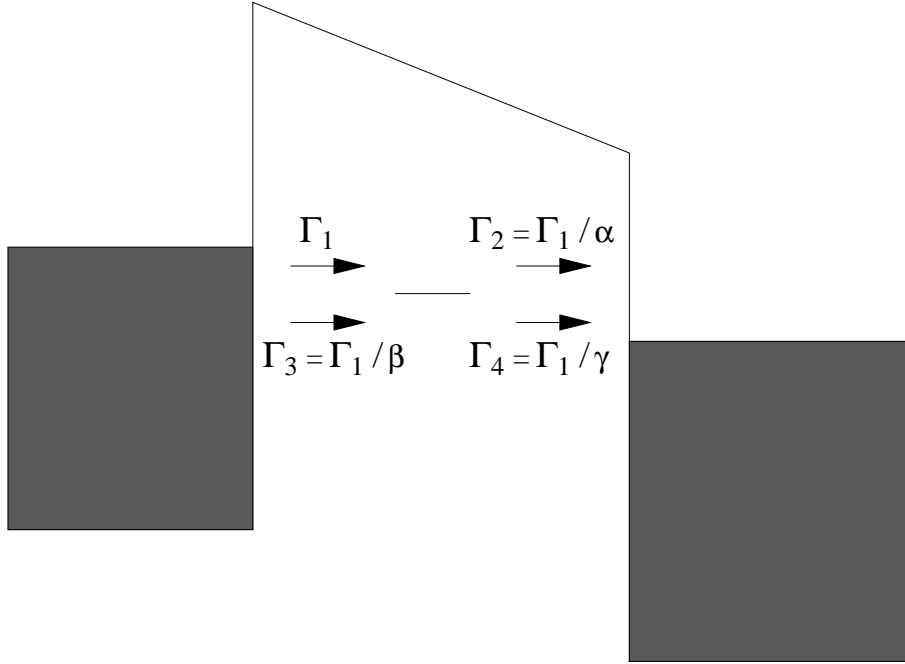


Figure 5.11: One localized state with two correlated tunneling paths

electron leaves. This case is illustrated in Fig. 5.11.

In order to do numerical simulations the following relation is used:  $\Gamma_1 = \alpha\Gamma_2 = \beta\Gamma_3 = \gamma\Gamma_4$ . Different combinations of  $\alpha$ ,  $\beta$  and  $\gamma$  are studied. Figure 5.12 shows the Fano factor as a function of  $\beta$  for the cases  $\alpha = \gamma = 0.1$ ,  $\alpha = \gamma = 1$ , and  $\alpha = \gamma = 10$ . The points are simulation results. Shot noise is suppressed in the whole parameter range simulated, with a maximum of 1 and a minimum of 0.5. When  $\beta \rightarrow 0$ ,  $F \rightarrow 1$ . As  $\beta$  increases,  $F$  saturates.

Physically,  $\beta \rightarrow 0$  (so  $\Gamma_3 \rightarrow \infty$ ) means electrons always resonantly tunnel through the barrier via the second path. The problem reduces to the case described by equation 5.7 but with  $\Gamma_1 \rightarrow \Gamma_3$  and  $\Gamma_2 \rightarrow \Gamma_4$ . For the second path,  $\Gamma_4 \ll \Gamma_3$ , thus

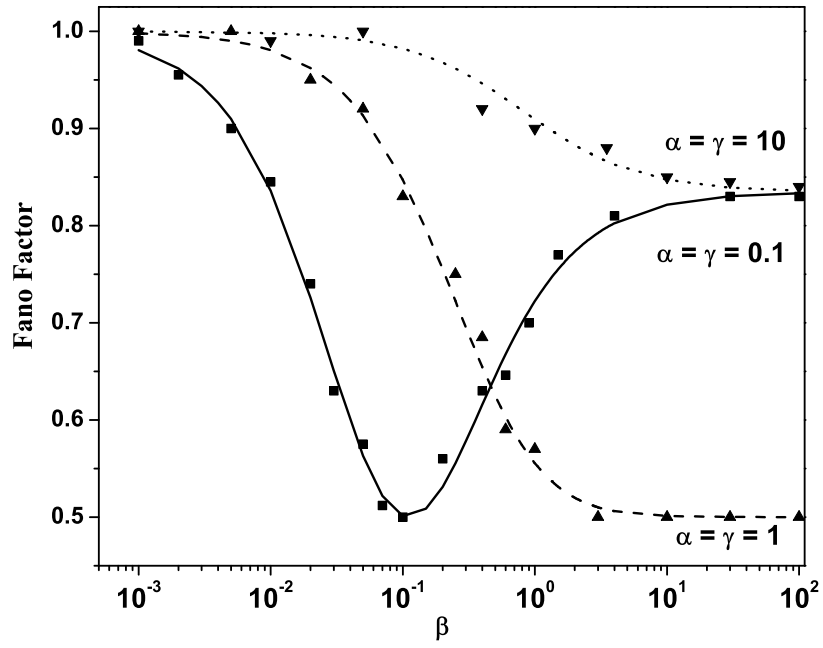


Figure 5.12: Simulation results of  $F$  as a function of  $\beta$  when  $\alpha = \gamma$ . Scattered points are simulation results and lines are fits to equation 5.10.

$F \rightarrow 1$ . This is somewhat counterintuitive, especially for the case where  $\alpha = \gamma = 10$ , where the average tunneling time for the first path is  $\Gamma_1^{-1} + \Gamma_2^{-1} = 11/\Gamma_1$  and for the second path is  $\Gamma_3^{-1} + \Gamma_4^{-1} = (\beta + 10)/\Gamma_1$ . As  $\beta \rightarrow 0$  the two tunneling times are very close, so one would expect that electrons should have almost equal probabilities of choosing any of the paths. However, this is only true when the two paths are not correlated. With the Coulomb correlation, the probability of a path to be chosen depends on the tunneling rate of its first step. As  $\beta \rightarrow 0$  the rate of the first step in the second path is very high, so electrons take this path exclusively. The  $F$  saturation at large  $\beta$  values can be explained in the same way. As  $\beta \rightarrow \infty$  electrons always choose the first path, so  $F$  can be calculated by equation 5.7, which is constant once  $\alpha$  is fixed. For  $\alpha = 0.1, 1$ , and  $10$ ,  $F$  goes to  $0.835, 0.5$ , and  $0.835$  respectively as  $\beta \rightarrow \infty$ .

Figure 5.13 shows the simulation results (points) for another case where  $\alpha = 1$ , so the first path is symmetric. As before, when  $\beta \rightarrow 0$ ,  $F \rightarrow 1$ . This was explained above. As  $\beta \rightarrow \infty$ ,  $F \rightarrow 0.5$  for all different  $\gamma$  values. The reason is that as  $\beta \rightarrow \infty$  electrons always choose the first path to tunnel. Since now for the first path  $\Gamma_1 = \Gamma_2$ ,  $F = 0.5$  according to equation 5.7. The most important feature in this case is the shot noise enhancement in some parameter range. By comparing this figure to Fig. 5.12, one can find that whenever  $\alpha = \gamma$ , shot noise is suppressed. Shot noise enhancement is possible only when  $\alpha \neq \gamma$ . In order to understand the origin of the enhancement, let us consider the tunneling events in the time domain.

Suppose we put an electron detector that is sensitive enough to record single

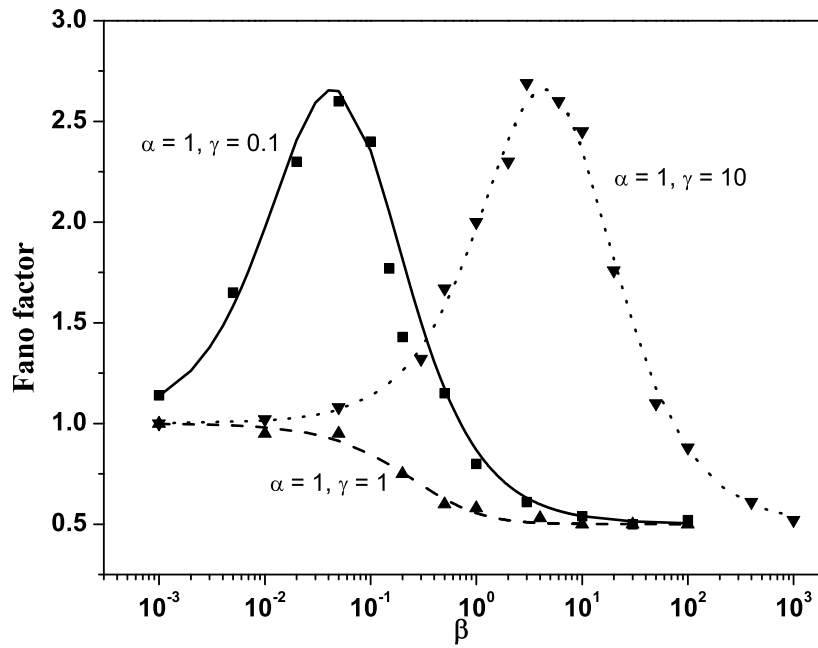


Figure 5.13: Simulation results of  $F$  as a function of  $\gamma$  when  $\alpha = 1$ . Points are results of the simulation and lines are fits to equation 5.10.

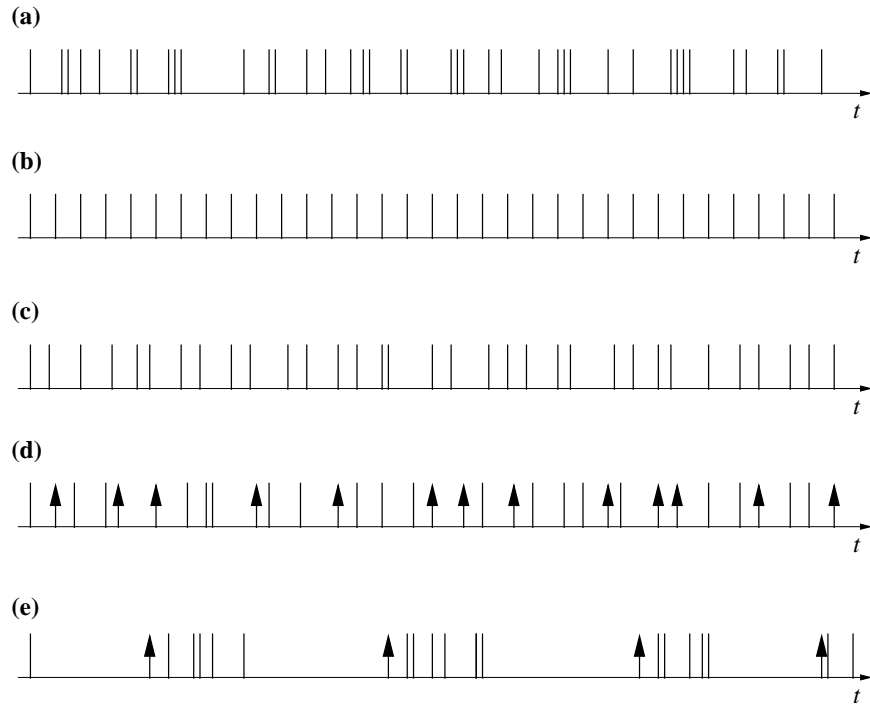


Figure 5.14: Time sequence of tunneling events: (a) an ideal barrier; (b) an electron pump; (c) tunnel barrier with one localized state; (d) tunnel barrier with two independent paths; (e) tunnel barrier with two Coulomb correlated tunneling paths. In (d) and (e) two different types of bars are for tunneling events through different paths.

electron tunneling events as a function of time. Figure 5.14 shows a section of the time sequence of tunneling events recorded for different cases: (a) is for an ideal tunnel barrier where electrons tunnel randomly and independently. The arrival time of electrons has a Poisson distribution, thus  $F = 1$ . (b) shows an extreme case where electrons tunnel through an “electron pump”<sup>1</sup>, so consecutive events are equally spaced. Since the arrival time has no distribution,  $F = 0$ . (c) is for a tunnel barrier with one localized state. The arrival time has a distribution, but is sub-Poissonian due to the Coulomb regulation effect on consecutive events, thus  $0 < F < 1$ . (d) is for the case of two independent tunneling paths. Here I use two different symbols for electrons tunneling through different paths. There is no correlation between the two categories and each category has a sub-Poissonian distribution, so the overall Fano factor also satisfies  $0 < F < 1$ . Figure 5.14(e) corresponds to the special case illustrated in Fig. 5.11 with  $\gamma \gg \alpha$  (assuming the bars without arrows are from path 1). Under such condition  $\Gamma_4 \ll \Gamma_2$ , so whenever an electron chooses the second path, it will block other electrons for a long time about  $\Gamma_4^{-1}$ . As a consequence electrons will tunnel through the barrier in a “bunched” manner, as shown in (e). The current fluctuations in this case are expected to be larger than those in the case where electrons are not “bunched”. On the other hand, for each tunneling path the Coulomb regulation still exists and will reduce the fluctuations. The actual current fluctuations depend on the relative weight of these two effects. For very different

---

<sup>1</sup>An electron pump is such a device that the tunneling time for each electron can be precisely controlled.

$\alpha$  and  $\gamma$ ,  $F > 1$  is obtained; however, if  $\gamma \approx \alpha$ , the Coulomb regulation for each path dominates, and the result is  $F < 1$ . This argument explains our numerical simulation results.

So far the discussion of the tunneling process in Fig. 5.11 is all qualitative. By considering the physical meaning and asymptotic behaviors, I have argued that the numerical simulation results are reasonable. Even though the simulation method should work here because it has been applied to many other cases and has agreed well with theory, an analytical result is still very helpful for further study. After the simulation, I calculated the Fano factor for this case and found the following result:

$$F = \frac{\beta^2 + \alpha^2\beta(2 + \beta) - 2\alpha\beta\gamma + \gamma^2 + 2\beta\gamma^2}{(\beta + \alpha\beta + \gamma)^2}. \quad (5.10)$$

This equation is then compared to the numerical simulation results in Fig. 5.12 and Fig. 5.13 (see the lines in the two figures). Good agreement is found in both cases. With this equation one can explore a larger parameter space. It can be easily shown that  $F$  has no upper bound and has a minimum of 0.5 if  $\beta = \frac{\alpha}{1-\alpha}$  and  $\gamma = \alpha$ .

Another way to view this shot noise enhancement is to say that the fast tunneling path is modulated by the slow tunneling path. This modulation mechanism can also be found in other cases. For example in the case shown in Fig. 5.7(c), if the two localized states are very close to each other, then Coulomb interaction between them has to be taken into account. When one electron tunnels into one state it will shift the potential profile nearby due to the Coulomb interaction. As a

result, no electron can tunnel to either state until the first electron leaves. Under such a condition the two states are Coulomb correlated. Imagine  $\Gamma_2$  and  $\Gamma_4$  are very different, then the tunneling across the whole barrier can be switched on and off depending on the occupation status of the slow tunneling state. This again results in “bunched” tunneling events and enhanced shot noise.

So far, I have discussed the shot noise in a tunnel barrier with a few different impurity configurations. to summarize, I list the main results: (1) full shot noise only shows up in an ideal tunnel barrier; (2) tunneling through  $N$  localized states in series can suppress the shot noise by a factor of  $1/(N+1)$ ; (3) for a set of independent paths characterized by Fano factors  $F_1, F_2, \dots, F_N$ , the overall Fano factor always satisfies  $\min\{F_1, F_2, \dots, F_N\} < F < \max\{F_1, F_2, \dots, F_N\}$ ; (4) shot noise may be enhanced when parallel tunneling paths are correlated by Coulomb interaction.

In principle, it appears that the results given here can explain all the experimental data presented in the previous section. The missing link in determining if this really is the cause is the lack of microscopic details of localized states and impurities in the vicinity of the tunnel barriers. Additionally, how these details change as gate voltages are tuned is also very important. Unfortunately information about these details appears to be difficult to obtain. In the following, I will try to apply the model discussed in Fig. 5.11 to the data in Fig. 5.4, which contains information on conductance measurements that can be used as a cross check of our modeling.

As pointed out in the previous section, the peaks in the ac conductance measurements shown in Fig. 5.4(b) can not be fitted by the theory of resonant tunneling

through one localized state. Also, that theory can not account for the enhanced shot noise. In that fitting the tunneling rates were assumed to be constant as a function of the gate voltage. Generally speaking this may not be true. As the gate voltage is tuned the localized state is also shifted, so the coupling between the state and the two contacts can also change. In the following, I will assume that  $\alpha, \beta$  and  $\gamma$  in equation 5.10 are functions of the gate voltage. Within this model the conductance and the Fano factor can be calculated as

$$G(V_g) = \frac{4\alpha\beta\gamma}{(\beta + \gamma)(\alpha\beta\gamma + \alpha\beta + \beta\gamma + \gamma\alpha)} \times \frac{1}{1 + \left(\frac{e\alpha(V_g - V_0)}{\Gamma_1(1+1/\alpha+1/\beta+1/\gamma)}\right)^2}, \quad (5.11)$$

$$F(V_g) = \frac{\beta^2 + \alpha^2\beta(2 + \beta) - 2\alpha\beta\gamma + \gamma^2 + 2\beta\gamma^2}{(\beta + \alpha\beta + \gamma)^2}, \quad (5.12)$$

where  $V_0$  is the gate voltage at which conductance peaks occur.

Figure 5.15 shows a fit of part of the data in Fig. 5.4 (for the range  $-0.495V < V_g < -0.345V$ ) to equations 5.11 and 5.12. The following parameters are used: for peak 1,  $\alpha = 0.1$  and  $\Gamma_1 = 100 \mu eV$ ; for peak 2,  $\alpha = 0.1$  and  $\Gamma_1 = 120 \mu eV$ .  $\beta, \gamma$  used are given in Fig. 5.16.

I want to point out that given the large phase space of  $\alpha, \beta$  and  $\gamma$ , it is possible to fit the experimental data with other combinations of these parameters. In this sense, the fit in Fig. 5.15 cannot be an exact simulation of the system. In order to justify a specific choice of parameters, further knowledge of the microscopic details

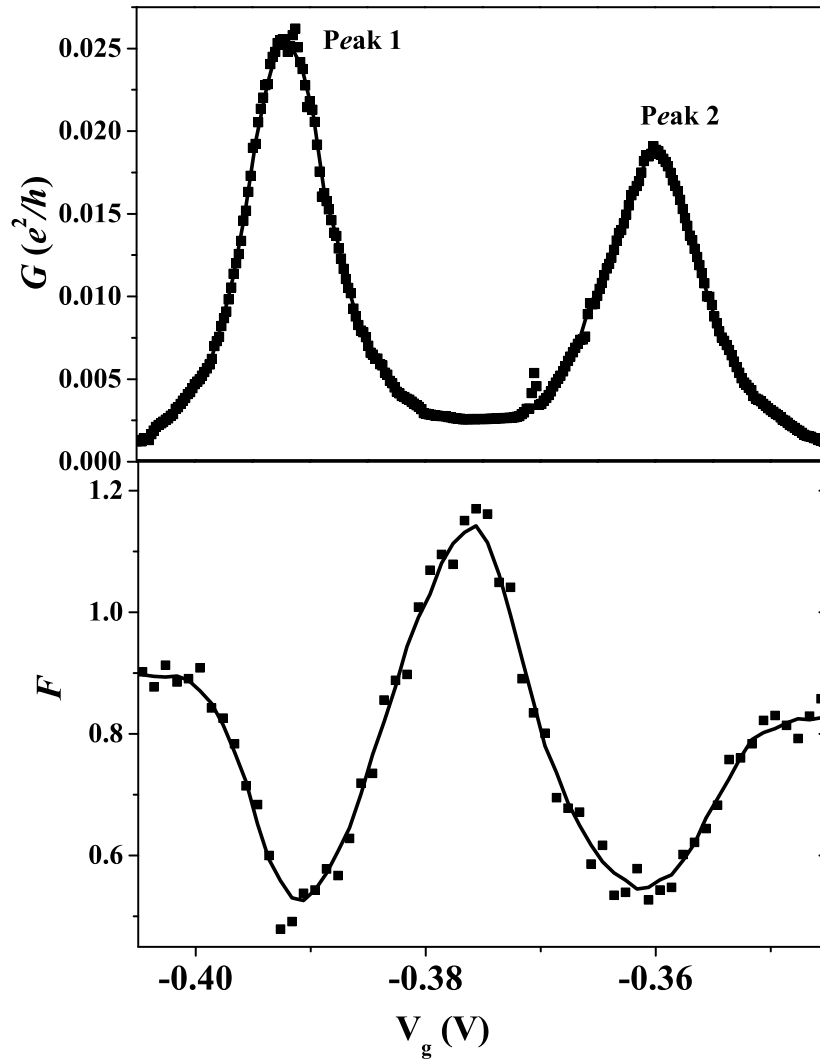


Figure 5.15: Fit of part of the data in Fig. 5.4 ( $-0.495V < V_g < -0.345V$ ) to equations 5.11 and 5.12: (a) conductance; (b) Fano factor.

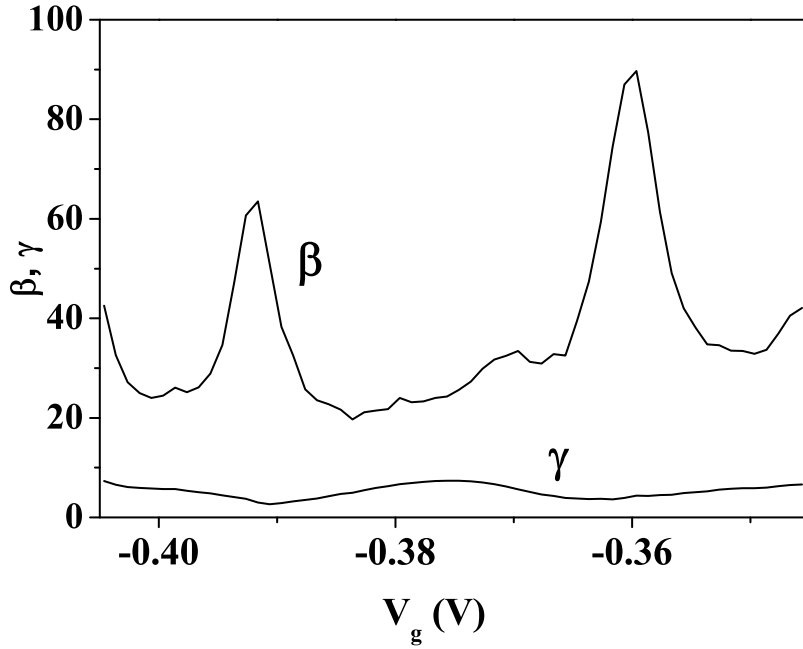


Figure 5.16: Gate voltage dependence of parameters used for fits in Fig. 5.15.

in the barrier is required. Nevertheless, the good agreement between the theory and data shows that this model is capable of reproducing the most important features of the measurements by comparing the experimental data to a possible configuration of the model.

The main features of the data modeled in Fig. 5.15 include: the Fano factor oscillates as  $V_g$  is tuned; the minimum Fano factor is 0.5 while the maximum is larger than 1; the Fano factor anti-correlates with the conductance. By allowing  $\alpha, \beta$  and  $\gamma$  to vary as a function of  $V_g$ , our model can produce oscillating Fano factors. The shot noise suppression and enhancement has been explained above. The anti-correlation between the conductance and shot noise can be explained by

the fact that as the gate voltage is tuned, the ratio between resonant tunneling and hopping also changes. Off the conductance peaks  $\beta$  is small, which means more electrons choose the second path hopping, while the blocking time  $\Gamma_4^{-1}$  is larger, so the bunching effect is more significant than that on resonance. As a result  $F$  is larger off the conductance peaks.

## 5.4 Summary

In the context of shot noise, tunnel barriers have received much less attention than other mesoscopic structures. This is mainly due to the simplicity of ideal tunnel barriers, so not much interesting physics has been expected from such systems. For an ideal tunnel barrier in which no localized states (generated by impurities and/or potential disorder) are found, electrons can only directly tunnel through the barrier and full shot noise is expected. In terms of localized states, barriers fabricated in metallic systems are usually cleaner. As a result the shot noise measured in these samples shows very good agreement with the theory for ideal barriers. For barriers with additional structure, shot noise generally deviates from the classical value and can have a very complicated gate and bias dependence, due to microscopic details.

Shot noise becomes even more complicated when these microscopic details are time dependent. In such a case the conductance of the barrier,  $T_j$ , is a time varying quantity. The model of Coulomb correlated tunneling paths discussed in the previous section is such an example. A similar model was studied by Safonov *et al.* [105], where the resonant tunneling through a localized state was modulated

by another nearby localized state. In both examples fast modulation was assumed, which means the conductance change is so fast that it only affects shot noise, while the normal conductance measurements are totally insensitive to it. Sometimes the modulation can be very slow, for example a modulation caused by a deep impurity state which takes a very long time to populate and depopulate. In such a case the modulation can be one of the causes of excess low frequency noise, such as  $1/f$  noise and random telegraph noise. The latter can also be monitored by normal conductance measurements.

In this chapter, I have discussed both stable and time dependent localized state configurations. For the stable ones, normal conductance measurements can also be used to study the behavior; for example, resonant tunneling and hopping are well studied subjects in mesoscopic physics. On the other hand, it turns out that shot noise can be very sensitive to the system details, and can supply additional information. For the time dependent cases, especially those of fast processes, shot noise detection can reveal much more physics than normal conductance measurements. This should be expected since shot noise measures the temporal correlation between electron transport events.

Finally, I note that the work reported here was the first comprehensive study of shot noise in mesoscopic semiconductor tunnel barriers. It was the initial step leading to a better understanding and characterization of the shot noise in more complicated mesoscopic systems.

## Chapter 6

### Shot noise study of quantum entanglement

In this chapter, I report my experimental result on shot noise properties of a coupled quantum dot system [116]. The main goal of this work is to demonstrate quantum entanglement of two electron spins as discussed in Chapter 3. In the first section, I discuss the preparation work needed in order to make the measurement and some related important issues. The second section shows my first results, which give possible evidence for entanglement. The third section provides deeper insights into various aspects of this experiment, while the last section gives a summary of the chapter.

#### 6.1 Experimental preparation

In this section I first give a brief description of the samples used in the entanglement experiment, followed by the discussion of relevant sample set-up issues. I will then talk about the experimental arrangements, and finally, I will discuss noise sources other than shot noise that are present in the system and how we handle and characterize them.

Figure 6.1 shows a SEM picture of a typical sample I made for the experiments. It was fabricated using the three level e-beam lithography technique described in Chapter 4. Each sample has four Ohmic contacts connected to four reservoirs labeled

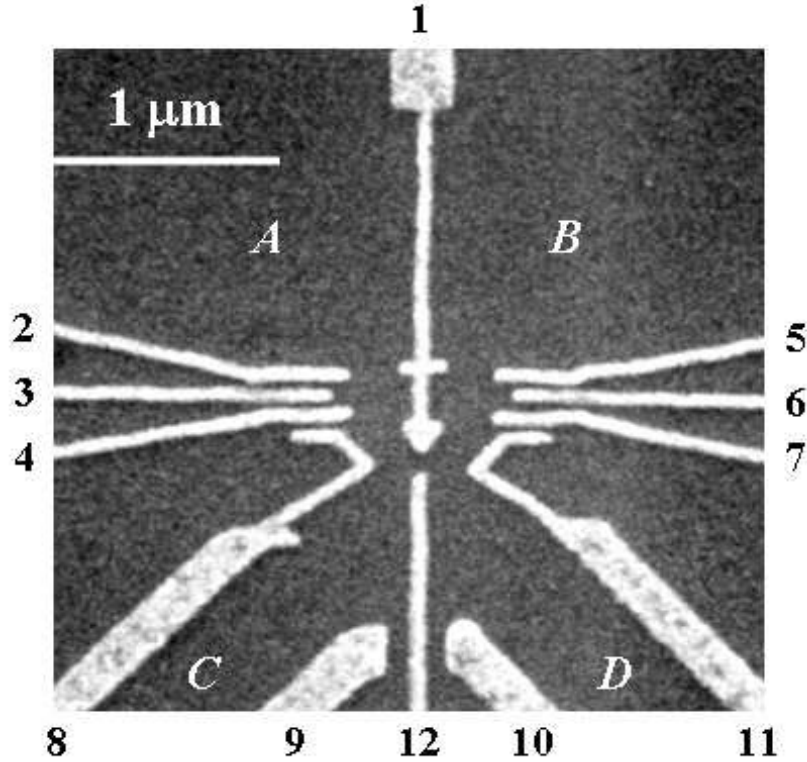


Figure 6.1: SEM picture of a sample used in the entanglement experiment.

as  $A$ ,  $B$ ,  $C$  and  $D$ , and twelve metallic gates shown as numbered bright patterns. Applying negative voltages to gates 1, 2, 3, and 4 (gates 1, 5, 6, and 7) defines quantum dot 1 (dot 2). The point contact formed by gate 1 and 12 serves as a beam splitter whose transmission probability  $T_j$  is controlled by a voltage on gate 12. The negative voltage on gate 1, also denoted as the spin exchange gate, changes both the height and width of the tunnelling barrier between the two dots and controls the strength of the exchange interaction (see Eq. 3.2). Gates 8, 9, 10 and 11 were designed to change the width of the outgoing channels leading to the shot noise detectors but were not used in the experiment reported here.

The theoretical proposal discussed in Chapter 3 assumed that each quantum dot contains only one electron and that the two electrons can be controlled very well by adjusting the quantum dot settings. However, these are formidable tasks for quantum dots in GaAs/AlGaAs heterostructures. The common picture of a quantum dot is that electrons occupy the eigenstates of a smooth confinement potential and they can be removed from the dot one by one as the voltage on the plunger gate decreases. In a real system, however, the confinement potential is always rough and irregular due to potential disorder and impurities. As the size of a dot is reduced, the roughness and irregularity become important and eventually all electrons left in the dot fall into the localized states formed by potential disorder and impurities. Given the random nature of these microscopic details, the electronic structure and, therefore, the transport properties of a dot in this regime are usually very complicated and unpredictable. For example, the well known Coulomb charge oscillation simply disappears when the number of electrons in a dot decreases to a certain value and tunneling through randomly distributing localized states dominates. Depending on the sample quality, this value varies from a few to a few tens. As a result, the control of electrons in such a dot becomes very difficult.

Creating quantum dots with a few or even one electron has been a goal in the mesoscopic community for a long time. Very recently a few groups have claimed the capability of creating single electron quantum dots [35, 36]. Their technique employs a set of auxiliary gates as detectors. This is not a plausible solution for my experiment since the two quantum dots are required to be very close to each

other, so no space is available for more gates. The best we can do here is to make the quantum dots as small as possible. However, as discussed in Chapter 3, it is expected that quantum dots with a few electrons can still be used for generating entangled states.

Although the two quantum dots are designed to be identical and are actually quite similar lithographically, I do not expect to be able to produce two microscopically identical quantum dots. Due to the random potential fluctuations, the confinement profile for the two dots could be quite different, making the electronic structure of each of the dots different. Therefore in a real coupled quantum dot system one may get two quantum dots having different number of electrons and different electronic structure. The work by Hu *et al.* [96, 97] addressed some of these issues, but further work, including data on real systems, is needed to see how they affect the entanglement.

The system is set up in the following way. Gates 1 and 12 are both biased with large negative voltages so there is no conduction between contacts  $A$  and  $B$ . The voltage on gate 1 is then lowered until the resistance between  $A$  and  $B$  decreases to about  $100\text{ M}\Omega$  (the reason will be given shortly). At this time gate 12 still has a large negative voltage, so the conduction between  $A$  and  $B$  should occur underneath gate 1. On the other hand, the tunneling probability is exponentially dependent on the gate width, so the conductance should only be associated with the narrow part of gate 1. I then apply voltage to gates 3 and 6 so that the two channels formed by 1 & 3 and 1 & 6 have a resistance of the order of  $13\text{ k}\Omega$ . Under this condition both

channels have a width of about half the Fermi wavelength. Gates 2, 4, 5 and 7 are then energized to form the two dots. We raise the voltage on these gates iteratively so that each time the change made on one gate increases the resistance of the dot by a small amount. In this way dots with two symmetric point contacts are obtained.

Needless to say setting the voltages on each of the gates that form the sample is somewhat tedious. A voltage applied to one gate can produce small but measurable changes in the transport characteristics of nearby gates. Each time a change is made, one has to wait for some time for the transient effects of depletion to settle down. I found that sometimes it took more than a week to set up one stable coupled quantum dot sample.

A few things need to be clarified in the sample set-up procedure. The potential barrier formed by the exchange gate determines the strength of exchange interaction between electrons in the two dots. Since this interaction decays exponentially as the height and width of the barrier increase [96], we do not want to fabricate a sample with a very wide exchange gate or put a very negative voltage on it. On the other hand, if the exchange barrier is too low, the tunnelling probability between the two dots will be too high, and then the two dots become a “molecule”, which is not a favored state for generating entanglement, according to Hu *et al.* [97]. I set the exchange gate so that its resistance is about 100 times larger than that of the two dots to reduce the inter-dot tunnelling. Normally, I set the dots with a resistance of the order of 1 M $\Omega$ , so the resistance between the two dots is about 100 M $\Omega$ . By reducing the channel width between gates 1 and 2 and 1 and 6 to half the Fermi

wavelength, we can make two small quantum dots very close to each other. This helps increase the exchange interaction strength.

The magnitude of the entanglement signal depends not only on the exchange interaction strength but also on the interaction time  $\tau$  between the two electrons. For very small quantum dots, the Coulomb charging energy is of the order of meV, much higher than the thermal energy ( $\sim 6\mu eV$ ) and bias across the dots ( $\sim 100\mu eV$ ), so they should be in the single electron tunnelling regime. In this regime the average time between two consecutive electrons is  $\tau_I = e/I$  ( $I$  is the dc current), so  $\tau_I$  is an upper bound of the actual exchange interaction time  $\tau$ . In order to have a large  $\tau$ , a small current should be used. In our measurements, a current of 100pA has been used, corresponding to  $\tau_I \sim 1$  nsec, and thus  $\tau < 1$  nsec. Without modeling the system, it is impossible to determine what interaction time is required. Experimentally, the smallest current we can use is set by the shot noise measurement sensitivity. In our system, a noise signal as small as  $5 \times 10^{-30}$  A<sup>2</sup>/Hz can be detected, corresponding to the full shot noise of  $I = 16$  pA.

Another important issue is the bias direction. For this experiment electrons have to be injected from reservoirs  $A$  and  $B$  to the two dots and tunnel to  $C$  and  $D$ . We want to make sure that the Fermi energy of  $A$  and  $B$  is always higher than that of  $C$  and  $D$ . This sounds trivial, however, given that the bias across the dots is only  $100 \mu eV$ , any thermal electromotive force in the wiring can change it significantly. Care must be taken during wiring and set-up to avoid or minimize such stray dc voltages. The static current in the system is monitored at all times.

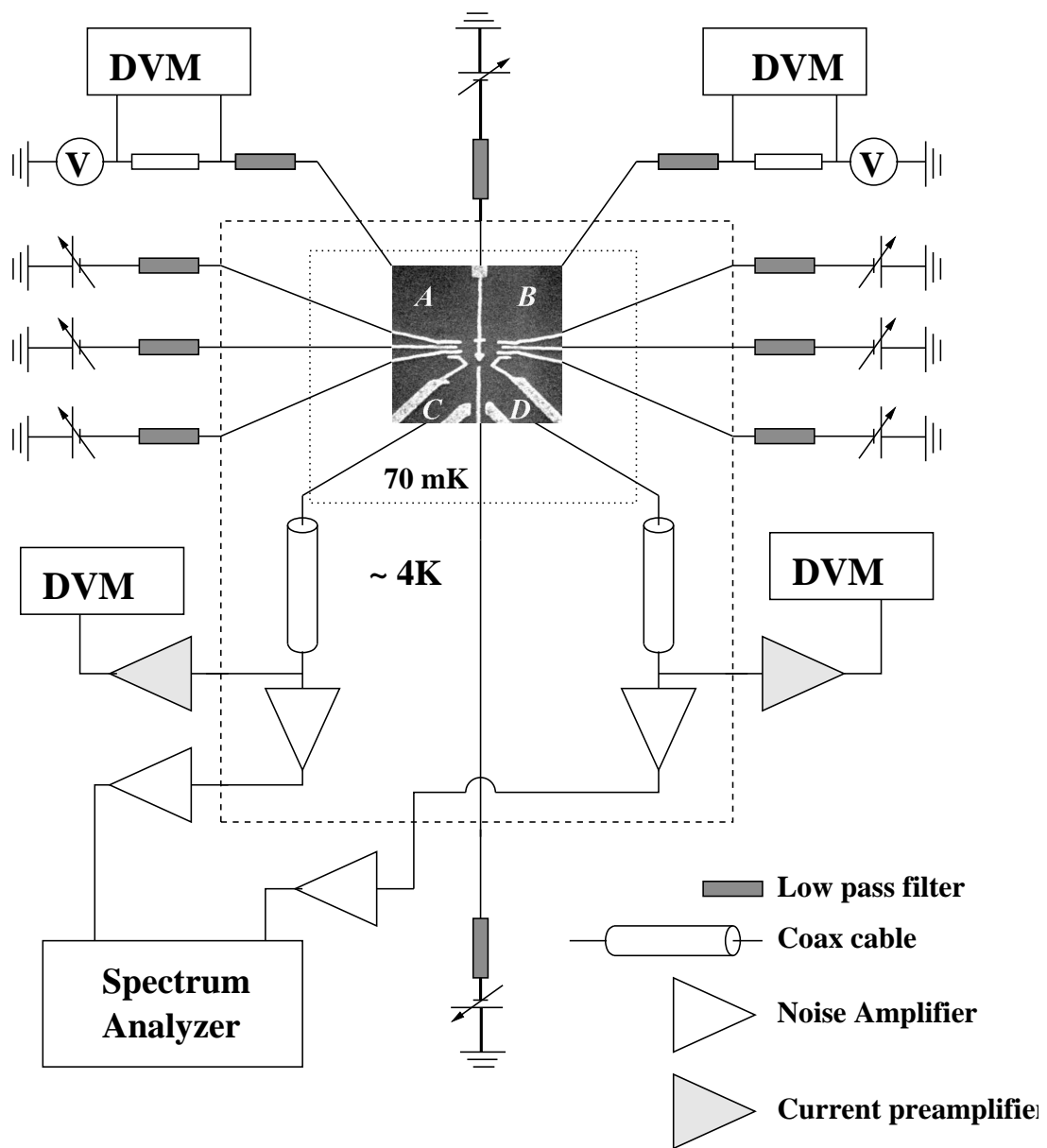


Figure 6.2: Experimental arrangement for the entanglement experiment.

Figure 6.2 shows the experimental arrangement. The sample is kept in the sample cell of a top-loading dilution refrigerator (see Chapter 4) with a base temperature of 70 mK. Eight gates used in this experiment are connected to independent batteries, each channel having a low pass filter to reduce the noise coupling from the environment. Two source reservoirs,  $A$  and  $B$ , are independently biased, and the voltages on two bias resistors are monitored by digital voltage meters, from which the injected dc currents are obtained. The two drain reservoirs,  $C$  and  $D$ , are connected to two short coax cables. In each channel, the current coming out of the sample is fed to two amplifiers. One is a room temperature current preamplifier that measures the dc current, while the other one is a cryogenic amplifier (see Chapter 4 for details), which is ac coupled to the sample and measures the high frequency components of the current, namely the current noise signal. The noise signals from both channels are further amplified at room temperature and then fed into an Agilent spectrum analyzer, which calculates the noise power of both channels and their cross correlation.

In a real system we not only have the wanted noise signal but also all kinds of other noise sources, such as low frequency noise and thermal noise. Low frequency noise can come from the sample and amplifiers. The frequency range where this noise is negligible depends on temperature, current level, and device specifications. In this experiment, the samples and noise amplifiers were kept at very low temperatures and the current was always below 1 nA. Additionally MESFETs with very good low frequency noise specifications were used to build the noise amplifiers and

measurements were done at a relatively high frequency (210-230 kHz). All these efforts helped reduce the importance of low frequency noise. As a result, in our measurements the low frequency noise is always negligible.

Any dissipative electrical component at a finite temperature contributes thermal noise. In this experiment the thermal noise from the cryogenic amplifiers dominates, as will be shown. Besides these two intrinsic noise sources, there will also be noise produced by external interference. Interference is coupled to the system by means of radiation, conduction, etc. Careful shielding and grounding can eliminate most interference problems.

The measurement system I used is shown schematically in Fig. 6.2. The noise amplifiers measure the shot noise and thermal noise from the sample and contribute their own thermal noise. In order to extract useful information a noise model needs to be developed.

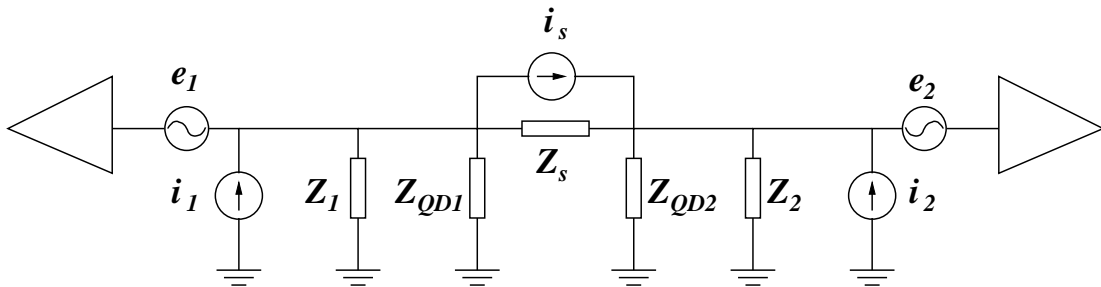


Figure 6.3: Noise model of the system.

Figure 6.3 shows a simplified noise model of the system, including the sample and the two cryogenic amplifiers.  $e_i$ ,  $i_i$  and  $Z_i$  ( $i = 1, 2$ ) are the voltage noise sources,

current noise sources and the load impedance of the two amplifiers.  $Z_{QDi}$  ( $i = 1, 2$ ) are the impedances of the two quantum dots.  $Z_s$  and  $i_s$  are the impedance and the noise associated with the part of the sample between reservoirs  $C$  and  $D$  in Fig. 6.1. In principle the two dots also contribute thermal noise. However, due to their high impedance ( $Z_{QD} \sim 1\text{M}\Omega$ ), the thermal noise current ( $\propto 4k_B T/Z_{QD}$ ) from them is very small compared to that of the beam splitter ( $\propto 4k_B T/Z_{BS}$  where  $Z_{BS} \ll Z_{QD}$ ), so it can be ignored. In the following, I assume that the two sides of the system are symmetric, so the subindexes 1 and 2 will be dropped. According to the noise model of MESFETs discussed in Chapter 4, the correlation between  $e$  and  $i$  can be neglected. Within this model, the noise measured by each amplifier and the cross spectrum can be calculated as:

$$S_1 = S_2 = e^2 + i^2 \left( \left| \frac{Z(Z + Z_s)}{2Z + Z_s} \right|^2 + \left| \frac{Z^2}{Z_s + 2Z} \right|^2 \right) + i_s^2 \left| \frac{Z_s Z}{Z_s + 2Z} \right|^2, \quad (6.1)$$

$$S_{12} = 2i^2 \text{Re} \left[ \frac{Z(Z + Z_s)}{Z_s + 2Z} \left( \frac{Z^2}{Z_s + 2Z} \right)^* \right] - i_s^2 \left| \frac{Z Z_s}{2Z + Z_s} \right|^2. \quad (6.2)$$

For  $S_1$  and  $S_2$  the  $e^2$  term dominates. The two cryogenic amplifiers have an equivalent input voltage noise of  $6 \times 10^{-19} \text{ V}^2/\text{Hz}$ . The other two terms in  $S_1$  and  $S_2$  are about tens times smaller for realistic component parameters. On the other hand, the shot noise signal to be detected is of the order of  $4 \times 10^{-21} \text{ V}^2/\text{Hz}$  (it is converted to these units for comparison), about 1% of the total background.

The cross-spectrum of the two channels can eliminate the huge background contributed by the two cryogenic amplifiers. Therefore the signal to noise ratio in

the cross-spectrum is much higher. In general, the cross-spectrum of two signals is a complex quantity. The physical meaning is that the average phase angle between the two signals needs not to be an integer multiple of  $\pi$ . In this model, however,  $S_{12}$  is always a real number according to equation 6.2. I verified this experimentally, and found the imaginary part of  $S_{12}$  is always around zero.

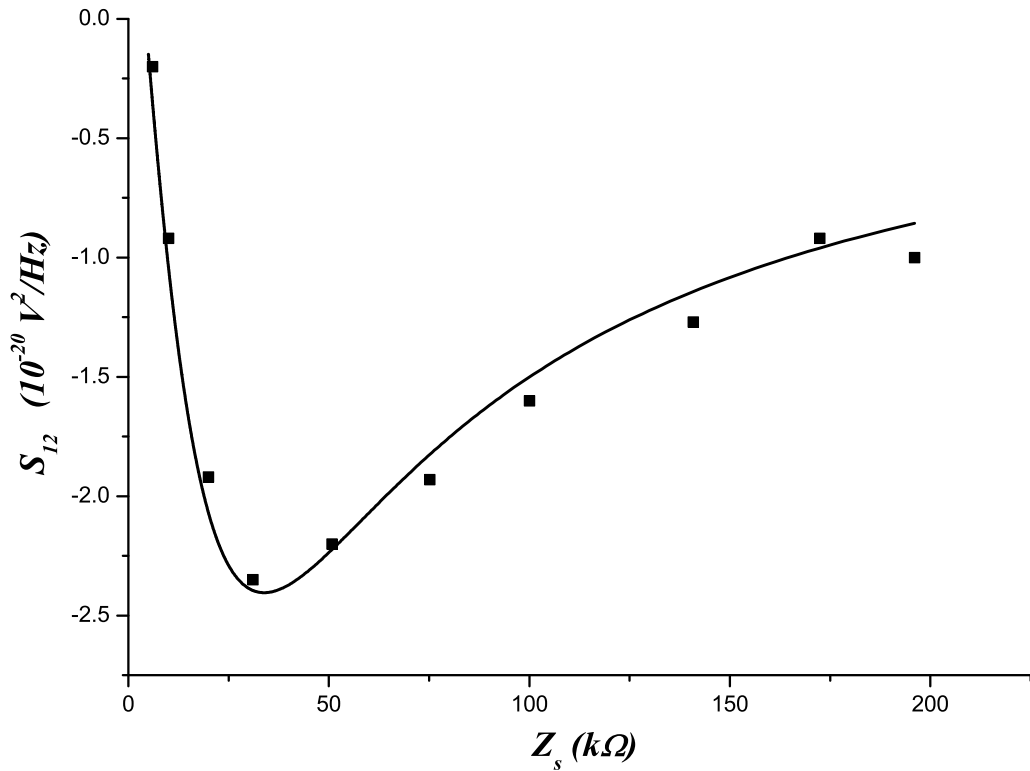


Figure 6.4: Background noise of the system.

$S_{12}$  is a function of both  $i^2$  and  $i_s^2$ . Note that  $i^2$  contains two parts, one being caused by the equivalent input current noise source of the MESFETs and the other due to one being the thermal noise from the load impedance. According to

the discussion in Chapter 4, the first part can be neglected. The second part is  $4k_B T/\text{Re}(Z)$ . For the equilibrium case (no current anywhere),  $i_s^2 = 4k_B T/\text{Re}(Z_s)$ . The solid line in figure 6.4 shows a calculation based on equation 6.2 with parameters from the experimental system. Dots in the same figure are the measured background noise. This background noise must be subtracted from the total noise measured for the entanglement experiment.

## 6.2 Experimental data

In this section, I discuss the first results for the shot noise measurements of two coupled quantum dots. The data shows both exchange gate and beam splitter dependence, which agrees qualitatively with the entanglement theory discussed in Chapter 3. Discrepancies between the data and the theory will also be addressed in this section.

The typical cross-spectrum data after a background subtraction from our sample as a function of beam splitter voltage in 2 mV steps is shown in Fig. 6.5. The four traces correspond to different exchange gate voltages  $V_{ex}$ . At each beam splitter voltage  $V_{BS}$  two data points are taken, one with  $I_{dc} = 100$  pA and the other with  $I_{dc} = 0$  A. For each data point the spectrum analyzer averages 40,000 times and integrates to obtain the total noise power over a 20 kHz window around 220 kHz. The zero current data is subtracted from the finite current data. For the two intermediate exchange gate voltages,  $V_{ex} = -184$  mV and  $-181$  mV, the cross spectrum exhibits a pronounced negative spike in the vicinity of  $V_{BS} = -181$  mV

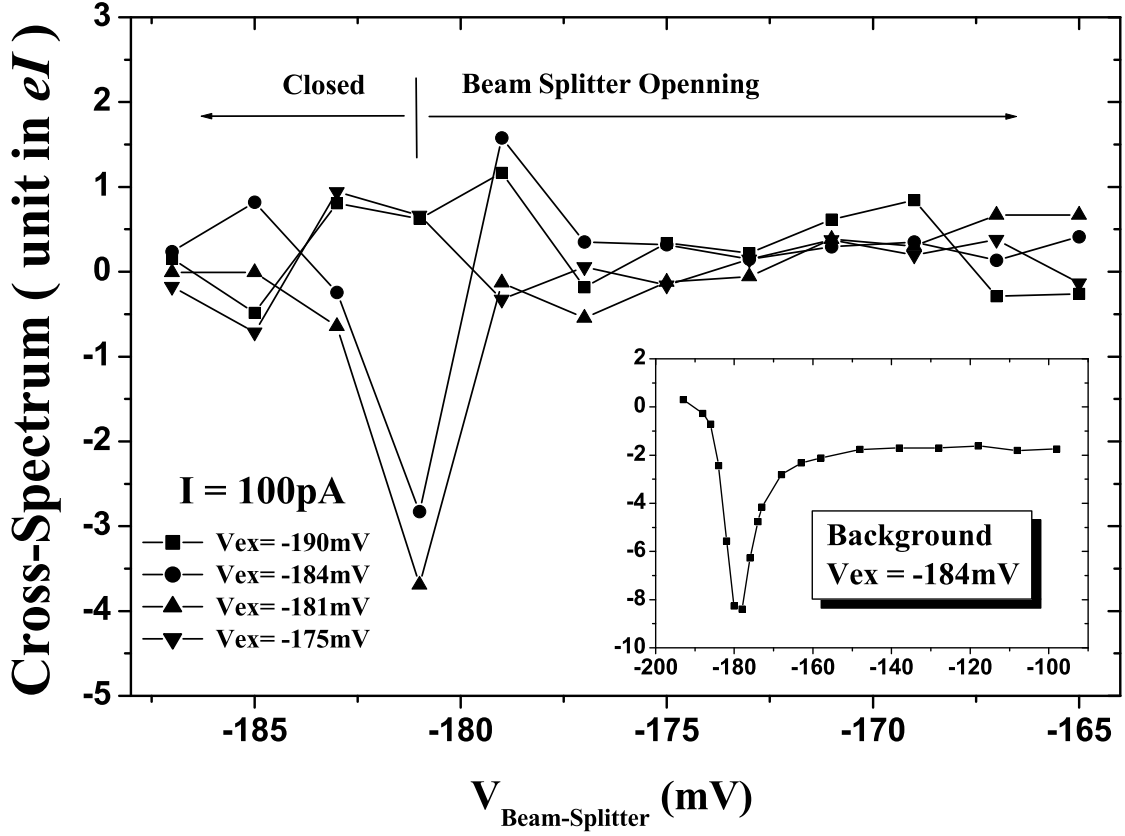


Figure 6.5: Typical cross-spectrum data after background subtraction; inset: background noise.

that corresponds to  $(-3 \pm 1)eI$  shot noise. At both higher and lower  $V_{BS}$  the signal fluctuates about  $(0 \pm 1)eI$ . When  $V_{ex}$  is raised to  $-190$  mV or lowered to  $-175$  mV, no evidence for a strong negative signal is observed.

According to the theory discussed in Chapter 3, the cross spectrum of an entanglement signal has the form  $-4eIT_j(1 - T_j)$ , with  $T_j$  being the transmission coefficient of the beam splitter. This form has a minimum when  $T_j = 1/2$ , corresponding to a beam splitter resistance of  $26$  k $\Omega$ . An independent transport mea-

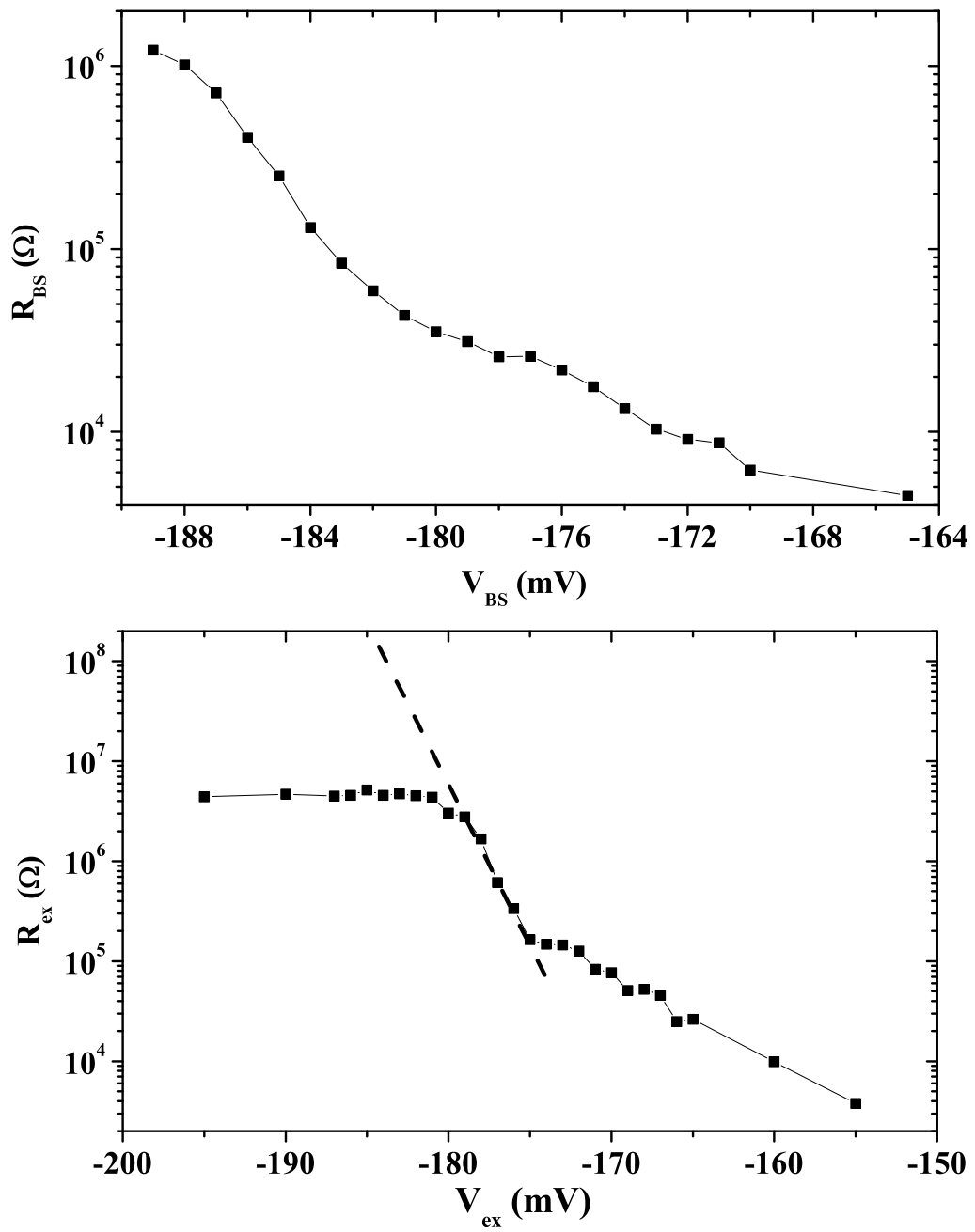


Figure 6.6: Beam splitter resistance and exchange gate resistance.

surement is carried out to find out the beam splitter resistance, as shown in Fig. 6.6. At  $V_{BS} = -181$  mV where the minimum cross spectrum occurs in Fig. 6.5, the beam splitter has a resistance of  $40$  k $\Omega$ . However, this number is actually the sum of the beam splitter resistance, the 2DEG resistance, and the contact resistance. The contribution of the last two terms is about  $4$  k $\Omega$ . By taking this into account, the result is still  $36$  k $\Omega$ , about  $10$  k $\Omega$  higher than expected. This discrepancy can be explained by two facts: first, the resistance measurements were done after the voltages on some of the gates forming the quantum dots were turned off and this may affect the transport properties of the beam splitter; second, as shown in Fig. 6.6, the beam splitter resistance is very sensitive to  $V_{BS}$ , so it can be a function of time if the beam splitter has any sort of instability.

The tunneling resistance under the exchange gate is also measured, as shown in Fig. 6.6. The data shows a saturation below  $V_{ex} = -180$  mV. This is due to the distributive capacitance of the dilution refrigerator wiring. The capacitance between the two leads used for resistance measurement is about  $1$  nF. The resistance measurement is done with a lock in technique with a reference frequency of  $25$  Hz. At this frequency,  $1$  nF corresponds to  $6$  M $\Omega$ , which is consistent with the resistance measurement. For  $V_{ex} = -181$  mV and  $-184$  mV, where the cross spectrum in Fig. 6.5 shows  $V_{BS}$  dependence, the exchange gate has an resistance between  $20$  M $\Omega$  and  $100$  M $\Omega$ , according to the extrapolation curve shown in Fig. 6.6. At  $V_{ex} = -175$  mV the exchange gate resistance between the two dots is only of the order of  $175$  k $\Omega$ ,  $3$  times smaller than the tunnelling resistance out of the dots. Direct

tunnelling between the two dots becomes significant and the system begins to behave as one quantum dot. In this case it has been predicted theoretically that electron spin entanglement cannot be detected by a beam-splitter arrangement [97]. In the opposite limit of very large exchange gate voltages the potential barrier between the two dots is much higher and the strength of the exchange interaction should be greatly reduced. We estimate that at  $V_{ex} = -190$  mV the tunnelling resistance between the two dots is greater than  $1 \text{ G}\Omega$  and the separation between the centers of the dots has increased to more than 70 nm. In such a case, the two dots are nearly decoupled and the electrons coming out of them are independent of one another so no entanglement should be possible.

The inset of Fig. 6.5 shows the typical background ( $I_{dc}=0$ ) at  $V_{ex} = -184$  mV as a function of  $V_{BS}$ . The shape and magnitude of this curve are insensitive to  $V_{ex}$  because the main contribution to this background is the thermal noise of the part of the sample between reservoirs C and D in Fig. 6.1, as discussed in the previous section. The minimum background occurs around -178 mV (not -181 mV) as expected from our noise circuit model. According to Fig. 6.4 a minimum background should occur at  $Z_s \approx 30k\Omega$ . In Fig. 6.6, that corresponds to -178 mV. Notice that the fluctuations in the background are very small and therefore it is very unlikely that the measured cross spectrum minimum in Fig. 6.5 is an artifact.

As a check of the reproducibility and our ability to set up the sample, I removed all the voltages on the gates and warmed up to well above 4.2 K. After cooling the sample back to 70 mK and applying voltages to the gates, I repeated the mea-

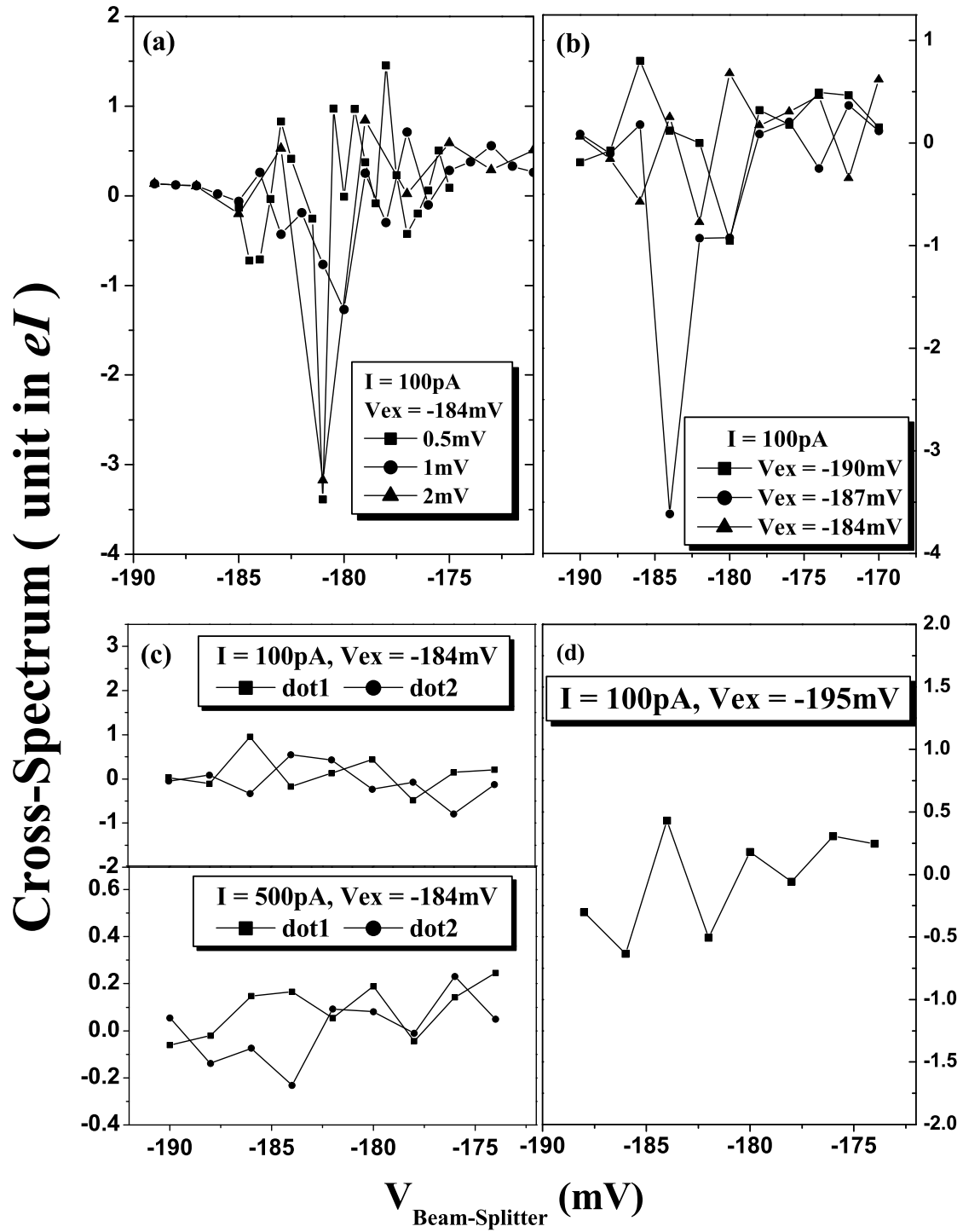


Figure 6.7: (a) & (b) Reproducibility check with three different step sizes in the beam splitter voltage; (c) single dot partition noise at different current level; (d) cross-spectrum for decoupled quantum dots.

measurements shown in Fig. 6.5 with different  $V_{BS}$  steps. Figure 6.7 displays three measurements of our cross-spectrum data for  $V_{BS}$  steps of 0.5, 1, and 2 mV taken at  $V_{ex} = -184$  mV. For unknown reasons, at a voltage step size of 1 mV I found less reproducibility than at other voltages but at all values I found a maximum negative cross-spectrum of  $-eI$  to  $-3eI$  at nearly the same value of  $V_{BS}$  and in agreement with my earlier measurements. This data also allows me to test the  $T(1 - T)$  theoretical dependence of the entanglement signal. From measurements of the beam splitter resistance as a function of  $V_{BS}$ , I estimate that the half-width of the negative cross-spectrum dip should be approximately 2.5 mV centered about  $V_{BS} = -182$  mV. The actual data appears to be a factor of 2 narrower than computed. This may simply suggest less than perfect operation of the beam splitter.

Figure 6.7(b) shows another measurement after the sample experienced a complete thermal cycle (warmed up to room temperature). Again, this data repeats all important features of the previous data with only a minor shift in the  $V_{ex}$  and  $V_{BS}$  dependence.

The  $V_{ex}$  and  $V_{BS}$  dependence of the cross spectrum noise shown in figs. 6.5 and 6.7(a), (b) is qualitatively consistent with the theoretical predictions for entangled singlet electrons exiting our coupled quantum dots. However, there are a few serious issues to be addressed about these results.

The theoretically predicted magnitude of the maximum negative cross spectrum noise for entangled spin singlet states occurs when  $T_j = 0.5$  and has a value of  $-eI$ , but our total background subtracted noise is  $-3eI$ . Uncorrelated electrons

exiting the two dots can generate partition noise at the beam splitter, which also contributes to the total measured signal. However, this partition noise has the form  $-2eIT_j(1 - T_j)$  (see Chapter 3 for details), with a maximum value of  $-0.5eI$  for  $T_j = 0.5$ . As a result, a current with both entanglement and non-entanglement components should have a shot noise less than that of a current with full entanglement. In other words, the  $-3eI$  result cannot be explained by a presence of uncorrelated electrons.

We measured the partition noise when only one quantum dot was active at currents of 100 and 500 pA. As shown in Fig. 6.7(c), we found no more than  $-eI$ . At large exchange gate voltages, where we do not believe we have any strong spin exchange coupling between the dots, we have attempted to measure the uncorrelated partition noise from the double dot system and, as shown in Fig. 6.7(d), have not found any negative correlation greater than  $-eI$  and we have never found any positive correlation. We have not found any other possible contribution to our negative cross spectrum and are left with a signal that appears to be 2-3 times larger than theoretical expectations. We point out that the largest uncorrelated noise signal theoretically predicted [45, 53, 117] or experimentally observed [50, 51, 52] is at least a factor of 6 smaller than we have observed in this entanglement experiment, so the measured signal must be associated with intra-dot couplings.

Ideally, this entanglement experiment should be carried out for the case of single electron quantum dots, or at least for quantum dots with odd number of electrons, as discussed in Chapter 3. The numbers of electrons in two dots have three

different combinations: odd-odd, odd-even and even-even. The shot noise signal for entangled states should disappear for the last two cases. We estimate the number of electrons in each dot to be  $2\sim 8$  based on the depletion pattern and the carrier density in the 2DEG. However, as pointed out in the previous section, counting electrons down to a few in such small quantum dots is extremely difficult. In particular, the Coulomb charge oscillation becomes undetectable in this regime. As a result, we do not know the exact number of electrons in the dots at different gate voltages. Therefore it is impossible to demonstrate how the measured shot noise signal changes depending on the electronic configuration of the two dots. Nevertheless, by tuning the gate voltages away from the settings used in Fig. 6.5, we observed that the measured negative cross spectrum disappeared, indicating the intra-dot coupling is sensitive to the single dot settings.

Another curious feature is that for most of our data, the negative cross spectrum occurs at only one point, even when the data acquisition step size is reduced. Sometimes we do observe large fluctuations in the shot noise at a single point due to some type of sample instability. However, they usually happen when we use less average times on the spectrum analyzer and are not reproducible in size and gate voltages. We believe the signal observed is not due to random fluctuations. Further study of the properties of the beam splitter is required to fully understand the data.

### 6.3 Potential problems in the experiment

In this section, I will discuss some other aspects of the entanglement experiment. I will first talk about the problem of synchronizing electrons and then discuss the effect of Coulomb interaction on the entanglement.

The original proposal of electron spin entanglement discussed in Chapter 3 uses two coupled quantum dots as an entangler. It works in the following way: two electrons are placed in the quantum dots and interact with each other through spin exchange interaction; they are then moved out from the dots to the beam splitter where the quantum interference takes place. The underlying assumption is that one has full control of the quantum dots. The two electrons are forced to stay in the dots for the same amount of time, then they leave the dots and arrive at the beam splitter at the same time.

In a realistic system, however, the synchronization of the two electrons is very difficult to achieve. Manipulating single electrons with a set of complicated operations like those assumed by the original proposal of electron spin entanglement is still a big challenge, even with state-of-the-art nano-technology. In our arrangement, the electrons are controlled by electrical currents. They tunnel into and out of the two dots. Since the tunnelling is a random process, there is no control over the entering and leaving time, so even for two microscopically identical quantum dots, electrons are not necessarily synchronized. The Fermi velocity of electrons in the 2DEG is about  $10^7$  cm/sec (see Table 2.1 for details). Suppose two electrons exit the dots with a lag of 100 ps and travel ballistically afterwards. Then the distance

between them will be  $10 \mu\text{m}$ . From the particle point of view the two electrons may simply miss each other, so the expected quantum interference at the beam splitter may not happen at all. On the other hand, in the original proposal the electrons are assumed to tunnel out of the two dots as plane waves, so from the wave point of view the two electrons can still have interference at the beam splitter even if they exit the dots at different times, so long as the electron waves have an overlap in space. Strictly speaking electrons exiting the dots should be viewed as wave packets with a spatial width. The impact of this effect on the quantum interference at the beam splitter was theoretically studied by Blanter *et al.* [44] Their result shows that the magnitude of the interference signal decays exponentially as the time lag of the two wave packets increases, with a characteristic time (Typical values of this characteristic time are below 100 ps.) corresponding to  $\delta/v$  where  $\delta$  and  $v$  are the spatial width and group velocity of the wave packets respectively.

In principle, the problem can be solved by using an electron pump, or turnstile [118], to replace the static quantum dots used. The basic idea is to use fast gate operations to synchronize electron motion. In that way, electrons enter and leave the dots in a controlled manner instead of in a random process. In other words, electrons are “forced” to move by programmed gate operations. The turnstile devices have been studied experimentally and theoretically. Kouwenhoven *et al.* [118] have demonstrated a turnstile operation on a quantum dot fabricated in GaAs/AlGaAs heterostructures. Hu *et al.* [95] studied theoretically the difference between static quantum dots and turnstile devices and pointed out the latter is more suitable for the

entanglement experiment. However, achieving the high precision of timing required for the entanglement experiment may be a challenge. According to the analysis above, the timing should be better than 100 ps.

Fast gate operation by itself is an interesting topic, since high speed applications for new devices are always demanded. For the entanglement experiment this kind of operation should also be applied to the exchange gate, so the spin exchange interaction can be under control. Another interesting topic is the shot noise of a turnstile device. Once electrons are regulated by a periodic gate signal, the current will be composed of a series of single electron events almost equally spaced in time, so there should be little shot noise exhibited.

There are still other factors affecting the electron synchronization, even in turnstile devices. When two quantum dots are placed very close to each other, the Coulomb interaction between them is quite significant. To give an idea of the order of magnitude, in our sample the presence of an electron in one dot can shift the energy levels in the other dot by an amount of 1 meV. This shift can make the other dot unavailable for electrons. The closer the two dots are, the more severe this problem is. The extreme situation is at any time at most only one quantum dot is occupied. In this case there will be no entanglement.

The two dots coupled by strong Coulomb interaction can be viewed as two parallel tunneling paths modulating each other. As discussed in Chapter 5, shot noise measurements are a nice tool to study these fast modulation processes. One can measure the shot noise of one dot as a function of the status of the other dot.

If the modulation really exists, enhanced shot noise should be observed.

The shot noise of quantum dots is another important issue to be addressed. In the original proposal electrons are assumed to be synchronized so, as pointed out earlier in this section, the currents coming out of the two dots should have no fluctuation. In static quantum dots, however, due to the random tunnelling process, the exiting time of consecutive electrons does have fluctuations, which means that the quantum dots contribute shot noise. In general, this is a suppressed shot noise compared to the Poissonian value  $2eI$ . The exact Fano factor depends on the gate settings. When the dots are squeezed down to the regime of a few electrons, the localized states caused by potential fluctuations and impurities can change the shot noise of the dots drastically. Both enhanced and suppressed shot noise could appear, as shown in Chapter 5. The contribution of this extra shot noise to the cross spectrum becomes more complex when the current carrying it is partitioned at the beam splitter. Depending on the Fano factor of the two dots, this extra shot noise can generate both a positive (if  $F_{QD} > 1$ ) or a negative (if  $F_{QD} < 1$ ) cross-spectrum [44]. We indeed observed super enhanced shot noise for quantum dots. As a result, the cross-spectrum of the shot noise of the two dots becomes positive. This extra signal will be mixed with any entanglement related signal, thus in a static arrangement, without carefully characterizing the shot noise properties of the dots, it will be very difficult to extract any useful information.

The last issue I want to discuss in this section is the nature of the beam splitter. In a particle picture a beam splitter is just a tunnel barrier characterized

by its transmission coefficient  $T_j$ . This may change when electrons come in as waves. For instance, different part of the beam splitter could have different transmission coefficients. In the original proposal, electrons either tunnel through the beam splitter or get reflected, then they are absorbed by the reservoirs afterwards. In a realistic system, electrons, especially viewed as waves, can have multiple reflections. In addition, reservoirs can also inject electrons back to the beam splitter. All these extra factors can change the signal size, or even cause a qualitative change. To fully understand the beam splitter, a study of its behavior in a more controllable configuration is desirable.

To conclude, in this section, I discussed the difference between a synchronized (turnstile) and non-synchronized (static model) double dot system. The effect of Coulomb interaction between dots on the synchronization scheme was discussed briefly. Other complexities raised by the extra noise of quantum dots, by the wave nature of electrons, and by the imperfect operations of the beam splitter have been mentioned as well. Some future work and possible directions were discussed.

## 6.4 Summary

The creation of entangled electron spin states is very important for both potential device applications and basic research. Electron spins are proposed as qubit candidates for quantum computing. Since entanglement is essential for the superior power of quantum computers, the study of entanglement of electron spins becomes critical. Being one of the most mysterious properties in quantum systems, entan-

glement has attracted interest since Schrödinger's landmark 1935 response to EPR. Experimentally, scientists have created entangled photon states. The violation of Bell's inequality has been shown, in agreement with the predictions of quantum mechanics. Since entanglement is a universal property of quantum states, it should also manifest itself for other particles. However, no definitive experimental proof of entanglement for massive particles in a solid-state environment has been demonstrated yet.

In this chapter, I discussed the first experimental work on the shot noise of a coupled quantum dot system. This experiment has been proposed as a possible way to create and detect entangled electron spin states. Our data is in qualitative agreement with some aspects of the theory of entanglement discussed in Chapter 3. In particular, the measured negative cross spectrum shows both exchange gate and beam splitter voltage dependence, indicating that the signal is related to both intra-dot couplings and quantum interference effects at the beam splitter. A few possibilities which may also contribute to the signal have been excluded. However, a quantitative agreement is still lacking; the measured signal does not have the size and shape predicted by theory. At the very least, these results are encouraging for further investigation. Better characterization of the two dots and the beam splitter is required, and reproducibility on more samples is desired.

## Chapter 7

### Conclusion and future work

#### 7.1 Shot noise measurements

The main experimental techniques I used for this thesis is shot noise measurements. In order to detect the shot noise of the small current required for the entanglement experiment, I developed two low noise cryogenic amplifiers. When operated at low temperatures ( $\sim 4$  K), these amplifiers have a voltage noise of  $0.8 \text{ nV}/(\text{Hz})^{1/2}$  and negligible current noise. They work properly up to 1 MHz. Combined with the noise cross-correlation technique realized by an Agilent 89410A spectrum analyzer, these amplifiers can be used to measure the shot noise of a current as low as 20 pA in a reasonable amount of time for averaging (i.e., 1 hour). Quieter amplifiers can be achieved by making a better circuitry design and choosing devices with better performance. However, as discussed in Chapter 6, the shot noise signal to be detected is always accompanied by thermal noise from the sample, so the pursuit of ultra low noise amplifiers becomes less important at some point.

As far as the noise (any noise other than the shot noise to be detected) is concerned, the most serious problem in the measurement system was not the noise from the instruments but rather the instability in the samples and some long term drift in the background noise due to unknown causes. One typical form of the insta-

bility is shown in Fig. 5.6(d). It resembles random telegraph noise commonly seen in GaAs/AlGaAs heterostructures. Fortunately, this phenomenon does not occur very often, and can be “overcome” simply by discarding data with this problem. On the other hand, long term drift is a serious problem that needs to be solved to improve the experiment. As mentioned above, given the background contributed by the amplifier noise and the thermal noise of the sample, measuring the shot noise of a small current always requires considerable time averaging. For the entanglement experiment, obtaining a complete set of data may take a few days or even a few weeks, depending on the data resolution one asks for. As a result, the system is required to be very stable over the time of data acquisition. With the present setup this is impossible. The worst aspect is that long term drift appears to be random and cannot be well characterized. The lack of reproducibility of some experimental data is mainly caused by this drift. Its origin is still not very clear, although there are indications that it may be related to sample quality.

## 7.2 Shot noise in mesoscopic tunnel barriers

In this thesis, I have shown measurements of the shot noise in mesoscopic tunnel barriers. Besides the expected full shot noise for tunnel barriers, suppressed and enhanced shot noise were also observed. To my knowledge, this was the first time anyone has seen such deviations of the shot noise from the full value in tunnel barriers. In particular, a Fano factor of over 10 that I observed in some barriers was totally unexpected. In general, the measured shot noise is a complicated function of

the applied bias and gate voltages and varies from sample to sample. This resembles conductance measurements of mesoscopic conductors where the result is sample specific since the conductance is very sensitive to the microscopic details which vary from sample to sample. Thus the disagreement between the noise data and theory can be explained by the tunnel barriers being non-ideal. I have studied numerically the dependence of shot noise on the microscopic details of a tunnel barrier. The simulation results show that localized states induced by impurities and/or potential disorder can affect the shot noise significantly. For example, shot noise can be much enhanced if the current is composed of electrons tunnelling through interacting localized states. The simulations capture most of the important features presented by the experimental data and can be used to explain the data.

This work clearly indicates that shot noise of mesoscopic samples is generally much more complicated than what is expected from simple models. Many details of the transport processes in these sample can be revealed by shot noise detection. This will benefit both mesoscopic physics and potential device applications in the future.

Although the shot noise study of mesoscopic tunnel barriers reported in this thesis is more comprehensive compared to the existing results, a more systematic investigation is required to obtain a better understanding. For example, more results of the standard conductance measurement may be helpful for understanding the shot noise properties. Given the uncontrollable nature of the microscopic details (e.g., their existence, location and properties), it seems that there is not much that can

be done with them. However, one interesting direction is to study the shot noise of mesoscopic samples with fabricated “controllable” details. For example, a quantum dot resembles a localized state studied in section 5.3 in many aspects. As pointed out in Chapter 2, the shot noise of a quantum dot is still far from being well understood, especially in the linear transport regime ( $eV \leq k_B T$ ). Another example is that two electrostatically coupled quantum dots can be viewed as two interacting localized states, so some interesting effects on the shot noise of the two dots may be expected.

### 7.3 Quantum entanglement

In this thesis, I reported the first shot noise cross-spectrum evidence for entangled electron spin states in two coupled GaAs/AlGaAs quantum dots. Electrons are injected into two quantum dots that are separated by a tunnelling barrier exchange gate and allowed to exit onto a beam splitter. Cross-correlated shot noise was measured between the two exiting channels. A large negative cross-spectrum signal was observed as the transmission coefficient of the beam splitter is changed for only certain values of the spin exchange coupling constant. This provides compelling evidence that something related to intra-dot couplings was measured. I excluded some possible contributions to the expected negative signal from other sources. The experimental results are qualitatively consistent with most of the theoretical expectations for spin singlet entanglement in this double dot system.

Quantitatively the measured shot noise is not in good agreement with the theory. The size of the signal is larger than expected and the important beam

splitter transmission dependence has not been verified. More work should be done to characterize the system. For example, spectroscopy of the energy states in the two dots is desired for doing the experiment in a more controllable way. The exact nature of the beam splitter remains a problem which deserves further study. In Chapter 6 I also discussed other potential problems in the experiment. Nevertheless, the observation of the expected qualitative behavior of the shot noise in such a system gives us the confidence that we have the initial evidence of electron spin entanglement, although further work is required for a definitive demonstration.

The entanglement experiment belongs to a large class of experiments probing the quantum statistics by measuring shot noise, as pointed out in Chapter 1. This is another important aspect of this experiment, besides demonstrating the entanglement of electron spins. Measuring shot noise in multi-terminal conductors presents difficulties from both technical challenges and the lack of a clear physical picture. Technical challenges include reducing the disturbance of the noise detection apparatus on the transport process in the samples and reducing the cross-talk between the apparatus for different terminals. From the point of view of physical insight, the shot noise properties of multi-terminal conductors are not well understood even theoretically yet. Needless to say, there are very few experimental results available at this time. In general, this is an interesting and important direction in the study of mesoscopic systems. The work reported in this thesis contributes to the understanding of both aspects mentioned above.

## BIBLIOGRAPHY

- [1] M. Nielsen and I. Chuang. *Quantum computation and quantum information*. Cambridge University Press, Cambridge, 2000.
- [2] J. I. Cirac and P. Zolle. Quantum computations with cold trapped ions. *Phys. Rev. Lett.*, 74:4091–4094, 1995.
- [3] R. C. Ramos, M. A. Gubrud, A. J. Berkley, J. R. Anderson, C. J. Lobb, and F. C. Wellstood. Design for effective thermalization of junctions for quantum coherence. *IEEE Trans. on Appl. Supercond.*, 11:998, 2001.
- [4] D. Loss and D. P. DiVincenzo. Quantum computation with quantum dots. *Phys. Rev. A*, 57:120, 1998.
- [5] G. Burkard, D. Loss, and D. P. DiVincenzo. Coupled quantum dots as quantum gates. *Phys. Rev. B*, 59:2070, 1999.
- [6] B. E. Kane. A silicon-based nuclear spin quantum computer. *Nature*, 393:133, 1998.
- [7] P. W. Shor. Algorithms for quantum computation: discrete logarithms and factoring. *Proc. 35<sup>th</sup> Annual Symposium on Foundations of Computer Science*, IEEE Computer Society Press, pages 124–134, 1994.
- [8] L. K. Grover. Quantum computers can search arbitrarily large databases by a single query. *Phys. Rev. Lett.*, 79:4709–4712, 1997.

- [9] R. Feynman. *Int. J. Theor. Phys.*, 21:467, 1982.
- [10] D. Deutsch. Quantum theory, the church-turing principle and universal quantum computer. *Proc. Phys. Soc. London*, 400:97, 1985.
- [11] Y. Makhlin, G. Schön, and A. Shnirman. Quantum-state engineering with Josephson-junction devices. *Rev. Mod. Phys.*, 73:357, 2001.
- [12] A. Shnirman, G. Schön, and Z. Hermon. Quantum manipulation of small Josephson junctions. *Phys. Rev. Lett.*, 79:2371–2374, 1997.
- [13] D. V. Averin. Adiabatic quantum computation with Cooper pairs. *Solid State Commun.*, 105:659–664, 1998.
- [14] M. F. Bokco, A. M. Herr, and M. J. Feldman. Prospects for quantum coherent computation using superconducting electronics. *IEEE Trans. Appl. Super.*, 7:3638–3641, 1997.
- [15] A. J. Leggett. Dynamics of the dissipative two-state system. *Rev. Mod. Phys.*, 59:1–85, 1987.
- [16] D. Vion, A. Aassime, A. Cottet, P. Joyez, H. Pothier, C. Urbina, D. Esteve, and M. H. Devoret. Manipulating the quantum state of an electrical circuit. *Science*, 296:886–889, 2002.
- [17] Yang Yu, Siyuan Han, Xi Chu, Shih-I Chu, and Zhen Wang. Coherent temporal oscillations of macroscopic quantum states in a Josephson junction. *Science*, 296:889–892, 2002.

- [18] Y. Nakamura, Y. A. Pashkin, and J. S. Tsai. Coherent control of macroscopic quantum states in a single-Cooper-pair box. *Nature*, 398:786, 1999.
- [19] J. R. Friedman, V. Patel, W. Chen, S. K. Tolpygo, and J. E. Lukens. Quantum superposition of distinct macroscopic states. *Nature*, 406:43, 2000.
- [20] Caspar H. van der Wal, A. C. J. ter Haar, F. K. Wilhelm, R. N. Schouten, C. J. P. M. Harmans, T. P. Orlando, Seth Lloyd, and J. E. Mooij. Quantum superposition of macroscopic persistent-current states. *Science*, 290:773, 2000.
- [21] J. M. Martinis, S. Nam, and J. Aumentado. Rabi oscillations in a large Josephson-junction qubit. *Phys. Rev. Lett.*, 89:117901, 2002.
- [22] P. Joyez, P. Lafarge, A. Filipe, D. Esteve, and M. H. Devoret. Observation of parity-induced suppression of Josephson tunneling in the superconducting single electron transistor. *Phys. Rev. Lett*, 72:2458–2461, 1994.
- [23] D. Flees, S. Han, and J. Lukens. Interband transitions and band gap measurements in Bloch transistors. *Phys. Rev. Lett.*, 78:4817–4820, 1997.
- [24] Y. Nakamura, C. D. Chen, and J. S. Tsai. Spectroscopy of energy-level splitting between two macroscopic quantum states of charge coherently superposed by Josephson coupling. *Phys. Rev. Lett.*, 79:2328–2331, 1997.
- [25] A. Einstein, B. Podolsky, and N. Rosen. Can quantum-mechanical description of physical reality be considered complete? *Phys. Rev.*, 47:777, 1935.
- [26] J. Bell. On the Einstein-Podolsky-Rosen paradox. *Physics*, 1:195–200, 1964.

- [27] J. Bell. On the problem of hidden variables in quantum mechanics. *Rev. Mod. Phys.*, 38:447–452, 1966.
- [28] S. J. Freedman and J. F. Clauser. Experimental test of local hidden-variable theories. *Phys. Rev. Lett.*, 28:938–941, 1972.
- [29] A. Aspect, J. Dalibard, and G. Roger. Experimental test of Bell’s inequalities using time-varying analyzers. *Phys. Rev. Lett.*, 49:1804–1808, 1982.
- [30] W. Tittel, J. Brendel, H. Zbinden, and N. Gisin. Violation of Bell inequalities by photons more than 10 km apart. *Phys. Rev. Lett.*, 81:3563, 1998.
- [31] G. Weihs, T. Jennewein, C. Simon, H. Weinfurter, and A. Zeilinger. Violation of Bell’s inequality under strict einstein locality conditions. *Phys. Rev. Lett.*, 81:5039, 1998.
- [32] Y. A. Pashkin, T. Yamamoto, O. Astafiev, Y. Nakamura, D. V. Averin, and J. S. Tsai. Quantum oscillations in two coupled charge qubits. *Nature*, 421:823–826, 2003.
- [33] A. J. Berkley, H. Xu, R. C. Ramos, M. A. Gubrud, F. W. Strauch, P. R. Johnson, J. R. Anderson, A. J. Dragt, C. J. Lobb, and F. C. Wellstood. Entangled macroscopic quantum states in two superconducting qubits. *Science*, 300:1548, 2003.

- [34] T. Yamamoto, Y. A. Pashkin, O. Astafiev, Y. Nakamura, and J. S. Tsai. Demonstration of conditional gate operation using superconducting charge qubits. *Nature*, 425:941, 2003.
- [35] M. Ciorga, A. S. Sachrajda, P. Hawrylak, C. Gould, P. Zawadzki, S. Julian, Y. Feng, and Z. Wasilewski. Addition spectrum of a lateral dot from Coulomb and spin-blockade spectroscopy. *Phys. Rev. B (Rapid Communication)*, 61:R16315, 2000.
- [36] J. R. Petta, A. C. Johnson, C. M. Marcus, M. P. Hanson, and A. C. Gossard. Manipulation of a single charge in a double quantum dot. *Phys. Rev. Lett.*, 93:186802, 2004.
- [37] M. J. M. de Jong and C. W. Beenakker. Doubled shot noise in disordered normal-metal-superconductor junctions. *Phys. Rev. B*, 49:16070, 1994.
- [38] V. A. Khlus. *Zh. Eksp. Teor. Fiz.*, 93:2179, 1987.
- [39] R. B. Laughlin. Anomalous quantum hall effect: An incompressible quantum fluid with fractionally charged excitations. *Phys. Rev. Lett.*, 50:1395–1398, 1983.
- [40] C. L. Kane and M. P. A. Fisher. Nonequilibrium noise and fractional charge in the quantum Hall effect. *Phys. Rev. Lett.*, 72:724, 1994.

- [41] X. Jehl, P. Payet-Burin, C. Baraduc, R. Calemczuk, and M. Sanquer. Andreev reflection enhanced shot noise in mesoscopic SNS junctions. *Phys. Rev. Lett.*, 83:1660, 1999.
- [42] L. Saminadayar, D. C. Glattli, Y. Jin, and B. Etienne. Observation of the  $e/3$  fractionally charged Laughlin quasiparticle. *Phys. Rev. Lett.*, 79:2526, 1997.
- [43] R. de Picciotto, M. Reznikov, M. Heiblum, V. Umansky, G. Bunin, and D. Mahalu. Direct observation of a fractional charge. *Nature*, 389:162, 1997.
- [44] Ya. M. Blanter and M. Büttiker. Shot noise in mesoscopic conductors. *Phys. Rep.*, 336:1, 2000.
- [45] M. Büttiker. Scattering theory of thermal and excess noise in open conductors. *Phys. Rev. Lett.*, 65:2901, 1990.
- [46] L. S. Levitov and G. B. Lesovik. *JETP Lett*, 58:230, 1993.
- [47] G. Iannaccone, G. Lombardi, M. Macucci, and B. Pellegrini. Enhanced shot noise in resonant tunneling: Theory and experiment. *Phys. Rev. Lett.*, 80:1054, 1998.
- [48] Ya. M. Blanter and M. Büttiker. Transition from sub-poissonian to super-poissonian shot noise in resonant quantum wells. *Phys. Rev. B*, 59:10217, 1999.
- [49] M. Büttiker. Electron statistical effects: bunches of photons–antibunches of electrons. *Science*, 284:275–276, 1999.

- [50] M. Henny, S. Oberholzer, C. Strunk, T. Heinzel, K. Ensslin, M. Holland, and C. Schönberger. The Fermionic Hanbury Brown and Twiss experiment. *Science*, 284:296, 1999.
- [51] W. D. Oliver, J. Kim, R. C. Liu, and Y. Yamamoto. Hanbury Brown and Twiss-Type experiment with electrons. *Science*, 284:299, 1999.
- [52] R. C. Liu, B. Odom, Y. Yamamoto, and S. Tarucha. Quantum interference in electron collision. *Nature*, 391:263, 1998.
- [53] G. Burkard, D. Loss, and E. V. Sukhorukov. Noise of entangled electrons: Bunching and antibunching. *Phys. Rev. B*, 61:R16303, 2000.
- [54] C. M. Lieber. Nanoscale science and technology: Building a big future from small things. *MRS Bull.*, 28:486–491, 2003.
- [55] T. Ando, A. B. Fowler, and F. Stern. Electronic properties of two-dimensional systems. *Rev. Mod. Phys.*, 54:437–672, 1982.
- [56] C. W. J. Beenakker and H. van Houton. Quantum transport in semiconductor nanostructures. *Solid State Physics*, 44:1–228, 1991.
- [57] N. W. Ashcroft and N. D. Mermin. *Solid state physics*. Saunders College Publishing, 1976.
- [58] S. Datta. *Quantum Phenomena*. Menlo Park. CA: Addison-Wesley, 1989.
- [59] H. Z. Zheng, H. P. Wei, and D. C. Tsui. Gate-controlled transport in narrow GaAs/Al<sub>x</sub>Ga<sub>1-x</sub>As heterostructures. *Phys. Rev. B*, 34:5635–5638, 1986.

- [60] T. J. Thornton, M. Pepper, H. Ahmed, D. Andrews, and G. J. Davies. One-dimensional conduction in the 2d electron-gas of a GaAs-AlGaAs heterojunction. *Phys. Rev. Lett.*, 56:1198, 1986.
- [61] B. J. van Wees, H. van Houten, C. W. J. Beenakker, J. G. Williamson, L. P. Kouwenhoven, D. Vandermaarel, and C. T. Foxon. Quantized conductance of point contacts in a two-dimensional electron-gas. *Phys. Rev. Lett.*, 60:848, 1988.
- [62] D. A. Wharam, T. J. Thornton, R. Newbury, M. Pepper, H. Ahmed, J. Frost, D. G. Hasko, D. C. Peacock, D. A. Ritchie, and G. Jones. One-dimensional transport and the quantization of the ballistic resistance. *Journal of Physics C : solid state physics*, 21:209–214, 1988.
- [63] R. Landauer. *IBM J. Res. Dev.*, 1:223, 1957.
- [64] R. Landauer. *Phil. Mag.*, 21:863, 1970.
- [65] M. Büttiker. Four-terminal phase-coherent conductance. *Phys. Rev. Lett.*, 57:1761, 1986.
- [66] Y. Imry. In G. Grinstein and G. Mazenko, editors, *Direction in condensed matter physics*, page 102. World Scientific, 1986.
- [67] G. Schön and A. D. Zaikin. Quantum coherent effects, phase transitions, and the dissipative dynamics of ultra small tunnel junctions. *Phys. Rep.*, 198:237, 1990.

- [68] C. W. J. Beenakker. Theory of Coulomb-blockade oscillations in the conductance of a quantum dot. *Phys. Rev. B*, 44:1646, 1991.
- [69] I. O. Kulik and R. I. Shekhter. 68:623, 1975. [*Sov. Phys. JETP* **41**, 308 (1975)].
- [70] L. P. Kouwenhoven, N.C. van der Vaart, A.T. Johnson, W. Kool, C.J.P.M. Harmans, J.G. Williamson, A.A.M. Staring, and C.T. Foxon. *Z. Phys. B*, 85:367, 1991.
- [71] E.B. Foxman, P.L. McEuen, U. Meirav, N.S. Wingreen, Y. Meir, P.A. Belk, N.R. Belk, M.A. Kastner, and S.J. Wind. Effects of quantum levels on transport through a Coulomb island. *Phys. Rev. B*, 47:10020, 1993.
- [72] E.B. Foxman, U. Meirav, P.L. McEuen, M.A. Kastner, O. Klein, P.A. Belk, D.M. Abusch, and S.J. Wind. Crossover from single-level to multilevel transport in artificial atoms. *Phys. Rev. B*, 50:14193, 1994.
- [73] L. P. Kouwenhoven, C. M. Marcis, P. L. McEuen, S. Tarucha, R. M. Westervelt, and N. S. Wingreen. Electron transport in quantum dots. In L.L. Sohn, L.P. Kouwenhoven, and G. Schn, editors, *Proceedings of the Advanced Study Institute on Mesoscopic Electron Transport*, page 1. 1997.
- [74] D.V. Averin and K.K. Likharev. *J. Low Temp. Phys.*, 62:345, 1986.
- [75] H. Grabert and M. H. Devoret. *Single charge tunneling*. Plenum Press, 1991.

- [76] A. Ambrózy. *Electronic noise*. McGraw-Hill International Book Company, 1982.
- [77] W. Schottky. *Ann. Physik*, 57:541, 1918.
- [78] L. Y. Chen and C. S. Ying. *Mod. Phys. Lett. B*, 9:573, 1995.
- [79] L. Y. Chen and C. S. Ying. Noise characteristics of sequential tunneling through double-barrier junctions. *Phys. Rev. B*, 46:4714, 1992.
- [80] B. L. Altshuler, L. S. Levitov, and A. Yu. Yakovets. 59:821, 1994. [JETP Lett. **59**, 857 (1994)].
- [81] M. I. Reznikov, M. Heiblum, H. Shtrikman, and D. Mahalu. Temporal correlation of electrons: Suppression of shot noise in a ballistic quantum point contact. *Phys. Rev. Lett.*, 75:3340, 1995.
- [82] A. Kumar, L. Saminadayar, D. C. Glatti, Y. Jin, and B. Etienne. Experimental test of the quantum shot noise reduction theory. *Phys. Rev. Lett.*, 76:2778, 1996.
- [83] Z. Wang, M. Iwanaga, and T. Miyoshi. *Jpn. J. Appl. Phys. Pt. 1*, 37:5894, 1998.
- [84] A. N. Korotkov. Intrinsic noise of the single-electron transistor. volume 49, page 10381. 1994.

- [85] S. Hershfield, J. H. Davies, P. Hyldgaard, C. J. Stanton, and J. W. Wilkins. Zero-frequency current noise for the double-tunnel-junction Coulomb blockade. *Phys. Rev. B*, 47:1967, 1993.
- [86] N. Bohr. Can quantum-mechanical description of physical reality be considered complete? *Phys. Rev.*, 48:696–702, 1935.
- [87] E. Schrödinger. Discussion of probability relations between separated systems. *Proc. Cambridge Phil. Soc.*, 31:555–563, 1935.
- [88] D. Bohm. *Quantum Theory*. New York: Prentice-Hall, 1951.
- [89] G. Greenstein and A. G. Zajonc. *Quantum Challenge: Modern Research on the Foundations of Quantum Mechanics*. Jones and Bartlett Publishers, Sudbury, Massachusetts, 1997.
- [90] J. M. Kikkawa and D. D. Awschalom. Resonant spin amplification in n-type GaAs. *Phys. Rev. Lett.*, 80:4313, 1998.
- [91] A. G. Huibers, M. Switkes, C. M. Marcus, K. Campman, and A. C. Gossard. Dephasing in open quantum dots. *Phys. Rev. Lett.*, 81:200, 1998.
- [92] R. Hanbury Brown and R. Q. Twiss. Correlation between photons in 2 coherent beams of light. *Nature*, 177:27–29, 1956.
- [93] R. Loudon. Fermion and Boson beam-splitter statistics. *Phys. Rev. A*, 58:4904, 1998.

- [94] D. P. DiVincenzo and D. Loss. Quantum computers and quantum coherence. *J. Mag. Magn. Matl.*, 200:202, 1999.
- [95] X. Hu and S. Das Sarma. Double quantum dot turnstile as an electron spin entangler. *Phys. Rev. B*, 69:115312, 2004.
- [96] X. Hu and S. Das Sarma. Hilbert space structure of a solid state quantum computer: two-electron states of a double quantum dot artificial molecule. *Phys. Rev. A*, 61:062301, 2000.
- [97] X. Hu and S. Das Sarma. Spin-based quantum computation in multielectron quantum dots. *Phys. Rev. A*, 64:042312, 2001.
- [98] A. T. Lee. A low-power-dissipation broadband cryogenic preamplifier utilizing GaAs MESFETs in parallel. *Rev. Sci. Instrum.*, 64:2373–2378, 1993.
- [99] A. van der Ziel. *Noise in Solid State Devices and Circuits*. New York: J. Wiley and Sons, 1986.
- [100] Y. Chen and R. A. Webb. Shot noise in tunnel barriers. *To be submitted*.
- [101] H. Birk, M. J. M. de Jong, and C. Schönenberger. Shot-noise suppression in the single-electron tunneling regime. *Phys. Rev. Lett.*, 75:1610, 1995.
- [102] R. Cron, M. F. Goffman, D. Esteve, and C. Urbina. Multiple-charge-quanta shot noise in superconducting atomic contacts. *Phys. Rev. Lett.*, 86:4104–4107, 2001.

- [103] H. E. van den Brom and J. M. van Ruitenbeek. Quantum suppression of shot noise in atom-size metallic contacts. *Phys. Rev. Lett.*, 82:1526–1529, 1998.
- [104] Y. P. Li, D. C. Tsui, J. J. Heremans, J. A. Simmons, and G. W. Weimann. Low-frequency noise in transport through quantum point contacts. *Appl. Phys. Lett.*, 57:774, 1990.
- [105] S. S. Safonov, A. K. Savchenko, D. A. Bagrets, O. N. Jouravlev, Y. V. Nazarov, E. H. Linfield, and D. A. Ritchie. Enhanced shot noise in resonant tunneling via interacting localized states. *Phys. Rev. Lett.*, 91:136801, 2003.
- [106] A. H. Steinbach, J. M. Martinis, and M. H. Devoret. Observation of hot-electron shot noise in a metallic resistor. *Phys. Rev. Letts*, 76:3806, 1996.
- [107] M. Henny, S. Oberholzer, C. Strunk, and C. Schönenberger. 1/3-shot-noise suppression in diffusive nanowires. *Phys. Rev. B*, 59:2871, 1999.
- [108] A. B. Fowler, G. L. Timp, J. J. Wainer, and R. A. Webb. Observation of resonant tunneling in silicon inversion layers. *Phys. Rev. Lett.*, 57:138, 1986.
- [109] T. E. Kopley, P. L. McEuen, and R.G. Wheeler. Resonant tunneling through single electronic states and its suppression in a magnetic field. *Phys. Rev. Lett.*, 61:1654, 1988.
- [110] Y. V. Nazarov and J. J. R. Struben. Universal excess noise in resonant tunneling via strongly localized states. *Phys. Rev. B*, 53:15466, 1996.

- [111] A. B. Fowler, J. J. Wainer, and R. A. Webb. Electronic transport in small strongly localized structures. *IBM J. Res. Develop.*, 32:372–383, 1988.
- [112] A. D. Stone and P. A. Lee. Effect of inelastic process on resonant tunneling in one dimension. *Phys. Rev. Lett.*, 54:1196, 1985.
- [113] L. Y. Chen and C. S. Ying. Noise characteristics of sequential tunneling through double-barrier junctions. *Phys. Rev. B*, 43:4534, 1991.
- [114] M. Büttiker. *Physica B*, 175:199, 1991.
- [115] V. V. Kuznetsov, E. E. Mendez, X. Zuo, G. L. Snider, and E. T. Croke. Partially suppressed shot noise in hopping conduction: Observation in SiGe quantum wells. *Phys. Rev. Lett.*, 85:397, 2000.
- [116] Y. Chen and R. A. Webb. Shot noise evidence for entangled electron spin states in coupled GaAs/GaAlAs quantum dots. *To be submitted*.
- [117] T. Martin and R. Landauer. Wave-packet approach to noise in multichannel mesoscopic systems. *Phys. Rev. B*, 45:1742, 1992.
- [118] L. P. Kouwenhoven, A. T. Johnson, N. C. van der Vaart, and C. J. P. M. Harman. Quantized current in a quantum-dot turnstile using oscillating tunnel barriers. *Phys. Rev. Lett.*, 67:1626–1629, 1991.